

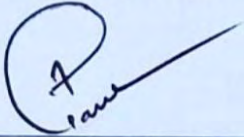
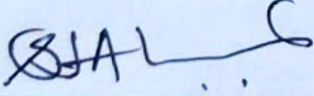
BANGLADESH UNIVERSITY OF ENGINEERING & TECHNOLOGY (BUET), DHAKA  
DEPARTMENT OF PHYSICS



**CERTIFICATION OF THESIS**

The thesis titled “**INVESTIGATION OF MLTIFERROIC AND PHOTOCATALYTIC PROPERTIES OF  $\text{Bi}_{0.9}\text{Y}_{0.1}\text{FeO}_3$  NANOPARTICLES**” submitted by **Md. Masud Parvez**, Roll No-1014143020F, Registration No-1014143020F, Session: October/14, has been accepted as satisfactory in partial fulfillment of the requirement for the degree of **Master of Philosophy (M. Phil.)** in Physics on **23 February, 2019**.

**BOARD OF EXAMINERS**

1.   
**Dr. Mohammed Abdul Basith**  
Professor,  
Department of Physics, BUET, Dhaka. Chairman  
(Supervisor)
2.   
**Head**  
Department of Physics, BUET, Dhaka. Member  
(Ex-Officio)
3.   
**Dr. Md. Feroz Alam Khan**  
Professor  
Department of Physics, BUET, Dhaka. Member
4.   
**Dr. Mohammad Jellur Rahman**  
Associate Professor  
Department of Physics, BUET, Dhaka. Member
5.   
**Dr. Syed Jamal Ahmed**  
Professor  
Department of Physics  
Dhaka University of Engineering and Technology (DUET)  
Gazipur, Dhaka. Member (External)

# INVESTIGATION OF MULTIFERROIC AND PHOTOCATALYTIC PROPERTIES OF $\text{Bi}_{0.9}\text{Y}_{0.1}\text{FeO}_3$ NANOPARTICLES

*A Dissertation Submitted to the Department of Physics, Bangladesh University of Engineering  
and Technology, Dhaka in Partial Fulfillment of Requirement for the Degree of  
M.Phil in Physics*

**SUBMITTED**

BY

**Md. Masud Parvez**

EXAMINATION ROLL NO. : 1014143020F

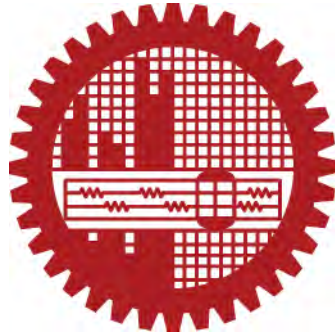
SESSION: OCTOBER 2014



DEPARTMENT OF PHYSICS  
BANGLADESH UNIVERSITY OF ENGINEERING AND TECHNOLOGY  
DHAKA 1000, BANGLADESH

# **Dedication**

*To my parents*



## **CANDIDATE'S DECLARATION**

It is hereby declared that this thesis or any part of it has not been submitted elsewhere for the award of any degree or diploma.

---

**Md. Masud Parvez**

# Acknowledgements

I would like to take this opportunity to thank everyone who made this work possible. First and foremost, I would like to express my utmost gratitude to my mentor and supervisor, Dr. Mohammed Abdul Basith, Professor, Department of Physics, Bangladesh University of Engineering and Technology (BUET), for giving me this wonderful opportunity to be a part of his multidisciplinary research team. Throughout my study period, his continuous guidance, encouragement and kind support have greatly shaped me into what I am today. In fact, I am quite lucky to be a part of this ambitious research team. It is my great honor to convey my gratitude to Professor, Dr. Md. Forhad Mina, Head, Department of Physics, BUET, for his wonderful support to move through the academic process during this degree program and to all respected teachers of the Department of Physics for their kind cooperation.

I am thankful to Department of Glass and Ceramic Engineering, BUET, Bangladesh for providing FESEM facilities.

I am also thankful to National Science and Technology Ministry for their financial support.

I wish to thank specially Md. Rafiq Azad, Areef Billah, Md. Abdul Jalil, Nilufar Yesmin, Sayeed Shafayet, and Sagar Dutta for their constant support in Nanotechnology Research Laboratory, BUET.

Most importantly, I would like to extend my gratitude to my family members, especially my parents and wife for their love, support and blessings, who have always been the greatest inspiration in my life in every possible way.

# Abstract

In this investigation,  $\text{BiFeO}_3$  and  $\text{Bi}_{0.9}\text{Y}_{0.1}\text{FeO}_3$  bulk polycrystalline materials have been synthesized by a conventional solid state reaction technique. Nanoparticles are also produced directly from their bulk powder materials by sol-gel method and ultrasonication technique. The XRD patterns ensure the phase transition from rhombohedrally distorted perovskite structure to orthorhombically distorted perovskite structure of the  $\text{Bi}_{0.9}\text{Y}_{0.1}\text{FeO}_3$  (prepared by sol-gel) sample. The Field Emission Scanning Electron Microscopy images and their respective histograms demonstrate that the particle size reduces in  $\text{Bi}_{0.9}\text{Y}_{0.1}\text{FeO}_3$  nanoparticles due to the doping of Yttrium (Y). The absorption spectra confirm that the undoped and doped  $\text{BiFeO}_3$  nanoparticles exhibit considerably high absorbance in the UV to visible range. Notably, 10% Y doped BFO nanoparticles prepared by sol-gel method exhibit the highest photodegradation efficiency.  $\text{Bi}_{0.9}\text{Y}_{0.1}\text{FeO}_3$  nanoparticles prepared by sol-gel method also exhibit a remarkable saturation magnetization may be associated with the size reduction of the particle size, suppression of impurity phases, structural transition and also crystallinity of the materials.

# Contents

<b>1.</b>	<b>Introduction</b>	<b>1</b>
1.1	Introduction	1
1.2	Aim and objectives	2
1.3	Outline of this thesis	3
<b>2.</b>	<b>Theoretical background</b>	<b>6</b>
2.1	Introduction	6
2.2	Multiferroics	6
2.3	Multiferroic materials	7
2.3.1	Classification of multiferroics	7
2.3.2	Split-order-parameter multiferroics (type-I)	8
2.3.2.1	Lone-pair multiferroics	9
2.3.2.2	Charge-ordered multiferroics	9
2.3.2.3	Geometrically frustrated multiferroics	9
2.3.2.4	Strain-induced multiferroics	10
2.3.3	Joint-order-parameter multiferroics (type-II)	10
2.3.3.1	Exchange-striction mechanism	11
2.3.3.2	Spin-current mechanism	12
2.3.3.3	p-d hybridization mechanism	13
2.4	BiFeO <sub>3</sub> type multiferroic	13
2.5	Structure of materials	13
2.5.1	Perovskite structure	14
2.5.9	Structure of BiFeO <sub>3</sub>	14
2.6	Magnetism	14
2.6.1	Origin of magnetism	16
2.6.2	Magnetic moment of atoms	18
2.6.3	Magnetic moment of electrons	19
2.6.4	Magnetic Behavior	20
2.6.5	Magnetic hysteresis loop	21
2.6.6	Cause of magnetic hysteresis loop	22
2.7	Ferroelectric behavior	23
2.7.1	Process of Polarization	24
2.7.1.1	Electronic polarization	24
2.7.1.2	Atomic polarization	25
2.7.1.3	Dipolar polarization	26
2.7.1.4	Space charge polarization	27
2.7.2	Ferroelectricity in BiFeO <sub>3</sub>	28
2.8	Photocatalytic activity	30
2.8.1	Photocatalysis	30
2.8.2	Photocatalysts	31
2.8.3	Parameters affecting photocatalysis	32
2.8.4	Nanosized materials	33
2.8.5	BiFeO <sub>3</sub> nanoparticles as a photocatalyst	34
<b>3.</b>	<b>Sample Preparations and Experimental Techniques</b>	<b>41</b>
3.1	Introduction	41
3.2	Synthesis of bulk polycrystalline sample	41
3.2.1	solid state reaction technique	41

3.2.1.1	Calcination	42
3.2.1.2	Pelletization	43
3.2.1.3	Sintering	43
3.2.2	Preparation of Bi <sub>0.9</sub> Y <sub>0.1</sub> FeO <sub>3</sub> bulk materials	44
3.3	Fabrication of Nanoparticles by Ultrasonication	44
3.3.1	Ultrasonication Technique	44
3.3.2	Sonication effects on particle disruption and aggregation	47
3.3.3	Why Sonication Technique	48
3.3.4	Preparation of Bi <sub>0.9</sub> Y <sub>0.1</sub> Fe O <sub>3</sub> nanoparticles by Ultrasonication	50
3.4	Sol-gel Method	50
3.4.1	Why Sol-gel Method	50
3.4.2	Preparation of BiFeO <sub>3</sub> Nanoparticles by Sol-gel Method	51
3.4.3	Synthesis of Bi <sub>0.9</sub> Y <sub>0.1</sub> FeO <sub>3</sub> Nanoparticles by Sol-gel	52
3.4.4	Annealing	53
3.5	Structural characterization techniques	53
3.5.1	X-ray diffraction	52
3.6	Morphological Studies	55
3.6.1	Field Effect Scanning Electron Microscope (FESEM)	55
3.6.2	Scanning process and image formation	56
3.7	Ferroelectric measurement	57
3.7.1	Ferroelectric loop tracer	57
3.7.1.1	Basic theory of operation	58
3.7.1.2	Basic calculation	58
3.8	Optical measurement	59
3.8.1	UV-Visible diffuse reflectance spectroscopy	59
3.8.2	UV-Visible spectrophotometer	62
3.8.3	Photocatalytic Activity Test	63
3.9	Magnetization measurement	66
3.9.1	Vibrating sample magnetometer (VSM)	66
<b>4.</b>	<b>Results and Discussions</b>	<b>73</b>
4.1	Introduction	73
4.2	Crystal Structure Analysis	73
4.3	Morphological Analysis	76
4.4	Optical Measurement	78
4.4.1	Absorbance and band gap estimation	79
4.4.2	Photocatalytic activity test	80
4.4.3	Photocatalytic Mechanism	82
4.5	Magnetic Characterization	83
4.6	Ferroelectric Behavior	85
<b>5.</b>	<b>Summary and Conclusions</b>	<b>93</b>
5.1	Summary	93
5.2	Conclusion	94
5.3	Suggestion for future work	94

## List of Figures

2.1	Schematic diagram of multiferroic materials	7
2.2	Schematic view of (a) Kagom'e lattice and (b) triangular lattice	9
2.3	Cluster model consisting of two magnetic ions (carrying spin moments $s_i$ and $s_j$ ) which are connected via vector $e$ and hybridized through ligand ion	10
2.4	The symmetric exchangestriction mechanism. (a) GKA rules (b) centrosymmetric chain with no polarization (c) non-centrosymmetric chain with polarization	12
2.5	Structure of a perovskite with a chemical formula $ABX_3$ . The red spheres are X atoms (usually oxygen), the blue spheres are B-atoms (a smaller metal cation, such as $Ti^{4+}$ ), and the green spheres are the A-atoms (a larger metal cation, such as $Ca^{2+}$ ). Pictured is the undistorted cubic structure; the symmetry is lowered to orthorhombic, tetragonal or trigonal in many perovskites	14
2.6	(a) Structure of a perovskite with a chemical formula $ABO_3$ (b) rhombohedrally distorted perovskite structure.	15
2.7	A spin magnetic moment associated with it due to the electron itself like the earth on its own axis.	17
2.8	Hysteresis loop for a ferromagnetic material	22
2.9	Dependence of the hysteresis loop of iron or steel on hardness caused by the addition of carbon or other non-magnetic material or by cold working.	23
2.10	A typical room temperature ferroelectric hysteresis measured along the pseudo-cubic [001]-axis. The full polarization, pointing along the pseudocubic [111]-axis, should be 3 times larger	24
2.11	Electronic polarization.	25
2.12	Atomic polarization.	26
2.13	Dipolar polarization.	27
2.14	Space charge polarization.	27
2.15	Variation of polarization with frequency.	28
2.16	Crystal structure of bulk $BiFeO_3$ with opposite rotation of successive oxygen octahedral around [111] polar axes. Red arrow indicates orientation of Fe magnetic moments in (111) plane.	29
3.1	Flow chart of the preparation of bulk polycrystalline materials by solid-state reaction technique	42
3.2	Schematic representation of sintering stages: (a) green body, (b) initial stage, (c) intermediate stage, and (d) final stage.	43
3.3	Schematic illustration of ultrasonic wave-induced cavitation and agglomerate fracture.	45
3.4	Schematic illustration of direct (left) and indirect (middle and right) sonication configurations as described in the text.	46
3.5	Schematic depiction of particle structures referred to in the text, and illustration of the typical effects of sonication on particle size as a function of delivered sonication energy.	48
3.6	A bath sonicator of 500 W (Model: POWERSONIC 510 HWASHIN technology Co.)	49
3.7	Synthesis steps a) Dissolving components with 4 hours continuous stirring b) Solution after pH control c) Solution during heating at about 70 °C to 80 °C d) Onset of a thin gel like layer e) Dried gel after oven heating f) After final grinding.	51
3.8	Furnace used for annealing xerogel sample	53
3.9	Annealing cycle	53
3.10	Schematic diagram for a X-ray powder diffraction (XRD) experiment. Adapted from BRUNDLE ET AL. [26].	54
3.11	Photograph of Field Effect Scanning Electron Microscope (FESEM)	55
3.12	Schematic diagram of Field Emission Scanning Electron Microscope (FESEM)	57
3.13	An schematic diagram of Sawyer tower circuit for P-E loop tracer	58
3.14	P-E loop tracer system (Marin India)	59
3.15	The Kubelka-Munk approximation: the incident and remitted light fluxes are	60

	approximated by two opposite fluxes, perpendicular to the surface of the infinitely thick sample layer.	
3.16	Solid sample measurement using the integrating sphere method Source: Optional Accessories for Shimadzu UV-Vis spectrophotometers	61
3.17	UV-visible spectrometer Shimadzu UV-2600 ISR plus was used to take the absorbance and reflectance data	62
3.18	Illustration of a double beam UV-vis instrument	63
3.19	Experimental setup of photocatalytic activity experiment. (a) closed system of Xenon lamp setup, (b) open system of xenon lamp setup, (c) Lux meter used to measure lamp-light intensity and (d) centrifuge machine used to separate the RhB solution and photocatalyst.	64
3.20	Degradation of rhodamine mine B. (a) color of RhB before illumination under xenon-lamp-light, (b) after illumination of the solutions under xenon-lamp-light for 50 minutes for different photocatalysts	64
3.21	The illumination of Rhodamine B(RhB) under visible light irradiation.	65
3.22	EV9 Micro sense Vibrating Sample Magnetometer.	66
3.23	Schematic diagram of (a) VSM and (b) details near the pickup coils.	68
4.1	X-ray diffraction patterns of the synthesized bulk materials and their corresponding nanoparticles (b): Magnified view of X-ray diffraction pattern.	74
4.2	FESEM images of the (a) $B_{0.9}Y_{0.1}FeO_3$ Nanoparticles (Sol-gel) (b) $B_{0.9}Y_{0.1}FeO_3$ Nanoparticles (Ultra sonication) (c) $B_{0.9}Y_{0.1}FeO_3$ Bulk (Solid-state) (d) BFO Nanoparticles (Solgel) (e) BFO Bulk (solid state)	77
4.3	(a) Absorption spectra for $BFeO_3$ bulk materials and its corresponding nanoparticles (b) Absorption spectra for $B_{0.9}Y_{0.1}FeO_3$ bulk materials and their corresponding nanoparticles	78
4.4	Kubelka Munk (KM) plot to estimate the band gap energy of the synthesized (a) BFO nano and (b) BFO bulk (c) $Bi_{0.9}Y_{0.1}FeO_3$ bulk, $Bi_{0.9}Y_{0.1}FeO_3$ Nano (prepared by Sol-gel) and $Bi_{0.9}Y_{0.1}FeO_3$ Nano (prepared by Ultrasonication) samples.	79
4.5	Photocatalytic degradation spectra by (a) $x = 0.00$ bulk materials, (b) $Bi_{0.9}Y_{0.1}FeO_3$ bulk materials, (c) $Bi_{0.9}Y_{0.1}FeO_3$ nanoparticles (Sol-gel) and (d) $Bi_{0.9}Y_{0.1}FeO_3$ nanoparticles (Ultrasonication) (e) their $C/C_0$ ratio graphs	81
4.6	Schematic illustration of the photocatalytic mechanism of BFO photocatalyst toward the degradation of RhB.	82
4.7	The room temperature M-H hysteresis loops of BFO and $Bi_{0.9}Y_{0.1}FeO_3$ (a) BFO bulk and nano materials (b) The enlarged view of BFO bulk and nano particles (c) MH hysteresis loops of $Bi_{0.9}Y_{0.1}FeO_3$ bulk and their corresponding nanoparticles (prepared by both Ultrasonication and Sol-gel technique) (d) The enlarged view of the hysteresis loops of $Bi_{0.9}Y_{0.1}FeO_3$ bulk and their corresponding nanoparticles (prepared by both Ultrasonication and Sol-gel technique)	84
4.8	The P-E hysteresis loop for (a) BFO Nanoparticles (b) $Bi_{0.9}Y_{0.1}FeO_3$ Nano (Sol-gel) (c) BFO Bulk (d) $Bi_{0.9}Y_{0.1}FeO_3$ (Ultrasonication)	86

## List of Tables

4.1	The table shows the calculated lattice parameters of the synthesized nanoparticle.	75
4.2	The table shows the average crystallite size (calculated from XRD patterns) and average particle size (calculated from FESEM images)	75
4.3	Remanent magnetization, coercive field and exchange bias field of the synthesized bulk powder materials and their corresponding nanoparticles.	83

# Chapter 1

## Introduction

### 1.1 Introduction

Multiferroic  $\text{BiFeO}_3$  (BFO) is a promising functional material in which ferroelectric (FE) and ferromagnetic (FM)/antiferromagnetic (AFM) orderings coexist. Among the many available single phase multiferroics,  $\text{BiFeO}_3$  (BFO) is the only room temperature (RT) multiferroic with  $T_C = 1043$  K and  $T_N = 647$  K having finite magnetoelectric (ME) effect. Recently, BFO systems have attracted scientific community greatly due to their fascinating properties in the field of material science and potential applications in various multifunctional devices [1-3]. Notably, due to the modulation of the cycloidal spiral spin structure with long wavelength period of 62 nm [4], the net magnetization of BFO is usually canceled out and hence a linear magnetization hysteresis (M–H) loop is observed. Several approaches have been attempted to suppress the spin modulated spiral structure (SMSS) in BFO and thus enhance the multiferroic behavior of BFO. These approaches are (i) structural modifications or deformations introduced by cation substitutions [5, 6], (ii) synthesizing BFO nanoparticles with particle size less than periodicity of helical order  $\sim 62$  nm [7], (iii) fabrication of epitaxial thin films [8], and (iv) application of high magnetic fields [9]. However, the electioneering of BFO for sensible applications is restricted by many factors, a number of them are listed here. (i) It's terribly tough to synthesize BFO in single phase because of the constant prevalence of secondary phases  $\text{Bi}_2\text{Fe}_4\text{O}_9$  and  $\text{Bi}_{25}\text{FeO}_{40}$ , that diminishes the magnetoelectric properties. (ii) High discharge current related to low polarization in bulk BFO systems, (iii) Weak magnetization. All these downsides limit BFO for the usage in devices. The multiferroic properties of BFO are very sensitive to its intrinsic defects, such as vacancies and phase purity. In the earlier studies, a lot of work has already been performed on the BFO synthesis, addressing varied issues concerned with the preparation of single phase particles to avoid the formation of secondary phases like  $\text{Bi}_2\text{Fe}_4\text{O}_9$  and  $\text{Bi}_{25}\text{FeO}_{40}$  [4,5] and simple volatilization of bismuth at high temperatures (near to its crystallization temperature) [6]. The presence of secondary phases will be avoided in solid-state (SS) synthesized samples by the popular leaching technique of exploiting  $\text{HNO}_3$  [7]. However, such samples end in the coarse powders and diminish the electrical properties [8]. Rapid liquid phase sintering technique can be used to avoid the formation of impurity phases [9].

## Chapter1: Introduction

---

Moreover, to avoid the metallic element loss at high temperatures, adding excess  $\text{Bi}_2\text{O}_3$  as fundamental compound is practiced by several researchers [10]. Even after that, one cannot have complete control over the number of loss of bismuth throughout the reaction. Besides these same old solid-state reaction, some completely different wet chemical routes such as, hydrothermal [11], sol-gel technique [12,13], automobile combustion [14] have been introduced recently which are able to cut back the oxidization temperature and produce pure phase nanoparticles. These wet chemical routes have been proved pretty much promising as they produce BFO at comparatively low temperature compared to solid state reaction route.

In the present investigation nominal composition of  $\text{Bi}_{0.9}\text{Y}_{0.1}\text{FeO}_3$  bulk polycrystalline ceramics were synthesized by conventional solid state reaction technique. The  $\text{Y}^{3+}$  ion has been chosen as a dopant due to its smaller ionic radius ( $\sim 0.90 \text{ \AA}$ ) than that of  $\text{Bi}^{3+}$  ion ( $1.03 \text{ \AA}$ ), which may result in large lattice distortion [12] and enhance the multiferroic optical properties of Y doped BFO. Then the nanoparticles were fabricated directly from their bulk powder materials by sol-gel method and ultrasonication technique. The structural, morphological, electrical, optical, photocatalytic and magnetic properties were investigated for both bulk polycrystalline materials and their nanoparticles. Investigation of the surface morphology and the crystal structure of the samples were done by using Field Emission Scanning Electron Microscope (FESEM) and X-Ray Diffraction (XRD) techniques, respectively. The electrical polarization (P) was observed as a function of applied electric field (E) at room temperature using a ferroelectric looptracer. Optical properties and photocatalytic activity of the synthesized samples were investigated by an experimental setup which involved xenon lamp, magnetic stirrer, lux meter, centrifuge machine and UV-vis spectrometer. Magnetic properties of the fabricated materials were carried out using a Vibrating Sample Magnetometer (VSM)

## 1.2 Aim and objectives

The main objectives of the present research are as follows:

- (i) Preparation of ultrafine nanoparticles of  $\text{Bi}_{0.9}\text{Y}_{0.1}\text{FeO}_3$  multiferroics using ultrasonication [10] and sol-gel [11] method.
- (ii) Investigation of their crystal structure using X-ray diffraction (XRD) techniques.
- (iii) Investigation of the particle size distribution of the synthesized nanoparticles using Field Effect Scanning Electron Microscopy (FESEM) imaging.

- (iv) Investigation of the ferroelectric properties of these multiferroic nanoparticles using a ferroelectric loop tracer (polarization vs electric field) such as measurement of the leakage current density as a function of electric field.
- (v) Measurements of the magnetic properties such as saturation magnetization ( $M_s$ ), remanent magnetization ( $M_r$ ) and coercivity ( $H_c$ ) of Y doped  $\text{BiFeO}_3$  nanoparticles from hysteresis loops by using a magnetometer.
- (vi) Investigation of the photocatalytic activity of the synthesized nanoparticles from optical measurements.

### 1.3 Outline of this thesis

The introduction, importance of multiferroic materials and objectives are discussed in **chapter 1**. A brief overview of the multiferroic materials and theoretical background are described in **chapter 2**. The experimental techniques used for the present investigations are illustrated in **chapter 3**. **Chapter 4** is dedicated to the results of various investigations of the study and explanation of results in the light of existing theories. Finally, the results are concluded and brief outlooks to possible future experiments are presented in **chapter 5**.

# Bibliography

- [1]. Eerenstein, W., Mathur, N. D., and Scott, J. F., “Multiferroic and magnetoelectric materials”, *Nature*, 442, 759-765, 2006.
- [2]. Ramesh, R., “Emerging routes to multiferroics”, *Nature*, 461, 1218-1219, 2009.
- [3]. Basith, M. A., Khan, F. A., Bashir, A., Shigeru, K., Fumihiko, H., Ngo, D.T., Tran, Q.H., and Molhave, K., “Tunable exchange bias effect in magnetic  $\text{Bi}_{0.9}\text{Gd}_{0.1}\text{Fe}_{0.9}\text{Ti}_{0.1}\text{O}_3$  nanoparticles at temperatures up to 250 K”, *J. Appl. Phys.*, 118, 023901, 2015.
- [4]. Fischer, P., Polomska, M., Sosnowska, I., and Szymanski, M., “Temperature dependence of the crystal and magnetic structures of  $\text{BiFeO}_3$ ”, *J. Phys. C: Solid State Phys.*, 13, 1931 – 1940, 1980.
- [5]. Bashir, A., Kensaku, K., Kunihiro, K., Shigeru, K., Hiroaki, K., Fumihiko, H., Areef, B., Jalil, M. A., and Basith, M. A., “Large difference between the magnetic properties of Ba and Ti co-doped  $\text{BiFeO}_3$  bulk materials and their corresponding nanoparticles prepared by ultrasonication”, *J. Phys. D: Appl. Phys.*, 49, 265003, 2016.
- [6]. Bashir, A., Islam, M. Z., Areef, B., and Basith, M.A., “Anomalous coercivity enhancement with temperature and tunable exchange bias in Gd and Ti co-doped  $\text{BiFeO}_3$  multiferroics”, *J. Appl. Phys. D.*, 49, 095001, 2016.
- [7]. Nuraje, N., and Su, K., “Perovskite ferroelectric nanomaterials”, *Nanoscale*, 5, 8752-8786, 2013.
- [8]. Bai, F., Wang, J., Wuttig, M., Li, J. F., and Wang, N., “Destruction of spin cycloid in (111) c-oriented  $\text{BiFeO}_3$  thin films by epitaxial constraint: Enhanced polarization and release of latent magnetization”, *Appl. Phys. Lett.* 86, 032511, 2005.
- [9]. Wei, J., Haumont, R., Jarrier, R., Berhtet, P., and Dkhil, B., “Nonmagnetic Fe-site doping of  $\text{BiFeO}_3$  multiferroic ceramics”, *Appl. Phys. Lett.* 96, 102509, 2010.
- [10]. Basith, M. A., Ngo, D.T., Quader, A., Rahman, M. A., Sinha, B. L., Bashir Ahmmad, Fumihiko Hirose and Molhave, K., “Simple top-down preparation of magnetic  $\text{Bi}_{0.9}\text{Gd}_{0.1}\text{Fe}_{1-x}\text{Ti}_x\text{O}_3$  nanoparticles by ultrasonication of multiferroic bulk material”, *Nanoscale*, 6, 14336, 2014.
- [11]. Mehedi, H., Hakim, M. A., Basith, M. A., Hossain, M. S., Bashir, A., Zubair, Hussain, A., and Islam, M. F., “Size dependent magnetic and electrical properties of Ba-doped nanocrystalline  $\text{BiFeO}_3$ ”, *AIP advances*, 6, 035314, 2016.

## Chapter1: Introduction

---

- [12]. Mukherjee, A., Hossain, Sk. M., Pal, M., and Basu, S. “Effect of Y-doping on optical properties of multiferroics BiFeO<sub>3</sub> nanoparticles”. *Appl. Nanosci.* 2, 305–310, 2012.
- [13]. Basith, M. A., Kurni, O., Alam, M. S., Sinha, B. L., and Bashir, A., “Room temperature dielectric and magnetic properties of Gd and Ti co-doped BiFeO<sub>3</sub> ceramics”, *J. Appl. Phys.*, 115, 024102–024107, 2014.

# Chapter 2

## Theoretical background

### 2.1 Introduction

Electricity and magnetism were combined into one common discipline in the 19<sup>th</sup> century, culminating in the Maxwell equations [1]. These equations tell us about the unified nature of magnetism and electricity. But electric and magnetic ordering in solids are most often considered separately and usually with good reason: the electric charges of electrons and ions are responsible for the charge effects, whereas electron spins govern magnetic properties. There are, however, cases where these degrees of freedom couple strongly. For example, in the new, large field of spintronics, the effects of spins on the transport properties of solids (and vice versa) allow the possibility to control one by the other. The finding of a strong coupling of magnetic and electric degrees of freedom in insulators can be traced back to Pierre Curie, but the real beginning of this field started in 1959 with a short remark by Landau and Lifshitz in a volume of their Course of Theoretical Physics [2].

### 2.2 Multiferroics

The term multiferroic was first used by H. Schmid in 1994 [3]. Multiferroics are single phase materials which simultaneously possess two or more primary ferroic order parameter. The four basic primary ferroic order parameters are:

- ferromagnetism
- ferroelectricity
- ferroelasticity
- ferrotoroidicity

The definition of multiferroics can be expanded to include non-primary order parameters, such as antiferromagnetism, ferrimagnetism and antiferroelectricity. If the coupling between electric and magnetic order parameters exists, a multiferroic material becomes a magnetoelectric material shown in figure 2.1. But a magnetoelectric (or a multiferroic) material does not necessary to be a multiferroic (or a magnetoelectric) material [4]. The

history of magnetoelectric multiferroics can be traced back to the 1960s [5]. In the most general sense

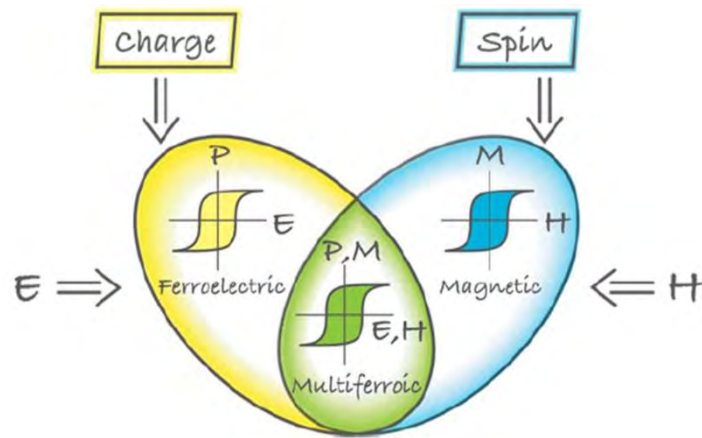


**Figure 2.1:** A schematic diagram of multiferroic

the field of multiferroics was born from studies of magnetoelectric systems. In recent 10 years, there is a great revival in multiferroics. In 2000, Nicola A. Hill gave an answer about scarcity of ferromagnetic ferroelectric coexistence [6]. In 2003 the large ferroelectric polarization was discovered in epitaxially grown thin films of  $\text{BiFeO}_3$  [7]. The same year, the strong magnetic and electric coupling was found in orthorhombic  $\text{TbMnO}_3$  [8] and  $\text{TbMn}_2\text{O}_5$  [9]. The recent studies of multiferroics show the importance of collaboration between experiment technology and modeling design.

## 2.3 Multiferroic materials

### 2.3.1 Classification of multiferroics

Multiferroic materials can broadly be classified in two categories namely single phase and composite materials. Single phase multiferroic materials show both ferroelectric and ferromagnetic order and they have similar crystal structure [10-16]. For the case of single phase multiferroic, multiferroicity is intrinsic effect of the material. Composite multiferroic materials results from the combination of two materials, those are ferroelectric and ferromagnetic separately. For the case of composite multiferroic, multiferroic order is not intrinsic and they have different structures. Single phase multiferroics can be classified into two big groups according to Khomskii classification [24].

- a) Type-I multiferroics
- b) Type-II multiferroics

### **Type-I multiferroics**

Type-I multiferroics are those materials in which ferroelectricity and magnetism have different sources; usually they show large polarization values and ferroelectricity appears at much higher temperatures than magnetism. This difference in transition temperatures reveals that both orders involve different energy scales and mechanisms, which provokes the occurrence of weak magnetoelectric coupling.  $\text{BiFeO}_3$  is the example of type-I multiferroic.

### **Type-II multiferroics**

Type-II multiferroic is novel class of multiferroics in which ferroelectricity exists only in a magnetically ordered state and caused by a particular type of magnetism. Type-II multiferroics divided into two groups: those in which ferroelectricity is caused by a particular type of magnetic spiral and those in which ferroelectricity appears even for collinear magnetic structures.  $\text{TbMnO}_3$  is the example of type-II multiferroic.

Many multiferroics are transition metal oxides with perovskite crystal structure, and include rare-earth manganites and ferrites (e.g.  $\text{TbMnO}_3$ ,  $\text{HoMn}_2\text{O}_5$ ,  $\text{LuFe}_2\text{O}_4$  and recently, “PZTFT” [3]). Other examples are the bismuth compounds  $\text{BiFeO}_3$  [4] and  $\text{BiMnO}_3$ , non-perovskite oxide  $\text{LiCu}_2\text{O}_2$  [5], and non-oxides such as  $\text{BaNiF}_4$  and spinel chalcogenides, e.g.  $\text{ZnCr}_2\text{Se}_4$ . These alloys show rich phase diagrams combining different ferroic orders in separate phases. One can identify two main classes of multiferroic materials with coupled electrical and magnetic properties; one in which the electrical and magnetic properties have different origins and hence two separate order-parameters (split-order-parameter multiferroics) and those in which the electrical properties stem from the magnetic ordering (joint-order-parameter multiferroics). Both types are described briefly below.

### **2.3.2 Split-order-parameter multiferroics (type-I)**

Split-order parameter multiferroics are usually good ferroelectric materials with large electrical polarization in the order  $0.1 - 1 \text{ C/m}^2$ . The ferroelectric transition temperature is often far above room temperature and well separated from the magnetic transition, being lower in temperature. The coupling of magnetic and electrical properties is weak since they originate from different sources. Several main groups of type-I multiferroics are known and the four most prominent of them are:

### 2.3.2.1 Lone-pair multiferroics

A number of transition metal perovskites, such as for example  $\text{BiMnO}_3$  [8] and  $\text{BiFeO}_3$  [9], do indeed order magnetically. In these so-called lone-pair multiferroics, the ferroelectricity occurs due to an electron lonepair (6s) on the A site, whereas the magnetic ordering stems from the B site magnetic moments of Mn and Fe, respectively. Hence, the origin of the electrical and magnetic ordering is different and the coupling between them is very weak.

### 2.3.2.2 Charge-ordered multiferroics

Another mechanism that gives rise to combined electric and magnetic properties can be found in charge-ordered multiferroics, e.g.  $\text{LuFe}_2\text{O}_4$  [10]. Here the ferroelectricity comes from the charge ordering of magnetic ions with different valence states giving rise to inequivalent bonds and hence ferroelectricity without ionic displacement.

### 2.3.2.3 Geometrically frustrated multiferroics

In geometrically frustrated multiferroics competition of magnetic interaction between different ion sites can give rise to lattice distortions, for example off-centering of ions into  $\text{YMnO}_3$  [9]. At low temperatures the frustrated systems can order into a non-collinear structure to compensate for the geometrical frustration, triangular and Kagomé lattice shown in figure 2.2. An anomaly in the dielectric function at magnetic phase transition is evident for the strong coupling between ferroelectric and magnetic ordering.

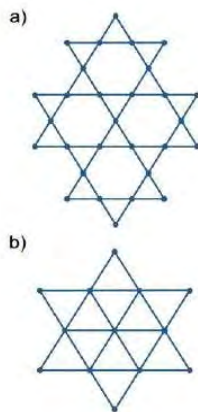


**Figure 2.2:** Schematic view of (a) Kagomé lattice and (b) triangular lattice.

### 2.3.2.4 Strain-induced multiferroics

In thin film heterostructures (for example  $\text{BiFeO}_3$  on  $\text{SrTiO}_3$  [10]) the electrical and magnetic properties can be mechanically coupled. Such strain induced multiferroics are based on magnetoelastic and magnetostriction effects in which an applied magnetic field will change the lateral dimension in one of the layers. Coupling through the mechanical interface induces strain in the second layer (or the substrate), which may give rise to an electrical polarization. A high quality of the interface is crucial to ensure optimal coupling in these systems. Pulsed laser deposition (PLD) is a capable technique for the fabrication of such heterostructures with both piezoelectric and magnetostrictive layers.

### 2.3.3 Joint-order-parameter multiferroics (type-II)

In type-II multiferroics, the ferroelectric properties derive directly from the magnetic long range ordering and the coupling between electrical and magnetic properties is inherently strong. Such magnetically driven multiferroics are found among insulating transition metal oxides with competing interaction and frustration, in which the magnetic ordering favors complex magnetic structures, for example in a cycloidal spin spiral. Since the electrical polarization occurs at the magnetic phase transition temperature, such materials can be described by one joint order parameter. Unfortunately, the magnetically induced polarization is usually weak and several orders of magnitude smaller than in type-I materials.

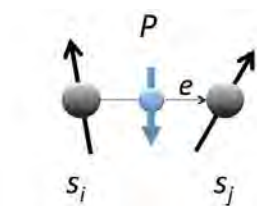


**Figure 2.3:** Cluster model consisting of two magnetic ions (carrying spin moments  $s_i$  and  $s_j$ ) which are connected via vector  $e$  and hybridized through a ligand ion.

A condition for a spontaneous electrical polarization in these materials is the breaking of inversion symmetry, which is accomplished via the magnetic ordering. Three main mechanisms for the formation of magnetically induced ferroelectricity are described in the

literature and are addressed by the cluster model (figure 2.3) [11,12],

$$\mathbf{P} = \mathbf{P}^{ES} \cdot \mathbf{e}(\mathbf{s}_i \cdot \mathbf{s}_j) + \mathbf{P}^{SC}(\mathbf{s}_i \times \mathbf{s}_j) \times \mathbf{e} + \mathbf{P}^{p-d}((\mathbf{e} \cdot \mathbf{s}_i) \cdot \mathbf{s}_i - (\mathbf{e} \cdot \mathbf{s}_j) \cdot \mathbf{s}_j) \quad (2.1)$$

All three mechanisms: (1) exchangestriction ( $\mathbf{P}^{ES}$ ), (2) spincurrent ( $\mathbf{P}^{SC}$ ) and (3) p-d hybridization ( $\mathbf{P}^{p-d}$ ) involving M-O-M bonds with M being a magnetic ion and O being oxygen. These mechanisms are described in some detail below:

### 2.3.3.1 Exchange-striction mechanism

In collinear spin-chains, multiferroicity can be understood in terms of the exchange-striction mechanism [13,14]. Two types of exchange-striction interaction can be described, the symmetric exchange based on the Heisenberg exchange interaction and the antisymmetric exchange through the inverse DZHALOSHINSKII-MORIYA (DM) interaction (incl. spin-orbit coupling). The corresponding Hamiltonian is given by

$$H = \frac{1}{2} \sum_{ij} J_{ij} s_i s_j + \frac{1}{2} \sum_{ij} \mathbf{D}_{ij} \cdot (\mathbf{s}_i \times \mathbf{s}_j) \quad (2.2)$$

with the first term being the Heisenberg exchange interaction and the second term being the Dzyaloshinskii Moriya (DM) interaction. The Dzyaloshinskii Moriya vector is given by  $\mathbf{D}_{ij} \propto \chi \times \mathbf{e}_{ij}$ , with  $\chi$  being the displacement of the ligand ion vertical to  $\mathbf{e}$ . For symmetric exchange the first term in equation 2.2 dominates and the occurrence of an electrical polarization can be explained by ionic displacements (non-centrosymmetric) due to the GOODENOUGH KANAMORI ANDERSON (GKA) rules [15–17]. If one considers simple configurations the GKA rules predict antiferromagnetic (AFM) coupling for bond angles close to  $180^\circ$  and ferromagnetic (FM) coupling for a bond angle of approximately  $90^\circ$ . A schematic illustration for the electrical polarization based on symmetric exchange is shown in figure 2.4. The second term in equation 2.2 describes antisymmetric exchange interaction. In a noncollinear structure, such as helicoidal, cycloidal or conical spin arrangement, spin canting occurs and induces a polar displacement (inverse Dzyaloshinskii Moriya interaction). Besides the magnetically-induced ferroelectricity due to ionic displacements, electronic charge displacements can also take place.

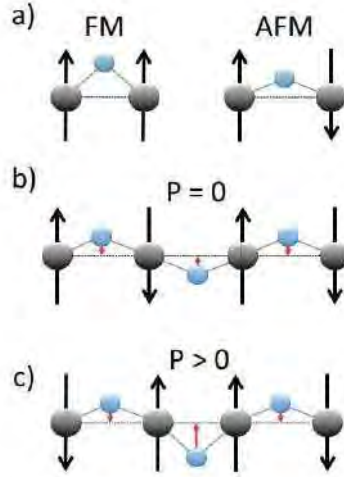


**Figure 2.4:** The symmetric exchange-striction mechanism. (a) GKA rules (b) centrosymmetric chain with no polarization (c) non-centrosymmetric chain with polarization.

### 2.3.2.2 Spin-current mechanism

Spiral magnetic ordering is usually a consequence of magnetic frustration. The occurrence of ferroelectricity in these systems can also be understood in terms of the spin-current mechanism proposed by KATSURA, NAGAOSA, AND BALATSKY [18] and separately by M. MOSTOVOY [19]. In the spin-current mechanism, ions may be fixed in a centrosymmetric structure and the electrical polarization is due to electronic charge displacements. The spontaneous polarization can be explained via a spin current defined as  $\mathbf{j}_s \sim J_{ij}(\mathbf{s}_i \times \mathbf{s}_j)$ , where  $\mathbf{s}_i$  and  $\mathbf{s}_j$  are noncollinear neighboring spins and  $J_{ij}$  is the Heisenberg exchange constant. The spin-current can be understood as virtual electron hopping. For a cycloidal spin spiral the electrical polarization can be described as

$$\mathbf{P} \sim \mathbf{e}_{ij} \times \mathbf{j}_s \sim \mathbf{e}_{ij} \times (\mathbf{s}_i \times \mathbf{s}_j) \sim (\mathbf{k} \times \mathbf{r}). \quad (2.3)$$

With  $\mathbf{e}_{ij}$  connecting two neighboring ions,  $\mathbf{k}$  is the propagation vector of the spiral and  $\mathbf{r}$  is the spin rotation axis. The electrical polarization is hence orthogonal to the spiral propagation vector and lies in the spiral plane. For applied magnetic fields the magnetic moments try to arrange in a plane perpendicular to the external field, which can result in spin flop transition.

### 2.3.2.3 p-d hybridization mechanism

A second mechanism in non-collinear spin-spiral materials is due to variation of p-d hybridization. Here non-zero polarization develops along the direction of the M-O-M cluster, hence parallel to  $e_{ij}$ , connecting two neighboring ions. Magnetically-induced ferroelectricity is comparably small, which makes it difficult to decide whether the ionic or electronic displacements are the source of the electrical polarization. Magnetically induced ionic displacements are close to the resolution limit of neutron and X-ray experiments.

## 2.4 BiFeO<sub>3</sub> type multiferroic

Bismuth ferrite (BiFeO<sub>3</sub>, also commonly referred to as BFO in Materials Science) is an inorganic chemical compound with perovskite structure and one of the most promising multiferroic materials. The room-temperature phase of BiFeO<sub>3</sub> is classed as rhombohedral belonging to the space group R3c [5]. It is synthesized in bulk and thin film form and for both cases, its antiferromagnetic (G type ordering) Néel temperature and ferroelectric Curie temperature are well above room temperature (approximately 653 K and 1100 K, respectively) [6,7]. Ferroelectric polarization occurs along the pseudo cubic [111] direction with a magnitude of 90-95  $\mu\text{C}/\text{cm}^2$  [23,24].

## 2.5 Structure of materials

A crystal structure is a unique arrangement of atoms, ions or molecules in a crystalline liquid or solid. It describes a highly ordered structure, occurring due to the intrinsic nature of its constituents to form symmetric patterns. Lattice is the symmetrical three dimensional arrangements of atoms inside a crystal. A crystal's structure and symmetry play a vital role in determining many of its physical properties, such as cleavage, electronic band structure, and optical transparency. The lattice systems of crystal structures are a grouping according to the axial system used to describe their lattice. Each lattice system consists of a set of three axes in a particular geometric arrangement.

### 2.5.1 Perovskite structure

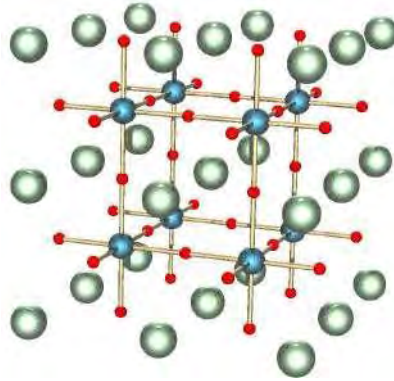


**Figure 2.5:** Structure of a perovskite with a chemical formula  $ABX_3$ . The red spheres are X atoms (usually oxygens), the blue spheres are B-atoms (a smaller metal cation, such as  $Ti^{4+}$ ), and the green spheres are the A-atoms (a larger metal cation, such as  $Ca^{2+}$ ). Pictured is the undistorted cubic structure; the symmetry is lowered to orthorhombic, tetragonal or trigonal in many perovskites [26].

A perovskite is any material with the same type of crystal structure as calcium titanium oxide ( $CaTiO_3$ ), known as the perovskite structure, or  $XII A^{2+V} B^{4+} X^{2-}$  with the oxygen in the face centers [25]. Perovskites take their name from the mineral, which was first discovered in the Ural Mountains of Russia by Gustav Rose in 1839 and is named after Russian mineralogist L. A. Perovski (1792-1856). The general chemical formula for perovskite compounds is  $ABX_3$ , where „A“ and „B“ are two cations of very different sizes, and X is an anion that bonds to both. The „A“ atoms are larger than the „B“ atoms. The ideal cubic-symmetry structure has the B cation in 6-fold coordination, surrounded by an octahedron of anions, and the A cation in 12-fold cuboctahedral coordination. The relative ion size requirements for stability of the cubic structure are quite stringent, so a slight of buckling and distortion can produce several lower symmetry distorted versions, in which the coordination numbers of A cations, B cations or both are reduced.

### 2.5.2 Structure of $BiFeO_3$

$BiFeO_3$  has rhombohedrally distorted perovskite structure. The oxygen octahedron is distorted with minimum and maximum O–O distances of 2.710 (7) and 3.015 (9) Å, respectively, and rotated by about  $\pm \alpha = 13.8 (3)^\circ$  around the threefold axis. The iron atom is shifted away from the centre of the deformed oxygen octahedron by about 0.134

(7) Å along the threefold axis. The bismuth atom is shifted with respect to two neighboring octahedron centres by about 0.540 (7) Å along the threefold axis. Bi-Fe distances are 3.0617 (11) and 3.8726 (11) Å. The oxygen atom is displaced by 0.2877 (6) Å away from the  $\text{Bi}_4$  plane. The iron-oxygen chain has angles of  $165.04 (21)^\circ$  (O-Fe-O) and  $154.1 (4)^\circ$  (Fe-O-Fe), and dihedral angles of  $127.8 (9)^\circ$  (O-Fe-O-Fe) and  $121.6(9)^\circ$  (Fe-O-F-O).

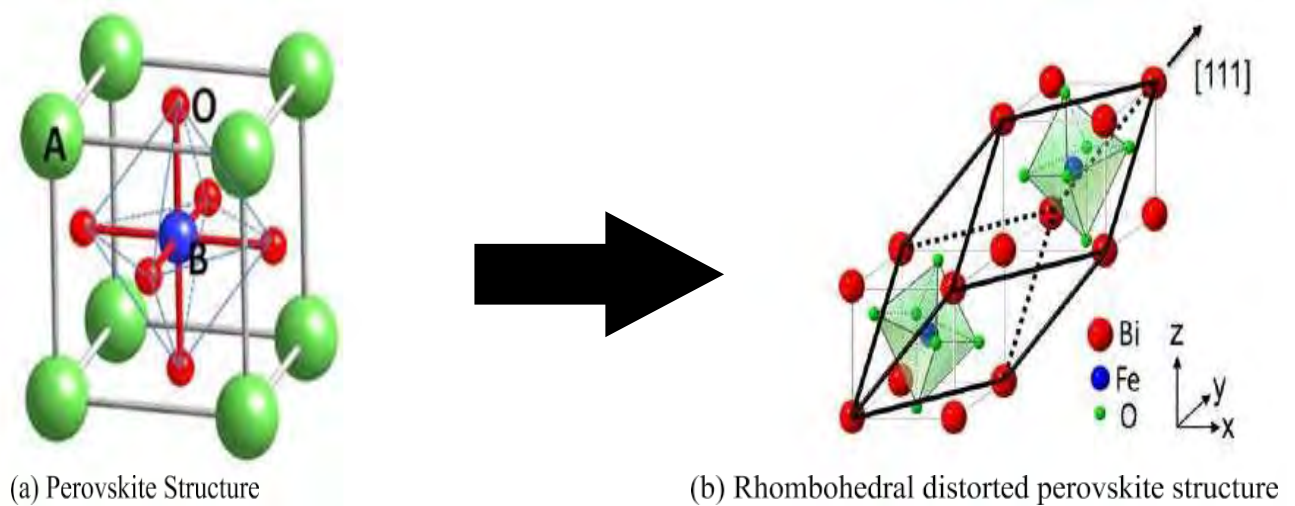


**Figure 2.6:** (a) Structure of a perovskite with a chemical formula  $\text{ABO}_3$  (b) rhombohedrally distorted perovskite structure

## 2.6 Magnetism

Magnetism is a class of physical phenomena that are mediated by magnetic fields. Electric currents and the magnetic moments of elementary particles give rise to a magnetic field, which acts on other currents and magnetic moments. Every material is influenced to some extent by a magnetic field. The most familiar effect is on permanent magnets, which have persistent magnetic moments caused by ferromagnetism. The prefix ferro refers to iron, because permanent magnetism was first observed in a form of natural iron ore called magnetite,  $\text{Fe}_3\text{O}_4$ . Most materials do not have permanent moments. Some are attracted to a magnetic field (paramagnetism); others are repulsed by a magnetic field (diamagnetism); others have a more complex relationship with an applied magnetic field (spin glass behavior and antiferromagnetism). Substances that are negligibly affected by magnetic fields are known as non-magnetic substances. These include copper, aluminium,

gases, and plastic. Pure oxygen exhibits magnetic properties when cooled to a liquid state. The magnetic state (or magnetic phase) of a material depends on temperature and other variables such as pressure and the applied magnetic field. A material may exhibit more than one form of magnetism as these variables change.

### 2.6.1 Origin of magnetism

The origin of magnetism lies in the orbital and spin motions of electrons and how the electrons interact with one another. The best way to introduce the different types of magnetism is to describe how materials respond to magnetic fields. It is just that some materials are much more magnetic than others. The main distinction is that in some materials there is no collective interaction of atomic magnetic moments, whereas in other materials there is a very strong interaction between atomic moments. The magnetic moment of an electron in an orbit is given by

$$\mu = \pi r^2 \frac{ev}{2\pi r} = \frac{evr}{2} \quad (2.5)$$

Where  $r$  is the radius of orbit,  $e$  is charge and  $v$  is the velocity. The angular momentum of an electron must be an integral multiple of Planck's constant.

$$mvr = \frac{nh}{2} \quad (2.6)$$

Where  $m$  is the mass and  $h$  is the Planck's constant. If the electron revolves in the first orbit then  $n=1$

Therefore orbital magnetic moment of an electron can be given from (2.5) and (2.6)

$$\mu = \frac{eh}{4\pi m} \quad (2.7)$$

This is known as Bohr magneton, the smallest possible orbital magnetic moment. A simple electromagnet can be produced by wrapping copper wire into the form of a coil and connecting the wire to a battery. A magnetic field is created in the coil but it remains there only while electricity flows through the wire. The field created by the magnet is associated with the motions and interactions of its electrons, the minute charged particles which orbit

## Chapter 2: Theoretical background

---

the nucleus of each atom. Electricity is the movement of electrons, whether in a wire or in an atom, so each atom represents a tiny permanent magnet in its own right. The circulating electron produces its own orbital magnetic moment, measured in Bohr magnetons ( $\mu_B$ ), and there is also a spin magnetic moment associated with it due to the electron itself spinning, like the earth, on its own axis (illustrated in Figure 2.7). In most materials there is resultant magnetic moment, due to the electrons being grouped in pairs causing the magnetic moment to be cancelled by its neighbor. In certain magnetic materials the magnetic moments of a large proportion of the electrons align, producing a unified

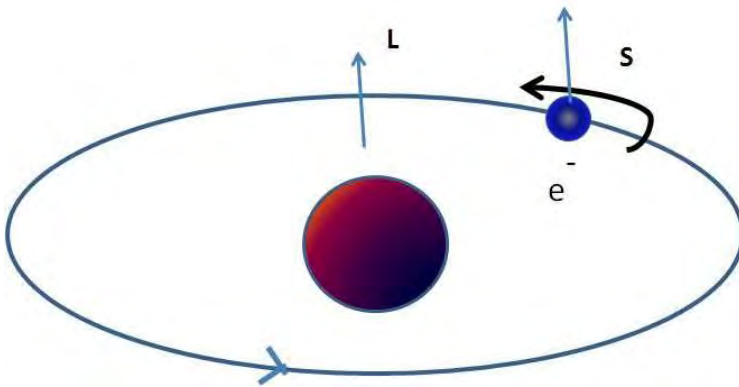


**Figure 2.7:** A spin magnetic moment associated with it due to the electron itself like the earth on its own axis.

magnetic field. The field produced in the material (or by an electromagnet) has a direction of flow and any magnet will experience a force trying to align it with an externally applied field. The smallest possible magnetic moment due to spin of the electron is

$$\mu = \frac{eh}{4\pi m} \quad (2.7)$$

According to quantum theory the spin of electrons have only two possibilities,  $+1/2$  or  $-1/2$ .

Similar to Eqn. (2.6) we can write in the form

$$\mu = \frac{eS}{2m} \quad (2.8)$$

where  $S$  is the spin quantum number. In short,

$$\mu = g\left(\frac{e}{2m}\right)S \quad (2.9)$$

here  $g$  is the term known as  $g$ -factor. When  $g = 2$ , the spin contribution arises and when  $g = 1$  the orbital contribution arises. The mass of the nucleus is so large that the magnetic moment contribution can be neglected compared to the electronic magnetic moment. The gyromagnetic ratio is proportional to the  $g$ -factor and „ $g$ “ arises due to the precession of the electrons similar to the precession of a top in a gravitational force. The value of  $g$  tells us whether the origin of magnetic moment is spin or orbital motion of electrons.

### 2.6.2 Magnetic moment of atoms

The strength of a magnetic dipole, called the magnetic dipole moment, may be thought of as a measure of a dipole's ability to turn itself into alignment with a given external magnetic field. In a uniform magnetic field, the magnitude of the dipole moment is proportional to the maximum amount of torque on the dipole, which occurs when the dipole is at right angle to the magnetic field [27]. The magnetic moment or magnetic dipole moment is a measure of the strength of a magnetic source. In the simplest case of a current loop, the magnetic moment is defined as:

$$\mu_m = I \int da \quad (2.10)$$

Where  $a$  is the vector area of the current loop, and the current,  $I$  is constant. By convention, the direction of the vector area is given by the right hand rule (moving one's right hand in the current direction around the loop, when the palm of the hand is touching the loop's surface, and the straight thumb indicates the direction). In the more complicated case of a spinning charged solid, the magnetic moment can be found by the following equation:

$$\vec{\mu}_m = \frac{1}{2} \int \vec{r} \times \vec{J} d\tau \quad (2.11)$$

where,  $d\tau = r^2 \sin\theta \, dr \, d\theta \, d\varphi$ ,  $J$  is the current density. Magnetic moment can be explained by a bar magnet which has magnetic poles of equal magnitude but opposite polarity. Each is the source of magnetic force which weakens with distance. Since magnetic poles come in pairs, their forces interfere with each other because while one pole pulls, the other repels.

## Chapter 2: Theoretical background

---

This interference is greatest when the poles are close to each other i.e. when the bar magnet is short. The magnetic force produced by a bar magnet, at a given point in space, therefore depends on two factors: on both the strength  $P$  of its poles and on the distance  $d$  separating them. The force is proportional to the product,  $\mu = PR$ , where,  $\mu$  describes the magnetic moment or dipole moment of the magnet along a distance  $R$  and its direction as the angle between  $R$  and the axis of the bar magnet. Magnetism can be created by electric current in loops and coils so any current circulating in a planar loop produces a magnetic moment whose magnitude is equal to the product of the current and the area of the loop. When any charged particle is rotating, it behaves like a current loop with a magnetic moment. The equation for magnetic moment in the current-carrying loop, carrying current  $I$  and of area vector  $\vec{a}$  for which the magnitude is given by:

$$\vec{\mu}_m = I\vec{a} \quad (2.12)$$

where,  $\mu_m$  is the magnetic moment, „ $\vec{a}$ “ vector measured in ampere-square meters, or equivalent joules per Tesla,  $I$  is the current, a scalar measured in amperes, and is the loop area vector, having as  $x$ ,  $y$  and  $z$  coordinates the area in square meters of the projection of the loop into the  $yz$ -,  $zx$ - and  $xy$ -planes.

### 2.6.3 Magnetic moment of electrons

The electron is a negatively charged particle with angular momentum. A rotating electrically charged body in classical electrodynamics causes a magnetic dipole effect creating magnetic poles of equal magnitude but opposite polarity like a bar magnet. For magnetic dipoles, the dipole moment points from the magnetic south to the magnetic north pole. The electron exists in a magnetic field which exerts a torque opposing its alignment creating a potential energy that depends on its orientation with respect to the field. The magnetic energy of an electron is approximately twice what it should be in classical mechanics. The factor of two multiplying the electron spin angular momentum comes from the fact that it is twice as effective in producing magnetic moment. This factor is called the electronic spin  $g$ -factor. The persistent early spectroscopists, such as Alfred Lande, worked out a way to calculate the effect of the various directions of angular momenta. The resulting geometric factor is called the Lande  $g$ -factor. The intrinsic magnetic moment of a particle with charge  $q$ , mass  $m$ , and spin  $s$ , is

$$\vec{\mu}_m = \frac{q}{2m} \vec{s} \quad (2.13)$$

where, the dimensionless quantity  $g$  is called the  $g$ -factor. The  $g$ -factor is an essential value related to the magnetic moment of the subatomic particles and corrects for the precession of the angular momentum. One of the triumphs of the theory of quantum electrodynamics is its accurate prediction of the electron  $g$  factor, which has been experimentally determined to have the value 2.002319. The value of 2 arises from the Dirac equation, a fundamental equation connecting the electron's spin with its electromagnetic properties, and the correction of 0.002319, called the anomalous magnetic dipole moment of the electron, arises from the electron's interaction with virtual photons in quantum electrodynamics. Reduction of the Dirac equation for an electron in a magnetic field to its non-relativistic limit yields the Schrödinger equation with a correction term which takes account of the interaction of the electron's intrinsic magnetic moment with the magnetic field giving the correct energy. The total spin magnetic moment of the electron is

$$\vec{\mu}_s = -g_s \mu_b \vec{s} / \hbar \quad (2.14)$$

where  $g_s = 2$  in Dirac mechanics, but is slightly larger due to Quantum Electrodynamics effects,  $\mu_m$  is the Bohr magneton and  $s$  is the electron spin. The  $z$  component of the electron magnetic moment is

$$\vec{\mu}_z = -g_s \mu_b \vec{m}_s \quad (2.15)$$

where,  $m_s$  is the spin quantum number. The total magnetic dipole moment due to orbital angular momentum is given by

$$\mu_s = -\frac{e}{2m_e} L = -\mu_b \sqrt{l(l+1)} \quad (2.16)$$

where,  $\mu_B$  is the Bohr magneton. The  $z$ -component of the orbital magnetic dipole moment for an electron with a magnetic quantum number  $m_l$  is given by

$$\vec{\mu}_z = -\mu_b \vec{m}_l \quad (2.17)$$

### 2.6.4 Magnetic Behavior

The magnetic properties of a matter are fundamentally the result of the electrons of the

atom, which have a magnetic moment by means of the electron motion. There are two types of electronic motion, spin and orbital, and each has a magnetic moment associated with it. Since the response of a material to a magnetic field (H) is the characteristic of the magnetic induction or the flux density (B) and the effect that a material has upon the magnetic induction in a magnetic field is represented by the magnetization (M). Thus a universal equation can be established, relating these three magnetic quantities, by

$$\vec{B} = \mu_0(\vec{H} + \vec{M}) \quad (2.18)$$

$$\vec{B} = \mu_0\vec{H} \quad (2.19)$$

where,  $\mu_0$  is a universal constant of permeability in a free space and is the permeability of a material. In equation (2.19), one can see that  $\mu_0\vec{H}$  is the magnetic induction generated by the field alone and  $\mu_0\vec{M}$  is the additional magnetic induction contributed by a material. The magnetic susceptibility ( $\chi$ ) is defined as the ratio of magnetization to magnetic field

$$\chi = \frac{\vec{M}}{\vec{H}} \quad (2.20)$$

The permeability and susceptibility of a material is correlated with respect to each other by

$$\mu = \mu_0 (1 + \chi) \quad (2.21)$$

The magnetic behavior of materials can be classified into the following five major groups:

- ❖ Diamagnetism
- ❖ Paramagnetism
- ❖ Ferromagnetism
- ❖ Antiferromagnetism
- ❖ Ferrimagnetism

### 2.6.5 Magnetic hysteresis loop

In addition to the Curie temperature and saturation magnetization, ferromagnets and ferrimagnets can retain a memory of an applied field once it is removed. This behavior is called hysteresis and a plot of the variation of magnetization with magnetic field is called a hysteresis loop (Figure 2.8).

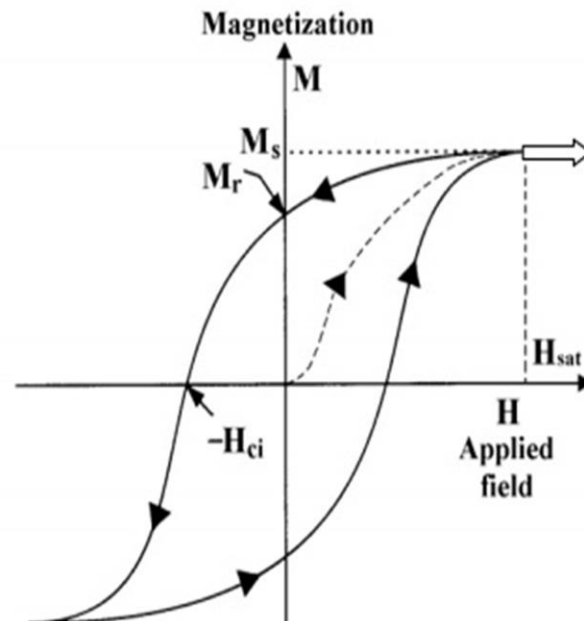


**Figure 2.8:** Hysteresis loop for a ferromagnetic material

The performance of any magnetic material can be defined with the help of this hysteresis loop.  $M_s$  is the saturation magnetization and is a measure of how strongly the material can be magnetized.  $M_r$  is the remanent magnetization which is the residual, permanent magnetization left after the removal of the applied field. In order to demagnetize the specimen from its remanent state, a reverse field  $H_{ci}$ , the coercive field is required to reduce the residual magnetization to zero. Depending on the value of the coercive field, ferromagnetic materials are classified as hard or soft. A hard magnet needs a large field to reduce its residual magnetization to zero, and for a soft magnet a small field is required to reduce its residual magnetization to zero. Hard and soft magnetic materials obviously have totally complementary applications. The various hysteresis parameters are not solely intrinsic properties but are dependent on grain size, domain state, stresses, and temperature.

### 2.6.6 Cause of magnetic hysteresis loop

It is well known that if a specimen of iron or steel is subjected to cold working the hysteresis loss and the coercivity increase (Figure 2.9). It is also well known that the addition of other non-magnetic elements to iron such as carbon in making steel increases the hysteresis loss and coercivity. These empirical facts were known long before theories of hysteresis were suggested. From these results it would appear that

## Chapter 2: Theoretical background

„imperfections“, whether in the form of dislocations or impurity elements in the metal, cause an increase in the energy lost during the magnetization process, in the form of a kind of internal friction. It is these „imperfections“ which give rise to hysteresis. Another mechanism which gives rise to hysteresis is caused by magnetocrystalline anisotropy. Ferromagnetic materials with higher anisotropy have greater hysteresis.

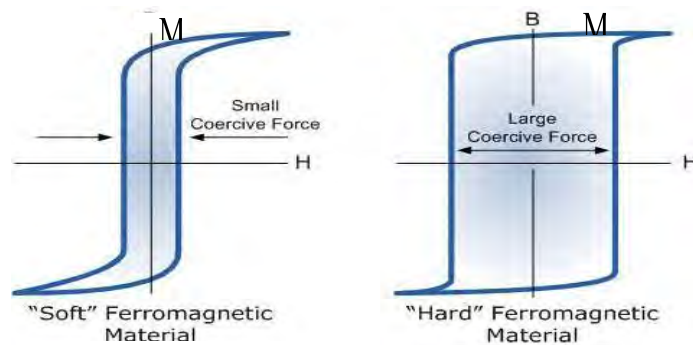


**Figure 2.9:** Dependence of the hysteresis loop of iron or steel on hardness caused by the addition of carbon or other non-magnetic material or by cold working.

This is well known by those working with permanent magnets. In an anisotropic solid certain crystallographic axes are favored by the magnetic moments which will prefer to lie along these directions as this leads to a lower energy. The magnetic moments can be dislodged from the direction they are occupying by application of a magnetic field but when this occurs they jump to crystallographically equivalent axes which are closer to the field direction, and hence of lower energy. This results in discontinuous and irreversible rotation of the magnetic moments which leads to a kind of switching action.

## 2.7 Ferroelectric behavior

The phenomenon of ferroelectricity was discovered in 1921 by J. Valasek who was investigating the dielectric properties of Rochelle salt ( $\text{NaKC}_4\text{H}_4\text{O}_6 \cdot 4\text{H}_2\text{O}$ ). Barium titanate ( $\text{BaTiO}_3$ ) was discovered to be ferroelectric in 1944 by A von Hippel and is perhaps the most commonly thought of material when one thinks of ferroelectricity. While there are some 250+ materials that exhibit ferroelectric properties, some of the more common/significant materials include: Lead titanate ( $\text{PbTiO}_3$ ), Lead zirconate

## Chapter 2: Theoretical background

titanate (PZT), Lead lanthanum zirconate titanate (PLZT), Bismuth Ferrite ( $\text{BiFeO}_3$ ). All ferroelectric materials are pyroelectric, however, not all pyroelectric materials are ferroelectric. Below a transition temperature called the Curie temperature ferroelectric and pyroelectric materials are polar and possess a spontaneous polarization or electric dipole moment. However, this polarity can be reoriented or reversed fully or in part through the application of an electric field with ferroelectric materials. Complete reversal of the spontaneous polarization is called switching. The non-polar phase encountered above the Curie Temperature is known as the paraelectric phase. The direction of the spontaneous polarization conforms to the crystal symmetry of the material while the reorientation of the spontaneous polarization is a result of atomic displacements. The magnitude of the spontaneous polarization is greatest at temperatures well below the Curie temperature and approaches zero as the Curie temperature is neared.

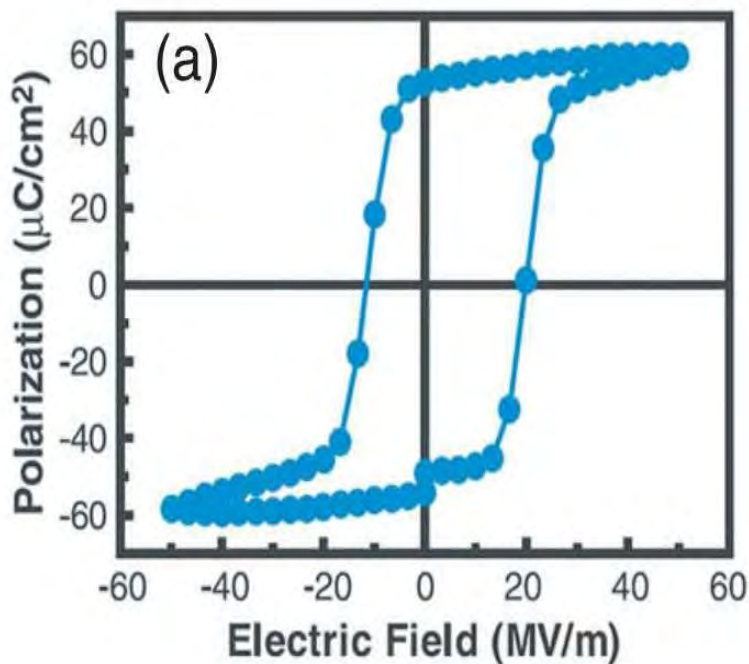


**Figure 2.10:** A typical room temperature ferroelectric hysteresis measured along the pseudo-cubic [001]-axis. The full polarization, pointing along the pseudo-cubic [111]-axis, should be 3 times larger [32]

### 2.7.1 Process of Polarization

The formation of an electric dipole or polarization can happen in a number of process or mechanisms [33]. At different frequency regimes, each one contributes to dielectric response and their involvement are in different polarizable species. The basic mechanism

or processes are

- ❖ Electronic polarization
- ❖ Ionic or atomic polarization
- ❖ Orientation polarization
- ❖ Space charge polarization

### 2.7.1.1 Electronic polarization

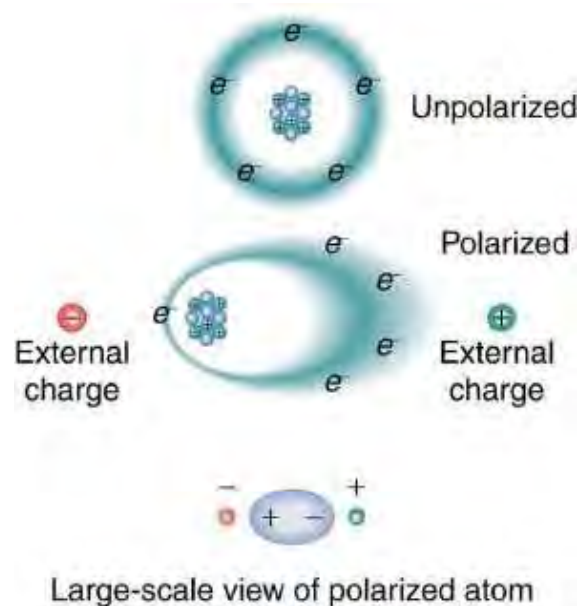


**Figure 2.11:** Electronic polarization.

Electronic polarization occurs in all dielectric materials. Upon an external electric field, being applied a slight relative shift of positive and negative electric charge in opposite directions occurs within an insulator, or dielectric. Polarization occurs when the induced electric field distorts the negative cloud of electrons around positive atomic nuclei in a direction opposite the field. This slight separation of charge makes one side of the atom somewhat positive and the opposite side somewhat negative. As soon as the electric field is removed, the electrons and nuclei return to their original position and the polarization disappears.

### 2.7.1.2 Atomic polarization

It is also known as ionic polarization. It involves the displacement of positive and

negative ions in relation to one another within crystal structure when an electric field is applied. The magnitude of the dipole moment for each ion pair  $P_i$  is equal to the product of the relative displacement  $d_i$  and the charge on each ion as

$$P_i = qd_i \quad (2.22)$$

Various popular effects like piezoelectricity, pyroelectricity, ferroelectricity etc occurs by ionic polarization phenomena. Wide range of polarization effects are possible through this mechanism depending upon the crystal structure, solid solution and various other factors. Ionic polarization is inversely proportional to the mass of the ions and square of the natural frequency of vibration of the ions. Covalently bonded ceramics do not show ionic polarization due to lack of charged atoms, but ionic bonded structures show ionic polarization. The frequency with which ions are displaced is of the same order as the lattice vibration frequency  $\sim 10^{13}$  Hz. It is observed in ionic crystals and occurs up to the infrared region  $10^{10} - 10^{13}$  Hz.

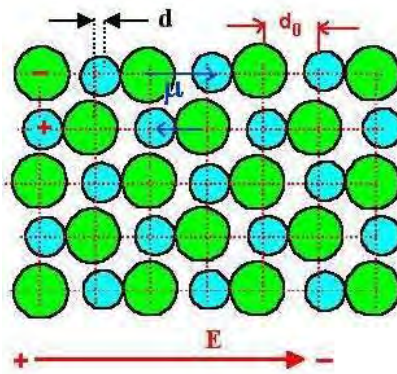
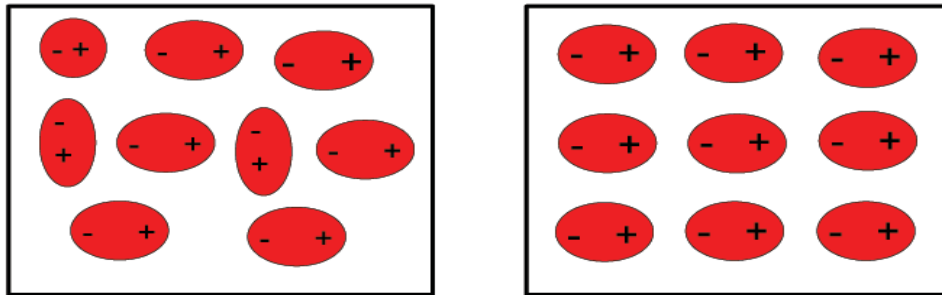


Figure 2.12: Atomic polarization.

### 2.7.1.3 Dipolar polarization

This mode of polarization is mainly attributed to the unequal charge distribution between partners in a molecule or complex ion. When a field is applied, these tend to line up with the electric dipoles in the direction of the field, giving rise to an orientation polarization. That is why, this polarization is found only where substance possesses permanent dipole moments. Upon electric field, these permanent moments rotate into the direction of the applied field, therefore contribute to the dipolar polarization. The tende-

ncy to alignment is counterbalanced by thermal vibrations of the atoms such that the polarization decreases with the increasing temperature.



**Figure 2.13:** Dipolar polarization.

Dipolar polarization occurs at lower frequencies of the field and thus can greatly affect the capacitive and insulating properties of glasses and ceramics in low frequency applications. Dipolar polarization is known as orientational polarization and it is both frequency and temperature dependent.

**2.7.1.4 Space charge polarization**

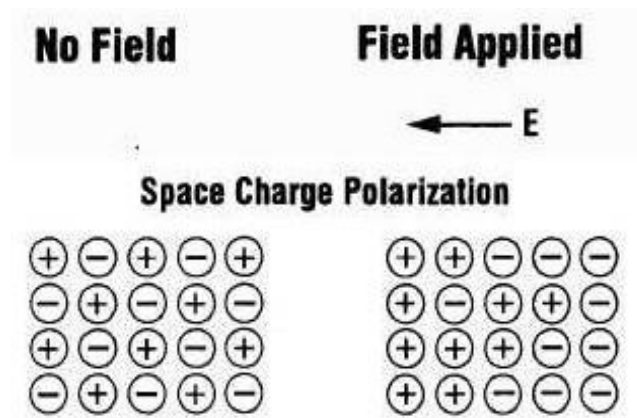


**Figure 2.14:** Space charge polarization.

The final source of polarization is mobile charges which are present because they are impeded by interfaces, because they are not supplied at an electrode or discharged at an electrode. Or they are trapped in the material during fabrication process. Space charges resulting from these phenomena appear as an increase in capacitance as far as the exterior circuit is concerned. Space charge polarization occurs at low frequencies (50-60 Hz). A type of polarization is known as Maxwell-Wagner polarization which is related to the space charge polarization, as this type of polarization is occurred within

## Chapter 2: Theoretical background

the frequency range ( $10^{-10}$  -  $10^4$  Hz). The dielectric response of solids is a complex function of frequency, temperature, and type of solid. Under dc conditions all mechanism operates and the maximum polarization results which eventuates to the maximum of dielectric constants. An ideal dielectric is supposed to adjust itself instantaneously to any change in voltage. However in practice there is inertia to charge movement that shows up as a relaxation time for charge transport. When the frequency of the applied field increases the mechanisms start to fade out and the value of polarizability starts.

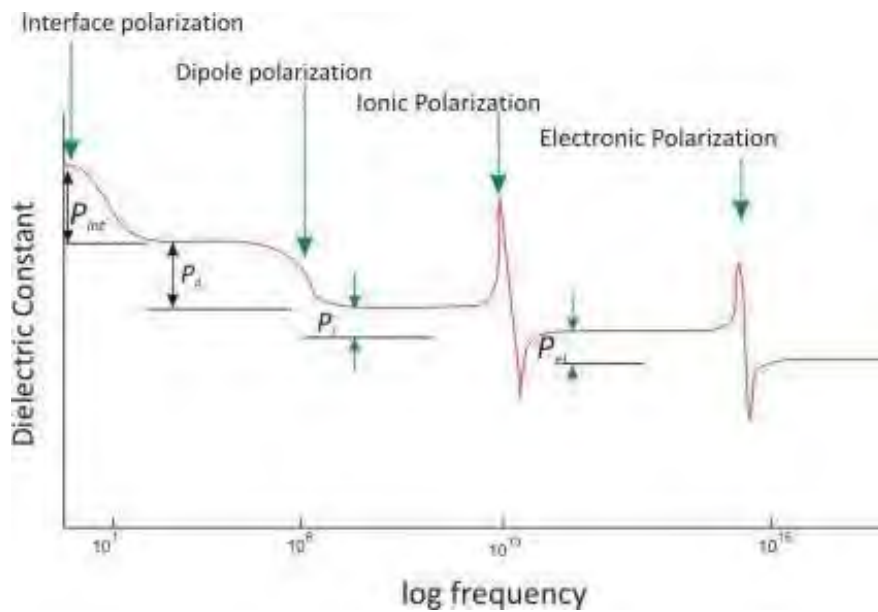


**Figure 2.15:** Variation of polarization with frequency.

It is already been noticed that the electronic polarization is the only process that can follow the rapid change in the alternate field so to cause a variation in the polarizability. That is why this is still operative in the visible range of the spectrum. Ionic polarization processes are able to follow an applied high frequency field and contribute to the dielectric constant at frequencies up to infrared region of the spectrum. Dipolar and space charge polarization have relaxation time corresponding to the particular system and process but in general participate and contribute only at lower frequencies.

### 2.7.2 Ferroelectricity in $\text{BiFeO}_3$

Bulk  $\text{BiFeO}_3$  is known to be exhibited ferroelectric ordering below Curie temperature

$T_c \sim 1103$  K. Both X-ray and neutron diffraction studies confirmed the ferroelectric phase of BFO. The origin of ferroelectricity in BFO can be understood its highly distorted perovskite structure with rhombohedral symmetry and space group  $R3c$ . As shown in Figure 2.16, the primitive unit cell contains two formula units (ten atoms), arising from counter rotations of neighboring oxygen octahedra around  $[111]$  axis [34]. The  $R3c$  symmetry allows development of a spontaneous polarization along  $[111]$  di-

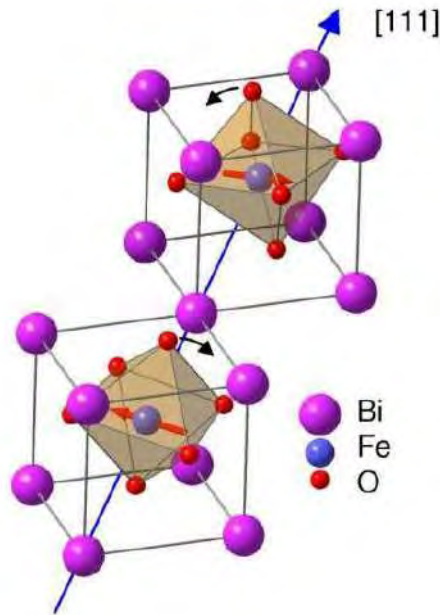


**Figure 2.16:** Crystal structure of bulk  $\text{BiFeO}_3$  with opposite rotation of successive oxygen octahedral around  $[111]$  polar axes. Red arrow indicates orientation of Fe magnetic moments in  $(111)$  plane.

rection in such a way that Bi, Fe, and O are displaced relative to one another along the  $[111]$  axis [34]. The largest relative displacements take place in Bi relative to O, which is consistent with a stereochemically active Bi  $6s^2$  lone pair compared to cubic perovskite [35]. The polar displacements in BFO are very large in comparison of non lone-pairactive perovskite ferroelectrics such as  $\text{BaTiO}_3$  and  $\text{KNbO}_3$ , but consistent with those observed for other bismuth based perovskite structures [36]. According to first principle calculations, it has been reported that BFO has a large spontaneous polarization ( $P_s$ ) of the order  $\sim 90\text{-}100 \mu\text{C}/\text{cm}^2$  for a rhombohedral structure with  $R3c$  space group and around  $150 \mu\text{C}/\text{cm}^2$  for tetragonal structure. But, experimentally observed spontaneous polarization is found to be much lesser than theoretically

predicted values [37]. This discrepancy in the values of polarization is attributed to the presence of secondary phases, defects, volatilization of the bismuth atoms at high temperatures, electron hopping between Fe ions that lead to high leakage current.

## 2.8 Photocatalytic activity

Photodegradation includes photo dissociation, the breakup of molecules into smaller pieces by photons. It also includes the change of a molecule's shape to make it irreversibly altered, such as the denaturing of proteins, and the addition of other atoms or molecules [38]. A common photodegradation reaction is oxidation. This type of photodegradation is used by some drinking water and wastewater facilities to destroy pollutants.

A simple and interesting approach to extend the catalyst absorption toward visible region is the photosensitization by an appropriate dye. The dye can absorb the visible light to reach an excited state. The dye in the excited state has in general lower redox potential than the corresponding ground state. If the redox potential is lower than the conduction band of photocatalyst being used, an electron may be injected from the excited state into the conduction band, and consequently the cationic radicals and conduction band electron are formed. This process has been intensively investigated in photoelectrochemical cells (the Gratzel cell) in the absence of molecular di oxygen. However, in the presence of dioxygen, the dye itself can undergo an effective degradation. Such degradation would be desired if the dye is a target organic pollutant.

### 2.8.1 Photocatalysis

It is the acceleration of a photoreaction in the presence of a catalyst. In catalyzed photolysis, light is absorbed by the substrate. In photogenerated catalysis, the photocatalytic activity (PCA) depends on the ability of the catalyst to create electron-hole pairs, which generate free radicals (hydroxyl radicals: OH) able to undergo secondary reactions [39]. Photocatalysis is a fantastic way to clean facilities, houses, and living environments. By modifying and further developing this technology, we can reduce pollution in our air and water. We can even reduce the spread of infections and diseases

such as SARS in hospitals. This cleaner way of life would benefit everyone around the world. The word photocatalysis is composed of two parts: (i) The prefix photo, defined as “light”, (ii) Catalysis is the process where a substance participates in modifying the rate of a chemical transformation of the reactants without being altered in the end. This substance is known as the catalyst which increases the rate of a reaction by reducing the activation energy. Hence, photocatalysis is a reaction which uses light to activate a substance which modifies the rate of a chemical reaction without being involved itself. Photocatalysis is a preferred and more advanced technique than conventional organic synthesis due to following reasons:-

- ❖ In photocatalytic reactions, both oxidation and reduction occurs simultaneously on the photocatalyst particles but in conventional reactions we need different oxidizing agent and reducing agent.
- ❖ Also in photochemical reactions, there is not much need of solvents which are expensive and are difficult to dispose of. We generally use water, but in conventional reactions many solvents are used.
- ❖ Photochemical reaction is a single step reaction, we can get our product just by mixing the reactant and irradiating them but conventional reactions are multi-step reactions.
- ❖ Photocatalytic reactions occur at ambient temperature and pressure so need not to maintain drastic conditions as required in conventional reactions.

### 2.8.2 Photocatalysts

Environmental contamination, which is growing around the world or in our daily home life, is a serious social problem not to be neglected [40]. Water pollution caused by industrial and household wastes and respiratory diseases caused by air pollutants such as SO<sub>x</sub> or NO<sub>x</sub> are the best examples of such contamination. The fact that using energy to eliminate such environmental contamination increases emission of CO<sub>2</sub> resulting in more global warming, however, leads us to a dilemma not to use energy to achieve our anti-pollution goal. Under such circumstances, that we need a new material that can gently harmonize the contaminated environment to restore original conditions by using

natural energy which is a part of the environment and low-cost energy supplied to our daily home life. Photocatalyst produces surface oxidation to eliminate harmful substances such as organic compounds or nearby bacteria, when it is exposed to the sun or fluorescent lamp. By applying this principle to water treatment, dissolving NO<sub>x</sub> in the air, or room air purification, photocatalyst can be used for various steps in purifying a contaminated environment. The function of the photocatalyst can be divided into five major categories as follows:

- ❖ Purifying water
- ❖ Preventing contamination
- ❖ Anti-bacteria
- ❖ Deodorizing
- ❖ Purifying the air (dissolving NO<sub>x</sub>)

It might be well understood that the functions listed above are those which amplify or accelerate the functions of the sun, or ultraviolet radiation. In this sense, it is not strange to regard zinc oxide as a photocatalyst from the viewpoint that it works as the catalyst in accelerating the functions of the light. Photocatalyst has the following advantages over any current air purification technologies:

- ❖ Real destruction of pollutant rather than a simple transfer on a substrate
- ❖ Degradation of pollutant at ambient temperature and pressure
- ❖ Build with easily available materials and by means of well-known techniques
- ❖ Economical, cheap and low energy consumption
- ❖ Adapted for a large range of pollutant (VOC, bacteria, mold)

### **2.8.3 Parameters affecting photocatalysis**

Degradation mechanism takes place on the surface of the photocatalyst. The concentration of the adsorbate directly affects the photocatalytic degradation rate of the pollutants to be degraded [41,42]. Photocatalytic degradation rate is linearly dependent with light intensity at low intensities. It depends on the square root of light intensity for medium intensities. At high intensities photocatalytic degradation rate is independent of the intensity of light [43,44]. The effect of pH on photocatalytic degradation varies due to

the kind of materials used and the kind of adsorbed pollutant [45]. Increasing or decreasing pH affects the adsorption of the pollutant and thus, the degradation rate. pH affects the surface charge of the photocatalyst and the ionizability of the pollutant. Adsorption is enhanced at lower pH values. Strongly adsorbed pollutants degrade faster. At higher pH values above pH 9, degradation rate is also enhanced due to the increased OH<sup>-</sup> anions on the photocatalyst surface. Therefore all these rates depend on the type of catalyst and the adsorbed pollutant [41,46,47]. The particle size of photocatalysts is an important parameter that affects photocatalytic activity. Decreasing the size of the catalyst, surface to volume ratio is increased, thus photocatalytic activity is increased. [48].

The surface properties of nanosized photocatalysts also affect the photocatalytic activity. It was shown that surface morphology and crystal structure have a direct effect on the photocatalytic activity of TiO<sub>2</sub> sol-gel films. Heat treatment can modify crystal structure leading to an increased photocatalytic activity [49]. The degradation mechanism is promoted with the absorption of light by the nanosized photocatalyst. In optical activation, electrons are excited from the valence band to the conduction band leading to e-h pair formation. The photon energy of the incident light should be above the band gap energy of the materials. So activation wavelength is an important parameter for the photocatalytic reactions. Most commonly used photocatalysts are wide band gap semiconductors that can be activated in UV light. However electromagnetic radiation of sun has only 7 percent UV content that strikes the atmosphere, which decreases more during penetrating the atmosphere [50]. According to Sasaki [51], the UV part of solar radiation detected on the Earth in 1990-1992 was not more than 0.145 percent at 290-320 nm and 4.1 percent at 320-400 nm.

### **2.8.4 Nanosized materials**

Many properties of photochemical processes change as the materials change scale from bulk to nanorange. Nanosized particles exhibit special magnetic, photochemical, photophysical, and electrophysical properties. When materials are in the nanoscale regime, their size has significant effects on their properties. Changing the size of such nanoparticles opens up the opportunity to control their characteristics [52]. Varying particle size strongly affects the

photodegradation experiment and the resulting processes. These processes depend on the optical absorption of light, dynamics of photogenerated exciton, the consequences of electron-hole recombination, and the photochemical reactions in the presence of reagents adsorbed on the surface of the particles [53].

The size effects in nanoparticles can be divided into two. The first one is the result of increased surface to volume ratio and change in surface roughness is observed in nanoparticles of 10-100 nm in size. The other is the change in the electronic state of the materials due to the quantum size effects dominating especially below a critical size (10 nm) at room temperature. The critical size, which is the threshold for the quantum size effects, differs for different materials, depending on the chemical structure of the nanoparticle. It is comparable to De Broglie wavelength of the free electron [54].

### **2.8.5 BiFeO<sub>3</sub> nanoparticles as a photocatalyst**

In the present days, the perovskite type BiFeO<sub>3</sub> nanoparticles has gained considerable attention as a promising photocatalyst due to its visible light response (band gap energy eV), good chemical stability [56] and intrinsic electric polarization field which can enable charge-carrier separation within the semiconducting structure. [57]

# Bibliography

- [1] Maxwell, J. C., “A Dynamical Theory of the Electromagnetic Field”, *Phil. Trans. R. Soc. L.*, 155, 459, 1865
- [2] Landau, L. D., Lifshitz, E. M., *Electrodynamics of continuous media* (Fizmatlit, Moscow, 1959)
- [3] Schmid, H., “Multi-ferroic magnetoelectrics, Ferroelectrics”, 162, 317, 1994.
- [4] Lazenka, V. V., Zhang, G., Vanacken, J., Makoed, I. I., Ravinski A. F., and Moshchalkov, V. V., “Structural transformation and magnetoelectric behaviour in  $\text{Bi}_{1-x}\text{Gd}_x\text{FeO}_3$  multiferroics”, *J. Phys. D: Appl. Phys.*, Vol - 45, pp - 125002 - 125007, 2012.
- [5] Ascher, E., Rieder, H., Schmid, H., and Stössel, H., “Some properties of ferromagnetoelectric nickeliodine boracite,  $\text{Ni}_3\text{B}_7\text{O}_{13}\text{I}$ ”, *J. App. Phys.*, 37, 1404, 1966.
- [6] Wang, J., Neaton, J. B., Zheng, H., Nagarajan, V., Ogale, S. B., Liu, B., Viehland, D., Vaithyanathan, V., Schlom, D. G., Waghmare, U. V., Spaldin, N. A., Rabe,
- [7] Yasui, Y., Sato, K., Kobayashi, Y., and Sato, M., (2009). “Studies of Multiferroic System  $\text{LiCu}_2\text{O}_2$ : I. Sample Characterization and Relationship between Magnetic Properties and Multiferroic Nature”, *J. Phys. Soc. Jpn.*, 78, 084720, 2009.
- [8] Seshadri, R. and Hill, N. A., “Visualizing the role of Bi 6s lone pairs in the off-center distortion in ferromagnetic  $\text{BiMnO}_3$ ”, *Chem. Mater.* 13, 2892, 2001.
- [9] Kiselev, S. V., Ozerovo, R. P., and Z.,Hdanovz, G. S., “Detection of magnetic order in ferroelectric  $\text{BiFeO}_3$  by neutron diffraction”, *Sov. Phys. Dokl.* 7, 742, 1963.
- [10] Efremov, D. V., Brink, J. V. D., and Khomskii, D. I., “Bond-versus site-centred ordering and possible ferroelectricity in manganites”, *Nat. Mater.* 3, 853, 2004.
- [11] Kartavtsevaa, M.S., Gorbenkoa, O. Yu., Kaula, A. R., Murzinaa, T. V., Savinova, S. A., and Aktsipetrova, O. A., “Strain-induced effects in phase transitions in thin films of multiferroic  $\text{BiFeO}_3$  probed by optical second-harmonic generation”, *J. of Mater. Res.*, 22, 2063, 2007.

## Chapter 2: Theoretical background

---

- [12] Jia, C., Onoda, S., Nagaosa, N., and Han, J. H., “Bond electronic polarization induced by spin”, *Phys. Rev. B*, 74, 224444, 2006.
- [13] Jia, C., Onoda, S., Nagaosa, N., and Han, J. H., “Microscopic theory of spin-polarization coupling in multiferroic transition metal oxides”, *Phys. Rev. B*, 76, 144424, 2007.
- [14] Chapon, L. C., Radaelli, P. G., Blake, S. Park, G. R., and Cheong, S.-W., “Ferroelectricity Induced by Acentric Spin-Density Waves in  $\text{YMn}_2\text{O}_5$ ”, *Phys. Rev. Lett.*, 96, 097601, 2006.
- [15] Sergienko, I. A., en, C., and Dagotto, E., “Ferroelectricity in the Magnetic E-Phase of Orthorhombic Perovskites”, *Phys. Rev. Lett.*, 97, 227204, 2006.
- [16] Anderson, P. W., “Antiferromagnetism. Theory of Superexchange Interaction”, *Phys. Rev.*, 79, 350, 1950.
- [17] Goodenough, J. B., “Theory of the Role of Covalence in the Perovskite-Type Manganites [La, M(II)]  $\text{MnO}_3$ ”, *Phys. Rev.* 100, 564 (1955).
- [18] Kanamori, J., “Superexchange interaction and symmetry properties of electron orbitals”, *J. Phys. Chem. Solids*, 10, 87, 1959.
- [19] Katsura, H., Nagaosa, N., and Balatsky, A. V., “Spin Current and Magnetoelectric Effect in Noncollinear Magnets”, *Phys. Rev. Lett.*, 95, 057205, 2005.
- [20] Mostovoy, M., “Ferroelectricity in Spiral Magnets”, *Phys. Rev. Lett.* 96, 067601 (2006)
- [21] Kiselev, S. V., Ozerov, R. P., Zhdanov and G. S., “Detection of magnetic order in ferroelectric  $\text{BiFeO}_3$  by neutron diffraction”, *Soviet Physics - Doklady*, 7(8), 742, 1963.
- [22] Spaldin, N. A., Cheong, S. W. and Ramesh, R., “Multiferroics: Past, present, and future”, *Phys. Today*, 63(10), 38, 2010.
- [23] Chu, Y. H., Martin, Lane W., Holcomb, M. B., Ramesh, R., “Controlling mag-

## Chapter 2: Theoretical background

---

- netism with multiferroics”, *Mater. Today*, 10(10), 16, 2007.
- [24] Seidel, J., Martin, L. W., He, Q., Zhan, Q., Chu, Y. H., Rother, A., Hawkrigde, M. E., Maksymovych, P., Yu, P., Gajek, M., Balke, N., Kalinin, S. V., Gemming, S., Wang, F., Catalan, G., Scott, J. F., Spaldin, N. A., Orenstein, J., and Ramesh, R., “Conduction at domain walls in oxide multiferroics”, *Nat. Mater.*, 8(3), 229, 2009.
- [25] Wenk, H. R., Bulakh, A., “Minerals: Their Constitution and Origin”, New York, NY: Cambridge University Press. ISBN 978-0-521-52958-7, 2004.
- [26] Navrotsky, A.,(1998).“Energetics and Crystal Chemical Systematics among Ilmenite, Lithium Niobate, and Perovskite Structures”, *Chem. Mater.*, 10(10), 2787, 1998.
- [27] Cullity, B. D., “Introduction to Magnetic Materials”, Addison-Wisley Publishing Company, Inc., California, 1972.
- [28] Warburg, E., “Magnetische untersuchungen”, *Ann. Phys. Chem.*, 13, 141, 1881.
- [29] Ewing, A., “Magnetic Induction in Iron and other Metals”, *Proc. Roy. Soc.*, 220, 39, 1882.
- [30] Chen, C. W. “Magnetism and Metallurgy of Soft Magnetic Materials”, North Holland Publishing Company, Amsterdam, 1977.
- [31] Jiles, D. C., Garikepati, P. and Chang, T. T., “Theory of ferromagnetic hysteresis: evaluation of stress from hysteresis curves”, *IEEE Trans. Mag.*, 24, 2922, 1988.
- [32] Wang, J., Neaton, J. B., Zheng, H., Nagarajan, V., Ogale, S. B., Liu, B., Viehland, D., Vaithyanathan, V., Schlom, D. G., Waghmare, U. V., Spaldin, N. A., Rabe, K. M., Wuttig, M. and Ramesh, R., “Epitaxial BiFeO<sub>3</sub> multiferroic thin film heterostructures”, *Science*, 299, p. 1719, 2003.
- [33] Carter, C. B., Norton, M. G., “Ceramic Materials Science and Engineering”, Springer, New York, 2007.

## Chapter 2: Theoretical background

---

- [34] Neaton J. B., Ederer C., Waghmare U.V., Spaldin N.A., Rabe K. M., "First-principles study of spontaneous polarization in multiferroic BiFeO<sub>3</sub>", Phys. Rev. B, vol. 71, pp. 014113, 2005.
- [35] Seshadri R., Hill N. A., "Visualizing the role of Bi 6s „lone pairs“ in the off-center distortion in ferromagnetic BiMnO<sub>3</sub>", Chem. Mater., vol. 13, pp. 2892, 2001.
- [36] Iniguez, J., Bellaiche, L., Vanderbilt, D., "First-principles study of (BiScO<sub>3</sub>)<sub>1-x</sub>(PbTiO<sub>3</sub>)<sub>x</sub> piezoelectric alloys", Phys. Rev. B, vol. 67, pp. 224107, 2003.
- [37] Catalan G., Scott J.F., "Physics and Applications of Bismuth Ferrite", Adv. Mater., vol. 21, pp. 2463, 2009.
- [38] Fox, M. A., Dulay, M. T., "Heterogeneous Photocatalysis", Chem. Rev., 93, 341, 1993.
- [39] Russell, A. D., "Bacterial adaptation and resistance to antiseptics, disinfectants and preservatives is not a new phenomenon", Journal of Hospital Infection, 57, 97-104, 2004.
- [40] Burda C., Lou Y., Chen, X., Samia, A. C. S., Stout, J., and Gole, J. L. "Enhanced Nitrogen Doping in TiO<sub>2</sub> Nanoparticles", J. Phys. Sci., 3, 1049, 2003.
- [41] Subramanian, V., Pangarkar, V. G., and Beenackers, A. A. C. M., "Photocatalytic degradation of para-hydroxybenzoic acid: Relationship between substrate adsorption and photocatalytic degradation", Clean Products and Processes, vol. 2, pp. 149, 2000.
- [42] Noguchi, T., Fujishima, A., Sawunoyama, P., and Hashimoto, K., "Photocatalytic degradation of gaseous formaldehyde using TiO<sub>2</sub> film", Environ. Sci. and Tech., vol. 32, no. 23, 3831, 1998.
- [43] Yawalkar, A. A., Bhatkhande, D. S., Pangarkar, V. G. and Beenackers, A. A. C. M. "Solar-assisted photochemical and photocatalytic degradation of phenol", J. of Chem. Technol. and Biotechnol., vol. 76, pp. 363, 2001.
- [44] Yang, L., and Liu, Z. "Study on light intensity in the process of photocatalytic

- degradation of indoor gaseous formaldehyde for saving energy”, *Energy Conversion and Management*, vol. 48, pp. 882-889, 2007.
- [45] Soltani, T., Entezari, M. H., “Sono-synthesis of bismuth ferrite nanoparticles with high photocatalytic activity in degradation of Rhodamine B under solar light irradiation”, *Chem. Eng. J.*, 223, 145, 2013.
- [46] Tanaka, S. and Saha, U. K., “Effects of pH on photocatalysis of 2,4,6-trichlorophenol in aqueous TiO<sub>2</sub> suspensions”, *Water Sci. Technol.*, vol. 30, no. 9, pp. 47, 1994.
- [47] Ku, Y., Leu, R., and K. Lee, K., “Decomposition of 2-chlorophenol in aqueous solution by UV irradiation with the presence of titanium dioxide”, *Water Res.*, vol. 30, no. 11, 1996, pp. 2569-2578.
- [48] Zhang, X., Liu, H., Zheng, B., Lin, Y., Liu, D., and Nan, C. W. “Photocatalytic and Magnetic behaviors observed in BiFeO<sub>3</sub> nanofibers by electrospinning”, *Journal of nanomaterials*, 2013, 3, 2013.
- [49] Yu, J., Zhao, X., and Zhao, Q., “Effect of surface structure on photocatalytic activity of TiO<sub>2</sub> thin films prepared by sol-gel method”, *Thin Solid Films*, vol.379,, pp. 7, 2000.
- [50] Caldwell, M. M., “Plant Life and Ultraviolet Radiation: Some Perspective in the History of the Earth’s UV Climate”, *Bio Science*, vol.29, no. 9, pp. 520, 1979.
- [51] Sasaki, M., Takeshita, S., Sugiura, M., Sudo, N., Miyake, Y., Furusawa, v., and Sakata, T., “Ground-based observation of biologically active solar ultraviolet-B irradiance at 35 degrees N latitude in Japan”, *J. Geomagn. Geoelectr. (Japan)*, vol. 45, pp. 473-85, 1993.
- [52] Stroyuk, A. L., Kryukov, A. I., Kuchmii, S. Ya., and Pokhodenko, V. D. “Quantum size effects in semiconductor photocatalysis”, *Theoretical and Experimental Chemistry*, vol. 41, no. 4, pp. 207-228, 2005.

## Chapter 2: Theoretical background

---

- [53] Guo, R., Fang, L., Dong, W., Zheng, F. and Shen, M., “Enhanced photocatalytic activity and ferromagnetism in Gd doped BiFeO<sub>3</sub> nanoparticles”, *J. Phys. Chem. C*, 114, 21390-21396, 2010.
- [54] Stroyuk, A. L., Kryukov, A. I., Kuchmii, S. Ya. and Pokhodenko, V. D., “Quantum size effects in the photonics of semiconductor nanoparticles”, *Theor. Exp. Chem.*, vol. 41, no. 2, pp. 67, 2005.
- [55] Schiavello, M., “Heterogeneous photocatalysis”, John Wiley and Sons, 1997.
- [56] Gao, F., Chen, X., Yin, K., Dong, S., Ren, Z., Yuan, F., Yu, T., Zou, Z. and Liu, J.-M., “Visible Light Photocatalytic Properties of Weak Magnetic BiFeO<sub>3</sub> Nanoparticles”, *Adv. Mater.*, 19, 2889, 2007.
- [57] Zhang, Y., Schultz, A. M., Salvador, P. A. and Rohrer, G. S., “Spatially selective visible light photocatalytic activity of TiO<sub>2</sub>/BiFeO<sub>3</sub> heterostructures”, *J. Mater. Chem.*, 21, 4168, 2011.

# Chapter 3

## Sample Preparations and Experimental Techniques

### 3.1 Introduction

In this chapter, sample preparations and experimental characterization techniques for studying magnetic properties, electrical properties and photocatalytic activity of the fabricated materials are reviewed. A number of techniques can be employed to obtain a profound understanding of the physics behind multifunctional materials. Different methods starting from X-ray diffraction, via Vibrating sample magnetometer (VSM) to optical spectroscopy are described.

### 3.2 Synthesis of bulk polycrystalline sample

All experimental studies on functional materials depend on high-quality samples and therefore preparation of good quality samples is the prerequisite to determine their properties. There exist a plenty of techniques for the synthesis of bulk polycrystalline solid materials. Out of them, the solid-state reaction technique is extensively used for the fabrication of bulk polycrystalline solids as it is simple and cost effective. In this present investigation, bulk polycrystalline samples were prepared initially by using solid state reaction technique.

#### 3.2.1 Solid state reaction technique

In this method reactants are mixed together in powder form and heated for extended periods at high temperature. High temperature provides a considerable amount of energy to accelerate the reaction rate. Hence, the final product obtained from this method is thermodynamically stable. The major benefit of this method is the formation of structurally defined product with desired properties which depends on final sintering temperature. The preparation of bulk polycrystalline samples by using solid state reaction technique is descri-

bed by using the following flow chart (figure 3.1).

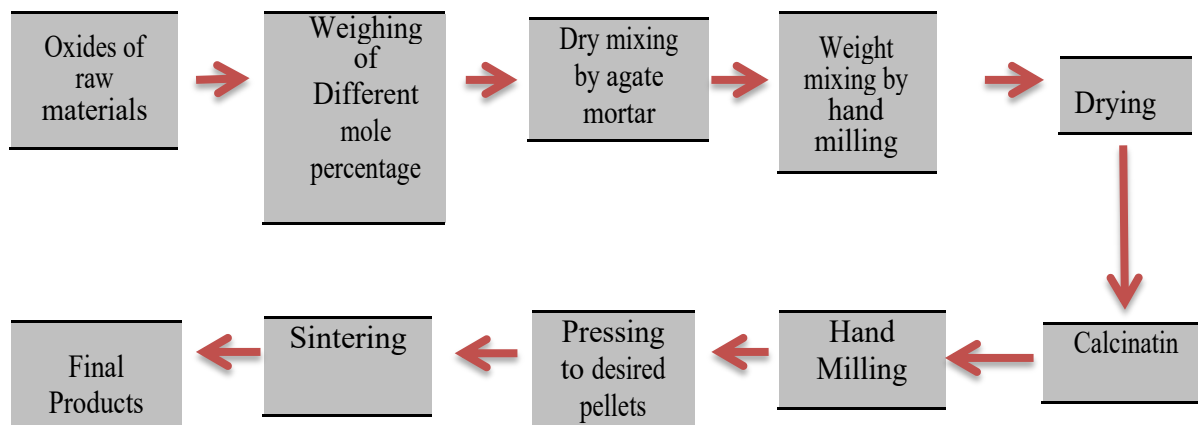


**Figure 3.1:** Flow chart of the preparation of bulk polycrystalline materials by solid-state reaction technique.

Detail process of calcination, pelletization and sintering are given below.

#### 3.2.1.1 Calcination

Calcination is a thermal treatment process in presence of air applied to ores and other solid materials to bring about a thermal decomposition phase transition or removal of a volatile fraction. The calcination processes normally take place below the melting point of the product materials. Calcination is to be distinguished from roasting, in which more complex gas solid reaction take place between the furnace atmospheres of the solid. The calcination reaction usually takes place at or above the thermal decomposition or transition temperature. This temperature is usually defined as the temperature at which the standard Gibbs free energy for a particular calcination reaction is zero [1]. The calcining process can be repeated several times to obtain a high degree of homogeneity. The calcined powders are crushed into fine powders. The ideal characteristics of fine powders are [2]. small particle size (sub-micron) narrow distribution in particle size dispersed particles equiaxed shape of particles high purity homogeneous composition. A small particle size of the reactant powders provides a high contact surface area for initiating the solid state reaction, by proper calcination. Porosity is easily eliminated if the initial pores are very small. A narrow size distribution of spherical particles as well as a dispersed state is important for compaction

of the powder during green-body formation. Grain growth during sintering can be better controlled if the initial size is small and uniform.

#### 3.2.1.2 Pelletization

It is a process of pressing the powder in automatic hydraulic press at room temperature by applying a force of around 2-10 tons for couple of seconds to accelerate the reaction rate. Here it is essential to increase the area of contact between the particles, this can be achieved by pressing the reaction powder into pellets but even at high pressure the pellets are sometimes porous and the crystal contacts are not perfect. Therefore, pelletization of the samples with a proper pressure is another important requirement to obtain good quality samples [3].

#### 3.2.1.3 Sintering

Sintering is defined as the process of obtaining a dense, solid body by heating a compacted powder for a certain time at a temperature high enough to significantly promote diffusion, but clearly lower than the melting point of the main component. The driving force for sintering is the reduction in surface free energy of the powder. Part of this energy is transferred into interfacial energy (grain boundaries) in the resulting polycrystalline body [2,4] The sintering time, temperature and the furnace atmosphere play very important role to determine the electric and magnetic properties of multiferroic and related materials. The purposes of sintering process are:

- ❖ to bind the particles together so as to impart sufficient strength to the product
- ❖ to densify the material by eliminating the pores and
- ❖ to homogenize the materials by completing the reactions left unfinished in the calcining step.

Sintering of a solid material is divided into three stages as shown in figure 3.2 [25]

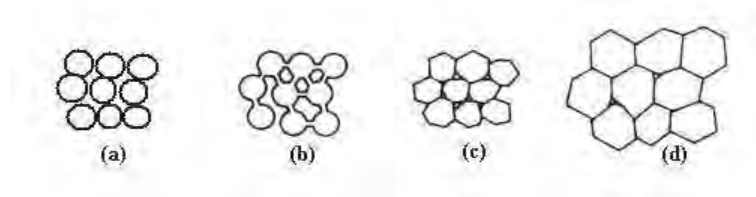


**Figure 3.2:** Schematic representation of sintering stages: (a) green body, (b) initial stage, (c) intermediate stage, and (d) final stage.

- ❖ Stage 1. Contact area between particles increases,
- ❖ Stage 2. Porosity changes from open to closed porosity,
- ❖ Stage 3. Pore volume decreases; grains grow.

#### **3.2.2 Preparation of $\text{Bi}_{0.9}\text{Y}_{0.1}\text{FeO}_3$ bulk materials**

In this present investigation, Polycrystalline sample of  $\text{Bi}_{0.9}\text{Y}_{0.1}\text{FeO}_3$  were synthesized by standard solid state reaction technique described above. The high purity oxides of  $\text{Bi}_2\text{O}_3$ ,  $\text{Fe}_2\text{O}_3$  and  $\text{Y}_2\text{O}_3$  powders were mixed and ground in an agate mortar till a homogeneous mixture is formed. This mixture was calcined at around  $650^\circ\text{C}$  for 2 hours in a programmable furnace. The calcined powders were ground again for 2 hours to get more homogeneous mixture. The mixture was calcined again at around  $700^\circ\text{C}$  for 2 hours in the same programmable furnace. The calcined powders were ground again for 60 minutes to get more homogeneous mixture. The powders were pressed into pellets of thickness 1 mm and diameter 13 mm by using a automatic hydraulic press and were sintered at around  $750^\circ\text{C}$  for 5 hours [6]. The ceramic pellets were ground again into powder by manual grinding to obtain powder materials. The sintered pellets and powders were used to measure the required structural, morphological, ferroelectric, optical and magnetic properties.

### **3.3 Fabrication of Nanoparticles**

A wide variety of techniques exist for the synthesis of nanoparticles in the research community. Nanoparticles can be derived by “Top-down”, or synthesized by “bottom-up” methods. A Top-down technique refers to “ultrasonication technique” [12] and sol-gel [28] are getting very popular at the present days to the scientists due it’s capability of creating ultrafine nanoparticles.

#### **3.3.1. Ultrasonication Technique**

In ultrasonication technique, the ultrasonic wave energy is used to synthesis nanoparticles that disperse the agglomerated materials into single particle. Details mechanism of the

### 3: Sample Preparations and Experimental Techniques

---

ultrasonication technique is given below. This brief overview highlights the basic aspects of ultrasonic generation and propagation relevant to particle dispersion [8]. During the process of ultrasonic disruption, sound waves propagate through the liquid medium in alternating high and low pressure cycles at frequencies typically in the 20-40 kHz range. During the low-pressure cycle (rarefaction), microscopic vapor bubbles are formed in a process known as cavitation (Figure 3.3). The bubbles then collapse during the high pressure cycle (compression) producing a localized shock wave that releases tremendous mechanical and thermal energy.

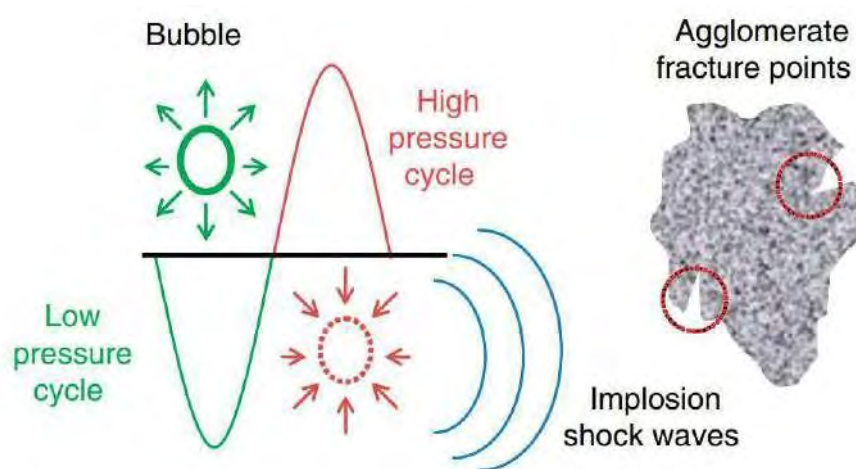


**Figure 3.3:** Schematic illustration of ultrasonic wave-induced cavitation and agglomerate fracture [8].

Ultrasonic waves can be generated in a liquid suspension either by immersing an ultrasound probe (transducer horn) into the suspension (direct sonication), or by introducing the sample container into a liquid that is propagating ultrasonic waves (indirect sonication). This is shown schematically in figure 3.4. In a sonication bath or a so-called cup horn sonicator (indirect sonication), the sound waves must travel through both the bath or cup liquid (typically water) and the wall of the sample container before reaching the suspension. In direct sonication, the probe is in contact with the suspension, reducing the physical barriers to wave propagation and therefore delivering a higher effective energy output into the suspension. Bath sonicators typically operate at much lower energy levels than are attainable using a probe or cup horn. In the case of bath sonicators, the transducer element is directly attached to the outside surface of the metal tank, and the ultrasonic waves are transmitted directly to the tank surface and then into

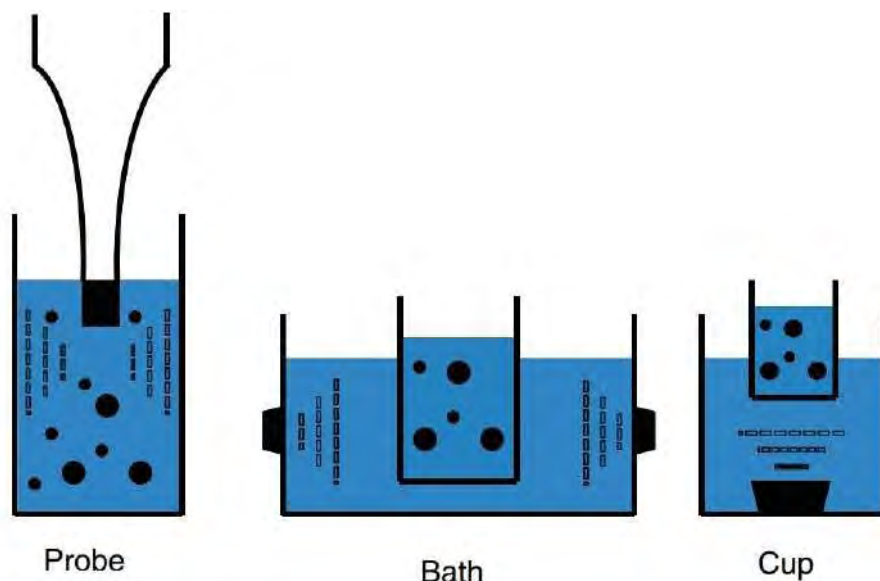


**Figure 3.4:** Schematic illustration of direct (left) and indirect (middle and right) sonication configurations as described in the text.

the bath liquid. In a cup horn, the radiating surface of the horn is inverted and sealed into the bottom of a (typically) transparent plastic cup into which the sample container is immersed. At ultrasound frequencies, the alternating formation, growth and subsequent shock waves produced by the collapse of bubbles result in extremely large (localized temperatures up to 10000 K, rapid temperature changes ( $> 10^5 \text{ Ks}^{-1}$ ), pressure bursts on the order of several MPa, and liquid jet streams with speeds reaching  $400 \text{ kmh}^{-1}$ .) Such massive, local energy output is the basis of the disruptive effect of sonication. It must be noted that these considerable pressure and temperature differentials are a result of the cavitation process and occur at the local interface of the exploding bubbles; consequently, these effects are inherent to the sonication process and will occur whether the sonicated container is cooled or not, or the treatment performed using a bath, cup horn, or a probe sonicator.

In all cases, the ultrasonic device transforms electrical power into vibrational energy by means of a piezoelectric transducer that changes its dimensions in response to an applied AC electric field. A sonicator's stated maximum power (e.g., 600 W) refers to the maximum theoretical power it would be able to consume, should it require so; it does not reflect the actual amount of ultrasonic energy delivered to the suspension. That is, for the same frequency and amplitude (and thus the same sonicator setting), the sonicator would need to

### **3: Sample Preparations and Experimental Techniques**

---

consume more power to treat a high viscosity suspension than it would for a low viscosity suspension, and if so, it could consume up to a maximum of 600 W. It is therefore erroneous to assume that selecting the highest setting value will result in the delivery of the instruments nominal maximum power to the sonicated suspension. For low viscosity media, even at the highest setting value, the delivered power will be a significantly lower fraction of the instruments maximum power rating. Similarly, the power value (measured in W) usually shown on the instrument display reflects the power that the instrument is consuming from the electrical source to produce the desired oscillation amplitude (from the selected setting value) in the sonicated medium. The consumed (i.e., displayed) power, however, does not necessarily reflect the power that is actually delivered to the sonicated suspension. Here in lies the deficiency with reporting either the manufacturers stated maximum power, the adjustable output power reading provided by the instrument, or the chosen setting level.

The net fragmentation effect from applying ultrasonic energy to a suspension is dependent on the total amount of energy delivered to the sonicated medium. However, not all of the produced cavitation energy is effectively utilized in disrupting particle clusters. The delivered energy is consumed or dissipated by several mechanisms, including thermal losses, ultrasonic degassing, and chemical reactions, such as the formation of radical species. Only a portion of the delivered energy is actually used in breaking particle-particle bonds to produce smaller particle aggregates, agglomerates, and primary particles. Moreover, an excessive energy input can potentially result in agglomerate formation or re agglomeration of previously fragmented clusters, as well as induce a variety of physicochemical alterations on the materials surface or to the constituents of the suspending medium. Such sonication-specific side-effects are addressed in the following sections, but first we examine the particle disruption process as it is the primary objective of ultrasonic treatment.

#### **3.3.2 Sonication effects on particle disruption and aggregation**

The properties of synthesized nanoparticles are strongly dependent on the particle size of the processed material. For instance, the size of the particles in suspension dictates along with the particles surface chemistry, their photocatalytic activity and arsenic from water. Additionally, the agglomeration state determines whether the particles will settle out

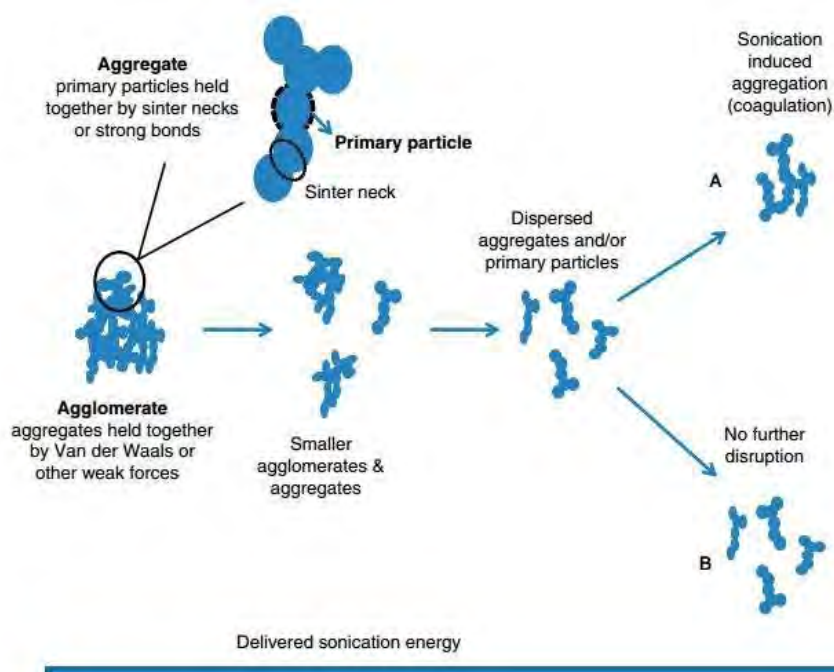


**Figure 3.5:** Schematic depiction of particle structures referred to in the text, and illustration of the typical effects of sonication on particle size as a function of delivered sonication energy [8].

or remain in suspension, which directly impacts in magnetization, polarization and leakage current [9]. Numerous other examples of size-dependent behavior can be found in the recent literature. Dry powders consist of particles that are bound together into macroscopic structures by both weak physical Vander Waals forces and stronger chemical bonds including particle fusion. Commonly, these powders contain micro meter and sub micro meter scale aggregates, which are in turn held together by physical forces to constitute larger agglomerates. This is depicted schematically in figure 3.5. For powders consisting of nano scale particles and aggregates, and therefore having substantial interfacial contact areas per unit volume, the nominally weaker Vander Waals forces can be extremely large, requiring the use of techniques such as sonication to effectively break down or disrupt powder agglomerates. In contrast, micro meter size primary particles can often be dispersed with moderate mixing or stirring.

#### 3.3.3 Why Sonication Technique

The properties of synthesized nanoparticles depend on the fabrication process. It is reported that, the magnetic order in the surface of the particles is modified by forming a magnetic dead layer [13–16], and consequently affect the magnetization, transition temperature and anisotropy of the material system [13]. By using the available wet chemical methods, it is diff-

### 3: Sample Preparations and Experimental Techniques

icult to control the complex solution processes and the size of the synthesized nanoparticles [17]. Therefore, the synthesis of nanoparticles with controlled size, chemical composition, oxygen stoichiometry and unmodified surface is of fundamental and technological interest. Notably, the perovskite nanoparticles of various compositions have been synthesized using the ball milling technique [18–22] to produce nanoparticles from a few to tens nanometers [18]. However, the magnetic properties of the finer particles were found to degrade. The degradation was ascribed to the increase of the defects density and surface roughness of the nanoparticles due to the high energy ball milling [18]. During the fabrication of the nanoparticles using ball milling, for a milling time longer than 40 h, the perovskite structure disappeared and a completely amorphous phase was formed [20]. Moreover, the magnetic measurements showed that ball milled samples have an inhomogeneous magnetic state [20].

Recently, our group synthesized Bi based  $\text{Bi}_{0.9}\text{Gd}_{0.1}\text{Fe}_{1-x}\text{Ti}_x\text{O}_3$  and  $\text{Bi}_{0.7}\text{Ba}_{0.3}\text{Fe}_{1-x}\text{Ti}_x\text{O}_3$  nanoparticles by ultrasonication of their micrometer sized multiferroic bulk powder materials [12,23]. Transmission electron microscopy imaging confirmed the formation of single crystalline nanoparticles with a mean size of 11-13 nm for 60 minutes sonication. In this present investigation, we have used this technique to produce ultrafine nanoparticles of Y doped  $\text{BiFeO}_3$  solid materials. A bath sonicator of 500 W was used in Nanotechnology Research Laboratory (NRL) in BUET to fabricate nanoparticles as shown in figure 3.7.



**Figure 3.6:** A bath sonicator of 500 W, (BUET NRL), (Model: POWERSONIC 510 HWASHIN technology Co.).

#### **3.3.4 Preparation of $\text{Bi}_{0.9}\text{Y}_{0.1}\text{FeO}_3$ nanoparticles by Ultrasonication**

Ceramic pellets of multiferroics with the nominal compositions of  $\text{Bi}_{0.9}\text{Y}_{0.1}\text{FeO}_3$  were prepared by a conventional solid state reaction technique. Details of the synthesis mechanism were described in section 3.3. The pellets were then ground into powder by performing manual grinding for approximately 60 minutes. The obtained powders were subsequently mixed with isopropanol with a ratio of 50 mg powder and 10 ml isopropanol with a mass percentage of  $\sim 0.5$  percent. Then, the mixtures of isopropanol and powder were put into an ultrasonic bath and sonicated for 60 minutes. After 12 hours,  $\sim 78$  percent of the mass had precipitated and the supernatant was collected from the solution to obtain nanoparticles. The supernatant was dried naturally and the collected nanoparticles were used to measure the required properties. Details of the sonication mechanism were described in the earlier section.

#### **3.4 Sol-gel Method**

The sol-gel process may be described as:

“Formation of an oxide network through polycondensation reactions of a molecular precursor in a liquid”.

A **sol** is a stable dispersion of colloidal particles or polymers in a solvent. The particles may be amorphous or crystalline. An aerosol is particles in a gas phase, while a sol is particles in a liquid.

A **gel** consists of a three dimensional continuous network, which encloses a liquid phase, in a colloidal gel, the network is built from agglomeration of colloidal particles. In a polymer gel the particles have a polymeric sub-structure made by aggregates of sub-colloidal particles. Generally, the sol particles may interact by van der Waals forces or hydrogen bonds. A gel may also be formed from linking polymer chains. In most gel systems used for materials synthesis, the interactions are of a covalent nature and the gel process is irreversible. The gelation process may be reversible if other interactions are involved.

##### **3.4.1 Why Sol-gel Method**

Advantages of sol-gel synthesis as the prime method for the production of  $\text{BiFeO}_3$  are:

### 3: Sample Preparations and Experimental Techniques

---

- ❖ Multi component compounds may be prepared with a controlled stoichiometry mixing sols of different compounds.
- ❖ The sol-gel method prevents the problems with co-precipitation, which inhomogeneous be a gelation reaction.
- ❖ Self-purification due to the high exothermic temperatures involvement.
- ❖ Synthesis of single phase materials at very low temperatures.
- ❖ Simple and cost effective.
- ❖ Enables mixing at an atomic level.
- ❖ Formation of nanopowder in the desired size and shape with uniform particle size distribution.

#### 3.4.2 Preparation of BiFeO<sub>3</sub> Nanoparticles by Sol-gel Method

- ❖ Stoichiometric proportion of Bi(NO<sub>3</sub>)<sub>3</sub>.5H<sub>2</sub>O and Fe(NO<sub>3</sub>)<sub>3</sub>.9H<sub>2</sub>O were initially dissolved in 400 ml deionized water with an individual concentration of 0.025M.
- ❖ The solution was stirred for about half an hour to obtain a clear solution.
- ❖ When the solution was transparent, 0.02 mole of C<sub>6</sub>H<sub>8</sub>O<sub>7</sub> as the chelating agent was added to the solution to complex the metal cations (Figure 3.7a).
- ❖ The solution was then stirred and heated at 70-75 °C for 8-10 hours to form a transparent blackish-red sol (Figure 3.7b).
- ❖ Afterwards appropriate amount of ethylene glycol was added to the solution as polymerization agent.
- ❖ The resultant solution was heated at 70-75 °C to initiate the polymerization reaction and a few minutes later a gel was formed with vigorous boiling and fuming (Figure 3.7c).

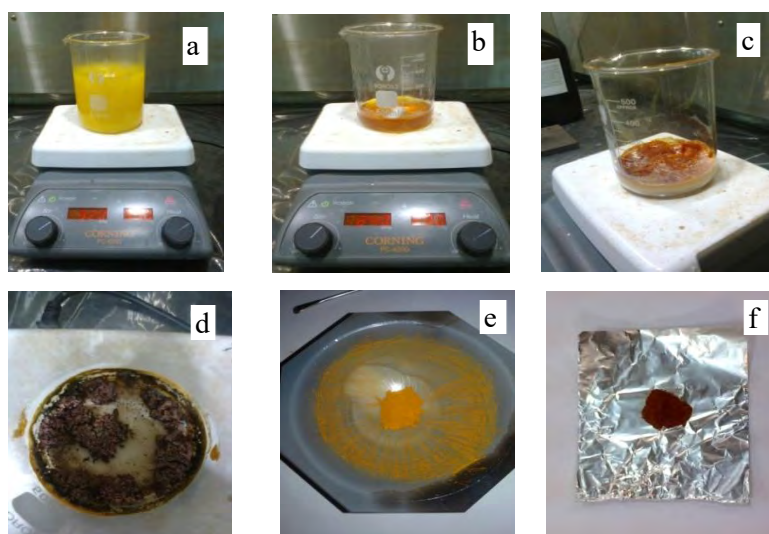


**Figure 3.7:** Synthesis steps a) mixing raw materials into deionized water, b) formation of sol, c) formation of gel, d) precursor xerogel, e) ground xerogel, f) annealed BiFeO<sub>3</sub> powder.

### 3: Sample Preparations and Experimental Techniques

---

- ❖ The gel was dried at 100 °C for 24 hours in a functional oven to obtain fluffy green xerogel (Figure 3.7d).
- ❖ The xerogel samples were then grounded into powder and annealed at 600 °C (the heating and cooling rate were maintained at 3 °C /min.) for 2 hours using a functional furnace in static air (Figure 3.7e).
- ❖ Finally the powders were grounded to get BiFeO<sub>3</sub> nanoparticles (Figure 3.7f)

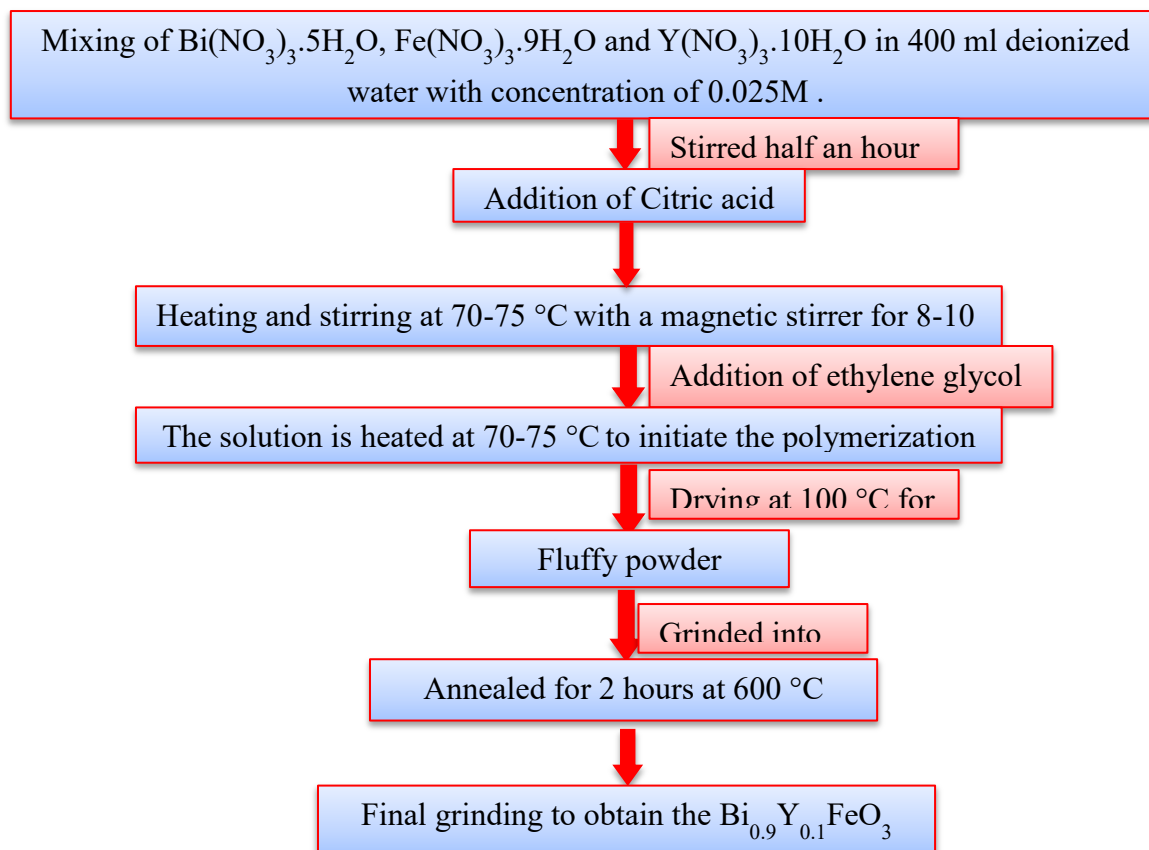
#### 3.4.3 Synthesis of Bi<sub>0.9</sub>Y<sub>0.1</sub>FeO<sub>3</sub> nanoparticles by Sol-gel

The synthesis process of the Y doped BFO powders was quite similar to the synthesis of pure BFO powder, except that there is an addition of rare earth metal (Y) into the Bi-Fe ionic solution before the heating process.

Materials for synthesis Bi<sub>0.9</sub>Y<sub>0.1</sub>FeO<sub>3</sub> nanoparticles by Sol-gel method:

- Bi(NO<sub>3</sub>)<sub>3</sub> .5H<sub>2</sub>O
- Fe(NO<sub>3</sub>)<sub>3</sub>.9H<sub>2</sub>O
- Y(NO<sub>3</sub>)<sub>3</sub>.10H<sub>2</sub>O
- C<sub>6</sub>H<sub>8</sub>O<sub>7</sub>
- OHCH<sub>2</sub>CH<sub>2</sub>OH
- Deionized water

#### Flow Chart of Synthesis Procedure:



#### 3.4.4 Annealing

Annealing, in metallurgy and materials science, is a heat treatment that alters the physical and sometimes chemical properties of a material to increase its ductility and reduce its hardness, making it more workable. It involves heating a material to about its recrystallization temperature, maintaining a suitable temperature, and then cooling. During annealing, atoms migrate in the crystal lattice and the number of dislocations decreases, leading to the change in ductility and hardness.

Laboratory Chamber Furnace (CAEBOLITE, ELF 11/6B / Germany) (NRL, BUET) was used to anneal xerogel samples at 600 °C in air atmosphere. The basic annealing cycle in our experiment is shown in figure 3.8.



Figure 3.8: Furnace used for annealing xerogel sample into NRL (BUET)

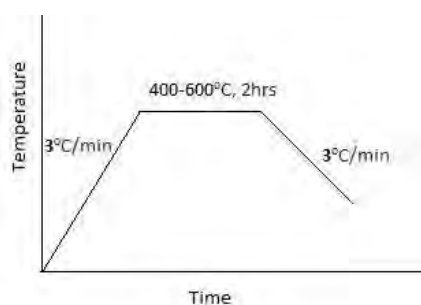


Figure 3.9: Annealing cycle

### 3.5 Structural characterization techniques

#### 3.5.1 X-ray diffraction

X-ray diffraction is the most fundamental and commonly used method to determine the

### 3: Sample Preparations and Experimental Techniques

structural and phase properties of crystalline samples. The basic principle of X-ray powder diffraction is illustrated in figure 3.10. The diffraction patterns can be analyzed in terms of Bragg's law:

$$2d\sin\theta = n\lambda \quad (3.1)$$

This law relates the wavelength ( $\lambda$ ) of electromagnetic radiation to the diffraction angle ( $\theta$ ) and the lattice spacing ( $d_{hkl}$ ) between two crystal plane in a crystalline sample. These diffracted X-rays are then detected, processed and counted. By scanning the sample through a range of  $2\theta$  angles, all possible diffraction directions of the lattice should be attained due to the random orientation of the powdered material. The phase analysis and crystal structure characterizations of the samples in this thesis were mostly performed using X-ray powder diffraction (XRD) with a Bruker D8 diffractometer equipped with a Vantec position sensitive detector (PSD, 4 degree opening) using Cu K $\alpha$  radiation,  $\lambda = 1.540598 \text{ \AA}$ .

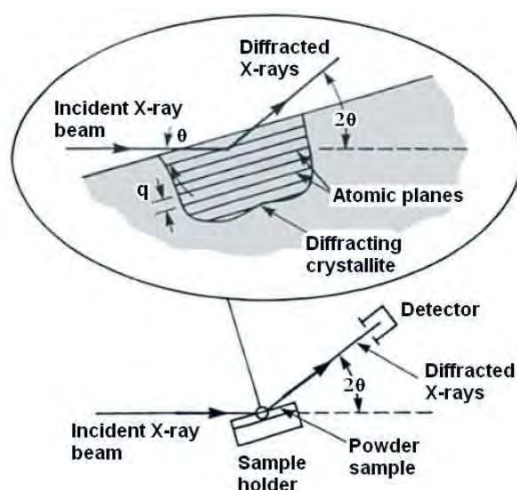


**Figure 3.10:** Schematic diagram for a X-ray powder diffraction (XRD) experiment. Adapted from BRUNDLE ET AL. [26].

The intensity of diffracted X-rays is continuously recorded as the sample and detector rotate through their respective angles. A peak in intensity occurs when the mineral contains lattice planes with  $d_{hkl}$ -spacings appropriate to diffract X-rays at that value of  $\theta$ . Once all  $d_{hkl}$ -spacings have been determined they are compared with standard data, available from the International Centre for Diffraction Data as the Powder Diffraction File (PDF), which facilitates to identify any impurity phases appeared as extra peaks.

## 3.6 Morphological Studies

### 3.6.1 Field Effect Scanning Electron Microscope (FESEM)

FESEM is a type of electron microscope that creates various images (surface morphology) by focusing a high energy beam of electrons onto the surface of a sample and detecting signals from the interaction of the incident electron with the sample's surface. The type of signals gathered in a FESEM varies and can include secondary electrons, characteristic x-rays, and back scattered electrons. In a FESEM, these signals come not only



**Figure 3.11:** Photograph of Field Effect Scanning Electron Microscope (FESEM).

from the primary beam impinging upon the sample, but from other interactions within the sample near the surface. The FESEM is capable of producing high resolution images of a sample surface in its primary use mode, secondary electron imaging. Due to the manner in which this image is created, FESEM images have great depth of field yielding a characteristic three-dimensional appearance useful for understanding the surface structure of a sample. This great depth of field and the wide range of magnifications are

the most familiar imaging mode for specimens in the FESEM. Characteristic x-rays are emitted when the primary beam causes the ejection of inner shell electrons from the sample and are used to tell the elemental composition of the sample. The back-scattered electrons emitted from the sample may be used alone to form an image or in conjunction with the characteristic x-rays as atomic number contrast clues to the elemental composition of the sample. The microstructure of the surface of the sintered pellets and their corresponding nanoparticles was observed using a field effect scanning electron microscope (FESEM, JEOL, JSM 7600f) in Glass and Ceramics Engineering Department, BUET as shown in figure 3.11.

#### **3.6.2 Scanning process and image formation**

In a typical FESEM, an electron beam is emitted from an field emission gun. The electron beam, which typically has an energy ranging from a few 100 eV to 40 keV, is focused by one or two condenser lenses to a spot about 0.4 nm to 5 nm in diameter. The beam passes through pairs of scanning coils or pairs of deflector plates in the electron column, typically in the final lens, which deflect the beam in the x and y axes so that it scans in a raster fashion over a rectangular area of the sample surface.

When the primary electron beam interacts with the sample, the electrons lose energy by repeated random scattering and absorption within a teardrop-shaped volume of the specimen known as the interaction volume, which extends from less than 100 nm to around 5 m into the surface. The size of the interaction volume depends on the electron's landing energy, the atomic number of the specimen and the specimen's density. The energy exchange between the electron beam and the sample results in the reflection of high-energy electrons by elastic scattering, emission of secondary electrons by inelastic scattering and the emission of electromagnetic radiation, each of which can be detected by specialized detectors. The beam current absorbed by the specimen can also be detected and used to create images of the distribution of specimen current. Electronic amplifiers of various types are used to amplify the signals which are displayed as variations in brightness on a cathode ray tube. The raster scanning of the CRT display is synchronized with that of the beam on the specimen in the microscope, and the resulting

image is therefore a distribution map of the intensity of the signal being emitted from the scanned area of the specimen. The image may be captured by photography from a high resolution cathode ray tube, but in modern machines is digitally captured and displayed on a computer monitor. Figure 3.12 shows a schematic diagram of Field Emission Scanning Electron Microscope (FESEM).

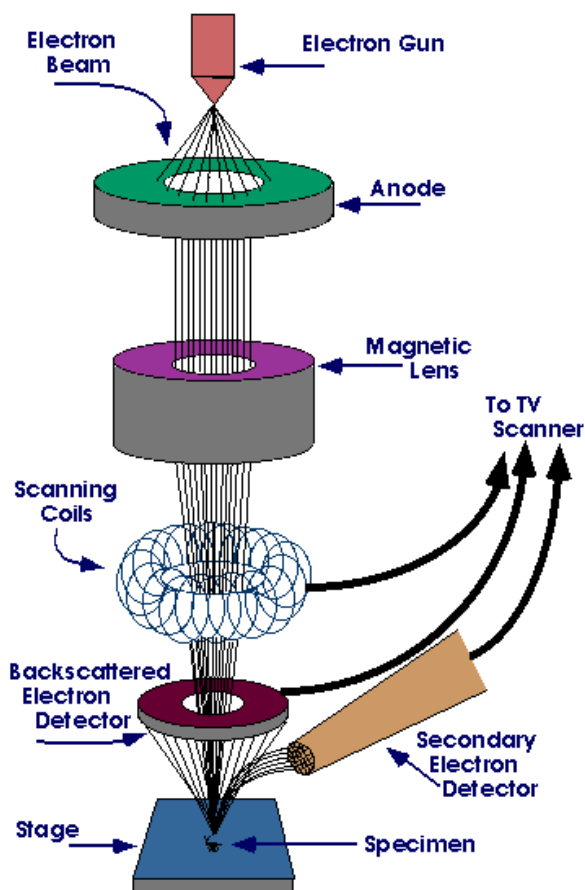


**Figure 3.12:** Schematic diagram of Field Emission Scanning Electron Microscope (FESEM).

## 3.7 Ferroelectric measurement

### 3.7.1 Ferroelectric loop tracer

A ferroelectric compound is characterized a spontaneous polarization below ferroelectric Curie temperature. Experimentally, the ferroelectricity can be confirmed by measuring P-E hysteresis loop. In this investigation, the ferroelectric measurements have been carried out using automatic P-E Loop Tracer Marine India into NRL, BUET.

#### 3.7.1.1 Basic theory of operation

The basic PE test system is based on Sawyer-Tower circuit. The principle is simple when two capacitors are connected in series and AC voltage is applied on both in series, the charge on both will be same. In order to get complete saturation the internal capacitance must be bigger than that of the sample capacitance.

#### 3.7.1.2 Basic calculation

The charge on both capacitances shall be same if both the capacitors are connected in series and an AC voltage is applied. The sample to be measured (device under test) is placed in series with a standard capacitor. As both the capacitor acquires same charge upon applied voltage, the polarization can be calculated using the relation below.

$$Q_1 = Q_2 \quad (3.2)$$

which means

$$C_1 V_1 = C_2 V_2 \quad (3.3)$$

The internal capacitor  $C_2$  is unknown. The total voltage  $V$  applied is also known which are  $V_1 + V_2$ . If we measure voltage across the internal capacitor i.e.  $V_2$  using a data acquisition card we may know how much voltage is applied on the sample by subtracting it from the total voltage. Measurement of  $V_2$  by data acquisition card is easy because magnitude of voltage  $V_2$  will be much less than  $V_1$ . In this way if all three quantities are known we can find  $C_1$  easily using above Eqn (3.3).

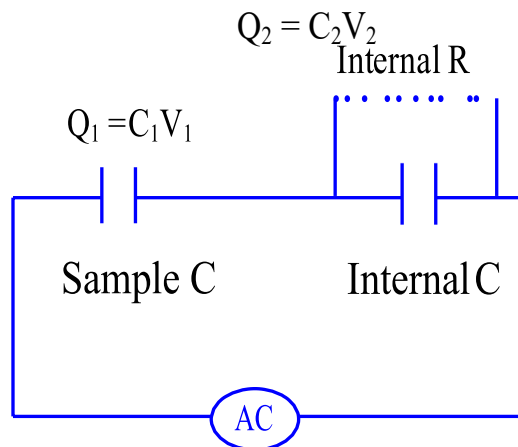


**Figure 3.13:** An schematic diagram of Sawyer tower circuit for P-E loop tracer.

We can get a table of  $Q_1$  if we multiply the sinusoidal voltages  $V_1$  with  $C_1$ . The polarization  $Q_1$  is represented in micro-coulomb per cm square in standard PE graph. This can be calculated simply by mathematical conversation of  $Q_1$  into micro coulomb and dividing by area. The second quantity is  $E$  which is electric field in kV/cm. This also can be achieved by converting the sinusoidal voltages  $V_1$  into kV and then dividing by thickness. If the experiments are conducted in air, the air molecule breaks down at high field resulting a spark between the electrodes. To prevent this, the capacitor is immersed into an oil bath (silicon oil).



**Figure 3.14:** P-E loop tracer system (Marin India).

In this investigation, the P-E loops and leakage current density of the fabricated materials were carried out using the P-E loop tracer system as shown in figure 3.14.

## 3.8 Optical measurement

### 3.8.1 UV-visible diffuse reflectance spectroscopy

The optical phenomenon known as diffuse reflectance is commonly used in the UV- visible, near-infrared (NIR), and mid-infrared regions to obtain molecular spectroscopic information. It is usually used to obtain spectra of powder by the collection and analysis of surface-reflected electromagnetic radiation as a function of frequency. There are two different type of reflection: regular or specular reflection usually associated with reflection from smooth, polished surface like mirrors, and diffuse reflection associated with reflection from so-called mat or dull surface texture like powders.

Originally published in the 1930s by Paul Kubelka and Franz Munk, the Kubelka-Munk equations described the reflectance and transmittance of the sample as a function of the absorption and scatter (K and S, respectively). In this Kubelka-Munk theory, the incident and scattered light flux are approximated by two fluxes I and J, which are perpendicular to the surface of the powdered sample, but in opposite direction as shown in Figure 3.15.

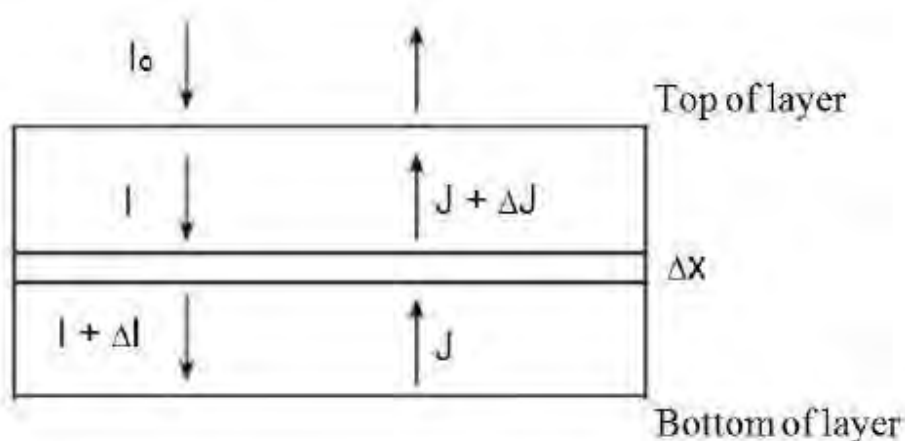


**Figure 3.15:** The Kubelka-Munk approximation: the incident and remitted light fluxes are approximated by two opposite fluxes, perpendicular to the surface of the infinitely thick sample layer.

Ideally one would like a function, like Beer and Lamberts law in transmission spectroscopy, to linearly relate analyte concentration with the reflectance characteristics of a diffusely reflecting sample. The function must use is that derived by Kubelka-Munk:

$$F(R_a) = \frac{(1 - R_a^2)}{2R_a} = \frac{K}{S} = \frac{2.303\epsilon C}{S} \tag{3.4}$$

where K is the absorption coefficient (twice the Beer and Lamberts law absorption coefficient), S is twice the scattering coefficient of the sample, s is the absorptivity, and C is the analyte concentration.

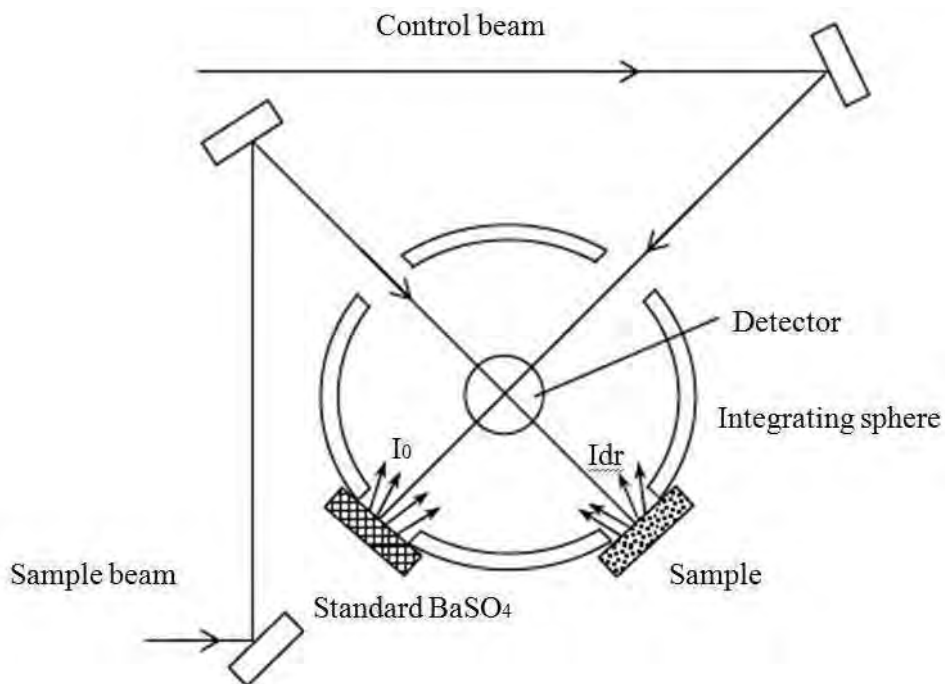


**Figure 3.16:** Solid sample measurement using the integrating spheres method Source: Optional Accessories for Shimadzu UV-Vis spectrophotometers.

The illumination of powdered samples by incident radiation leads to diffuse illumination of the materials. This incident light is then partially absorbed, partially scattered by particles. All UV-vis diffuse reflectance spectrophotometers are classical double beam spectrometers with fully automated acquisition, background subtraction and file storage as shown in Figure 3.16. The light sources are a  $D_2$  lamp for UV irradiation and a Tungsten filament for the visible region, while the reflected light is detected with a photomultiplier in the UV-vis region. Integration sphere is a one of diffuse reflectance attachments. This collects all the light scattered from sample and from a reference standard and the detectors are placed on the top or bottom of the integration sphere. The classical set-up of a diffuse reflectance spectrometer is shown in Figure 3.16. Because the integration sphere must scatter the light and not absorb it, it is coated with a perfectly white material such as  $MgO$ ,  $BaSO_4$ , etc. In this way, a negligibly small amount of specular reflection is included.



**Figure 3.17:** UV-visible spectrometer Shimadzu UV-2600 ISR plus was used into NRL, BUET to take the absorbance and reflectance data.

### 3.8.2 UV-Visible spectrophotometer

Ultraviolet-visible (UV-vis) spectroscopy is used to obtain the absorbance spectra of a molecule or compound in solution or as a solid. When the molecules absorb the suitable light energy or electromagnetic radiation, the electrons in ground state are excited to the excited state levels. The UV-vis region of energy for the electromagnetic spectrum covers 1.5 - 6.2 eV which relates to a wavelength range of 800 - 200 nm. The Beer-Lambert Law is the principle behind absorbance spectroscopy. There are three types of absorbance instruments used to collect UV-vis spectra:

- (1) single beam spectrometer,
- (2) double beam spectrometer and
- (3) simultaneous spectrometer.

In this work, the absorption spectra of dyes solutions were recorded by double beam spectrometer which mainly has a light source (usually a deuterium or tungsten lamp), a sample holder and a detector. For the double beam instrument (Figure 3.18), it has a single source and a monochromator and then there is a splitter and a series of mirrors to get the beam to a reference sample and the sample to be analyzed, this allows for more accurate readings.

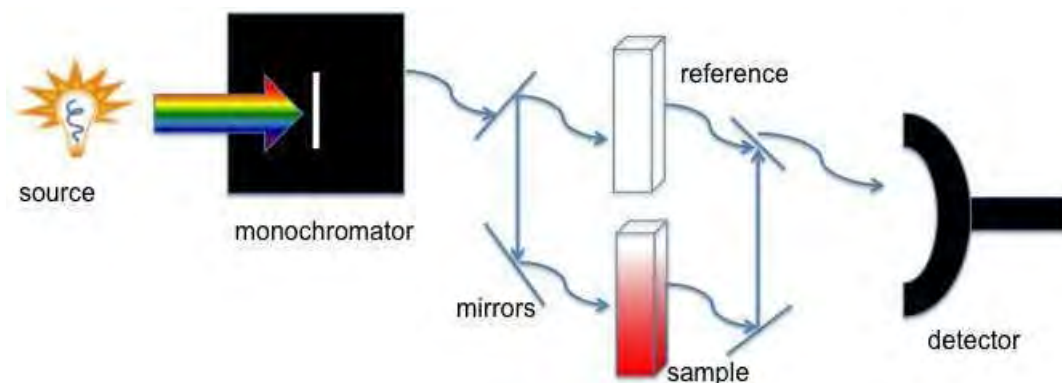


**Figure 3.18:** Illustration of a double beam UV-vis instrument.

The functional relationship between the quantities measured in an absorption method (A) and the quantity sought (the analyte concentration  $c$ ) is known as Beers law and can be written

$$A = \log \frac{P_0}{P} = abc \quad (3.5)$$

where  $a$  is a proportionality constant called the absorptivity and  $b$  is the path length of the radiation through the absorbing medium. Since absorbance is a unit less quantity, the absorptivity has unit that render the right side of the equation dimensionless.

### 3.8.3 Photocatalytic Activity Test

The experimental setup of photocatalytic activity test is shown in figure 3.19. Figure 3.19 (a) and (b) show the closed and open system of the xenon lamp setup, respectively. In this experiment, the xenon lamp of 500 W used as a solar simulator, magnetic stirrer used to make homogeneous solution as shown in figure 3.19 (b). It is very important to keep the intensity of light at a fixed value for each experiment. The flux meter is used to measure the intensity of xenon-lamp-light in this experiment as shown in figure 3.19 (c). The sample solution is centrifuged at  $5000 \text{ rpm}\cdot\text{min}^{-1}$  for 10 minutes to separate the catalyst material from the water using a centrifuge machine as shown in figure 3.19 (d).



**Figure 3.19:** Experimental setup of photocatalytic activity experiment. (a) closed system of Xenon lamp setup, (b) open syestem of xenon lamp setup, (c) Lux meter used to measure lamp-light intensity and (d) centrifuge machine used to separate the RhB solution and photocatalyst.

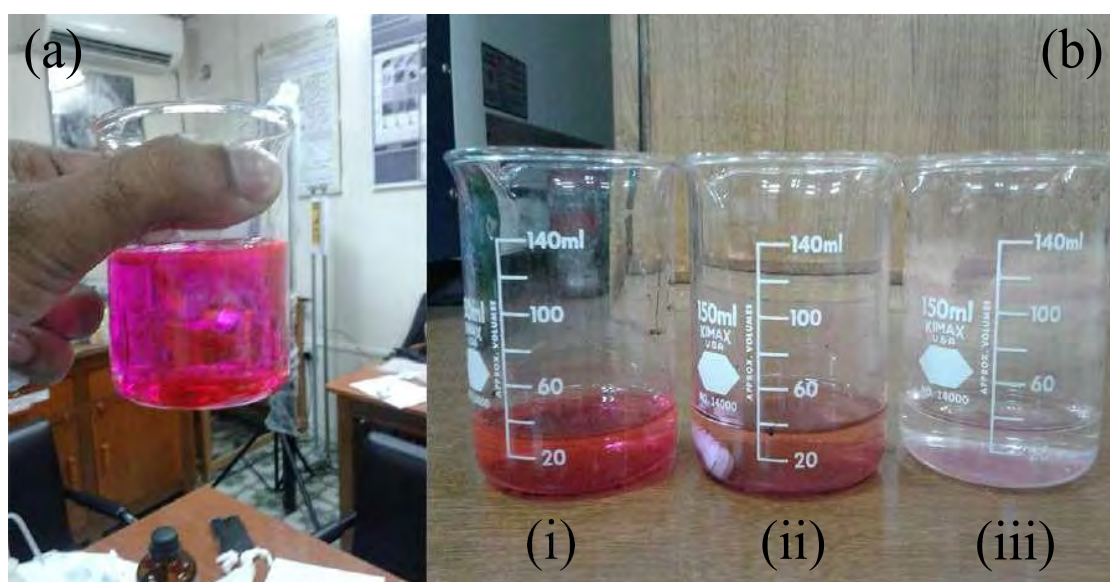


**Figure 3.20:** Degradation of rhodamine mine B. (a) color of RhB before illumination under xenon-lamp-light, (b) after illumination of the solutions under xenon-lamp-light for 50 minutes for different photocatalysts.

## Chapter 3: Sample Preparations and Experimental Techniques

---

In our present investigation, the photocatalytic activities were evaluated by the degradation of Rhodamine-B (RhB) in aqueous solution under visible-light irradiation using a 500 W Xe lamp. In a typical reaction run, 100 mL of RhB (15 mg/L) solution, previously adjusted to a fixed pH value of 2.5 with diluted HCl and NaOH, was added to a glass flask containing 80 mg of the photocatalyst. After the elapse of a period of time, a small quantity of the solution was taken, and the concentration of RhB was determined by measuring the absorbance at 553 nm using a UV-vis spectrophotometer. Each time before the absorption measurement, the sample solution was centrifuged at 5000 rpm.min<sup>-1</sup> for 10 min to separate the catalyst powder from the solution. The absorbance was converted to the RhB concentration referring to a standard curve showing a linear behavior between the concentration and the absorbance at 553 nm.

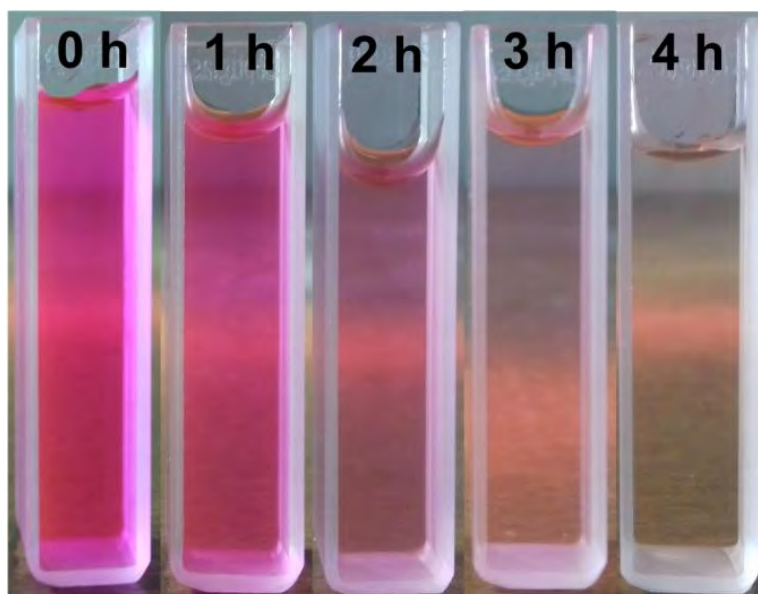


**Figure 3.21:** The illumination of Rhodamine B(RhB) under visible light irradiation.

Figure 3.20 and 3.21 shows the degradation of RhB before and after illumination under visible light. Before illumination, the undegraded RhB solution is shown in figure 3.20 (a). After 50 min illumination under the xenon lamp light the degradation of RhB for different materials as a

photocatalyst as shown in figure 3.20 (b). The outcome of the photocatalytic activity test will be presented in chapter 4.

### 3.9 Magnetization measurement

#### 3.9.1 Vibrating sample magnetometer (VSM)

VSM developed by S. Foner [29] is a versatile and sensitive method of measuring magnetic properties and is based on the flux change in a coil when the sample is vibrated near it. The VSM is an instrument designed to continuously measure the magnetic properties of materials as a function of temperature and field. In this type of magnetometer, the sample is vibrated up and down in a region surrounded by several pickup coils. The magnetic sample is thus acting as a time changing magnetic flux, varying inside a particular region of fixed area.



**Figure 3.22:** EV9 Micro sense Vibrating Sample Magnetometer (Atomic Energy Commission, Bangladesh).

VSM is used to measure the magnetic properties of the sample. The basic principle of VSM lies on Faraday's Law of Induction,  $\nabla \times \vec{E} = \frac{\partial \vec{B}}{\partial t}$  which tells us that a changing

magnetic field (B) will produce an electric field (E). This electric field can be measured and can give us information about the changing magnetic field. Thus, the sample is placed in a constant magnetic field and oscillated with a fixed frequency near a set of detection (pickup) coils. If the sample is magnetic, the constant magnetic field induces a magnetic dipole moment in the sample. This magnetic dipole moment creates a magnetic field around the sample. As the sample is oscillated, this magnetic flux changes as a function of time and the voltage induced (proportional to the rate of change of flux) in the pickup coils is synchronously detected. The voltage will also be proportional to the magnetic moment of the sample. In Figure-3.22, we show (a) schematic of VSM and (b) detailed configuration near the pick-up coils. The system detection capability can be maximized by optimizing the geometry of the pickup coils and by having oscillation amplitude that is relatively large (1 – 3 mm peak). The time dependent voltage induced in the pickup coils is given by

$$V_{induced} = \frac{d\phi}{dt} = \frac{d\phi}{dz} \frac{dz}{dt} \quad (3.5)$$

where,  $\phi$  represents the magnetic flux, the axis of oscillation of the sample is conventionally chosen to be the  $z$ -axis, and  $z$ , therefore, represents the position of the sample along this axis and  $t$  is the time. If the sample is made to oscillate sinusoidally, then the induced voltage in the pickup coils will have the form  $V_{induced} = cmA\omega \sin \omega t$ , where,  $c$  is a coupling constant,  $m$  is the DC magnetic moment of the sample,  $A$  is the amplitude of oscillation, and  $\omega = 2\pi f$ , where  $f$  is the frequency of oscillation of the sample. The detection of the magnetic moment of the sample, thus, amounts to measuring the coefficient of sinusoidal voltage response induced in the detection coil.

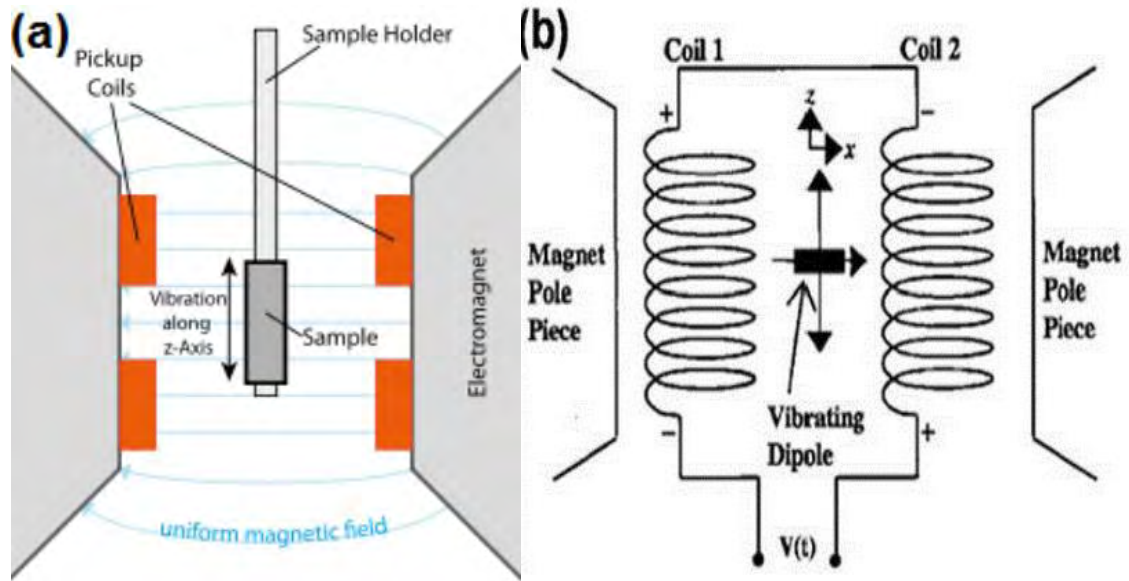


Figure 3.23: Schematic diagram of (a) VSM and (b) details near the pickup coils.

# Bibliography

- [1] Goldman, A., "Handbook of Modern Ferromagnetic Materials", Kulwer Acad. Pub, Boston, U.S.A, 1999.
- [2] Valenzuela, R., "Magnetic Ceramics", Cambridge University Press, Cambridge, 1994.
- [3] West, A. R., "Solid state chemistry and its applications", John Willey Sons, 1887.
- [4] Kingery, W. D., Bowen, H. K., and Uhlman, D. R., Introduction to Ceramics, 2nd edition, Wiley Interscience, New York, 476, 1976.
- [5] McColm, I. J. and Clark, N. J., Forming, "Shaping and Working of high Performance Ceramics", Blackie, Glasgow, 1-338, 1988.
- [6] Basith, M. A., Kurni, O., Alam, M. S., Sinha, B. L. and Bashir Ahammad, "Room temperature dielectric and magnetic properties of Gd and Ti co-doped BiFeO<sub>3</sub> ceramics", J. Appl. Phys., 115, 024102-024107, 2014.
- [7] Kelsall, R. W., Hamley, I. W., Geoghegan, M., "Nanoscale Science and Technology", 2005.
- [8] Taurozzi, J. S., Hackley, V. A., and Wiesner, M. R., "Ultrasonic dispersion of nanoparticles for environmental, health and safety assessment issues and recommendations", Nanotoxicology, 5(4), 711, 2011.
- [9] Hasan, M., Hakim, M. A., Basith, M. A., Hossain, M. S., Ahmad, B., Zubair, M. A., Hussain, A., and Islam, M. F., "Size dependent magnetic and electrical properties of Ba-doped nanocrystalline BiFeO<sub>3</sub>", AIP ADVANCES, 6, 035314, 2016.
- [10] Shankar, S. K., Kar, S., Subbanna, G. N., Raychaudhuri, A. K., "Enhanced ferromagnetic transition temperature in nanocrystalline lanthanum calcium

- manganese oxide ( $\text{La}_{0.67}\text{Ca}_{0.33}\text{MnO}_3$ )”, *Solid State Commun.*, 129, 479, 2004.
- [11] Muroi, M., Street, R., and McCormick, P. G., “Enhancement of critical temperature in fine  $\text{La}_{0.7}\text{Ca}_{0.3}\text{MnO}_3$  particles prepared by mechanochemical processing”, *J. App. Phys.*, 87, 3424, 2000.
- [12] Basith, M. A., Ngo, D. T., Quader, A., Rahman, M. A., Sinha, B. L., Bashir Ahmad, Fumihiko Hirose and Molhave, K., “Simple top-down preparation of magnetic  $\text{Bi}_{0.9}\text{Gd}_{0.1}\text{Fe}_{1-x}\text{Ti}_x\text{O}_3$  nanoparticles by ultrasonication of multiferroic bulk material”, *Nanoscale*, 6, 14336, 2014.
- [13] Markovich, V., Fita, I., Wisniewski, A., Puzniak, R., Mogilyansky, D., Iwanowski, P., Dluzewski, P., and Gorodetsky, G., “Nanometer size effect on magnetic properties of  $\text{Sm}_{0.8}\text{Ca}_{0.2}\text{MnO}_3$  nanoparticles”, *J. Phys. Chem. C*, 116, 435, 2012.
- [14] Curiale, J., Granada, M., Troiani, H. E., Sanchez, R. D., Leyva, A. G., Levy, P., Samwer, K., “Magnetic dead layer in ferromagnetic manganite nanoparticles”, *Appl. Phys. Lett.* 95, 043106, 2009.
- [15] Lampen, P., Bingham, N. S., Phan, M. H., Kim, H., Osofsky, M., Pique, A., Phan,
- [16] T. L., Yu, S. C., and Srikanth, H., “Impact of reduced dimensionality on the magnetic and magnetocaloric response of  $\text{La}_{0.7}\text{Ca}_{0.3}\text{MnO}_3$ ”, *Appl. Phys. Lett.* 102, 062414, 2013.
- [17] Sarkar, T., Raychaudhuri, A. K., Bera, A. K., and Yusuf, S. M., “Effect of size reduction on the ferromagnetism of the manganite  $\text{La}_{1-x}\text{Ca}_x\text{MnO}_3$  ( $x=0.33$ )”, *New J. Phys.*, 12 123026, 2010.
- [18] Ono, K., Kakefuda, Y., Okuda, R., Ishii, Y., Kamimura, S., Kitamura, A. and

- Oshima, M. J., “Organometallic synthesis and magnetic properties of ferromagnetic Sm-Co nanoclusters”, *J. Appl. Phys.*, 91, 8480, 2002.
- [19] Lampen, P., Bingham, N. S., Phan, M. H., Kim, H., Osofsky, M., Pique, A., Phan, T. L., Yu, S. C., and Srikanth, H., “Impact of reduced dimensionality on the magnetic and magnetocaloric response of  $\text{La}_{0.7}\text{Ca}_{0.3}\text{MnO}_3$ ”, *Appl. Phys. Lett.* 102, 062414, 2013
- [20] Roy, S., Dubenko, I., Ederh, D. D., and Ali, N. J., “Size induced variations in structural and magnetic properties of double exchange  $\text{La}_{0.8}\text{Sr}_{0.2}\text{MnO}_{3-\delta}$  nanoferrromagnet”, *J. Appl. Phys.*, 96, 1202, 2004.
- [21] Gencer, H., Cengiz, N. E., Kolat, V. S., Izgi, T. and Atalay, S., “Production of  $\text{LaCaMnO}_3$  Composite by Ball Milling”, *Acta Phys. Pol. A*, 125, 214, 2014.
- [22] Brankovic, Z., Marinkovic, Stanojevic. Z., Mancic, L., Vukotic, V., Bernik, S., and Brankovic, G., “Multiferroic bismuth manganite prepared by mechanochemical synthesis”, *J. Eur. Ceram. Soc.*, 30, 277, 2010.
- [23] Marinkovic, S. Z., Brankovic, Z., Jaglicic, Z., Jagodic, M., Mancic, L., Bernik, S., Recnik, A., and Brankovic, G., “Structural and magnetic properties of nanocrystalline bismuth manganite obtained by mechanochemical synthesis”, *J. Nanopart. Res.*, 13, 3431, 2011.
- [24] Ahmmad, B., Islam, M. Z., Billah, A., and Basith, M. A., “Large difference between the magnetic properties of Ba and Ti co-doped  $\text{BiFeO}_3$  bulk materials and their corresponding nanoparticles prepared by ultrasonication”, *J. Phys. D: Appl. Phys.*, 2016.
- [25] Rietveld H. M., “profile refinement method for nuclear and magnetic structures”, *J. Appl. Crystallogr.*, 2, 65, 1965.
- [26] Rodriguez-Carvajal, J., Fullprof.2k computer program, version 4.70, 2009.
- Brundle, C. R., Evans, C. A., and Wilson, S., editors, *Encyclopedia of*

Materials Characterization, Butterworth-Heinemann, 1992.

- [27] Wang, Y. P., Zhou, L., Zhang, M. F., Chen, X. Y., Liu, J.-M., and Liu, Z. G.,  
“Room-temperature saturated ferroelectric polarization in BiFeO<sub>3</sub> ceramics  
synthesized by rapid liquid phase sintering”, Appl. Phys. Lett., 84, 10, 2004.
- [28] Wang, Y. P., Zhou, L., Zhang, M. F., Chen, X. Y., Liu, J.-M., and Liu, Z. G.,  
“Room-temperature saturated ferroelectric polarization in BiFeO<sub>3</sub> ceramics  
synthesized by rapid liquid phase sintering”, Appl. Phys. Lett., 84, 10, 2004.
- [29] Foner, S., “Versatile and Sensitive Vibrating-Sample Magnetometer”, Rev. Sci.  
Instr., 30, 7, 1959

# Chapter 4

## Results and Discussion

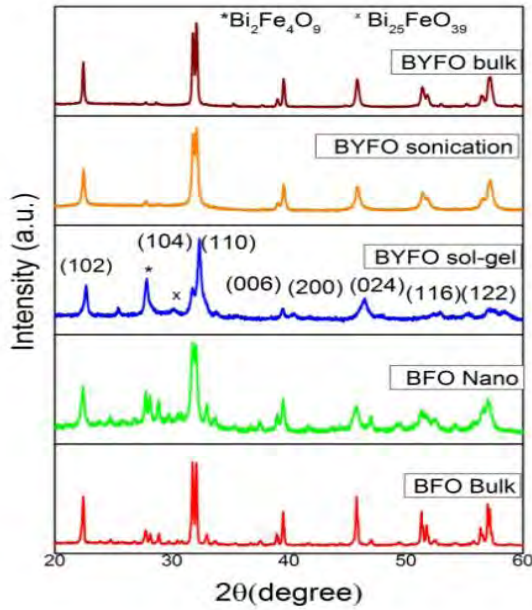
### 4.1 Introduction

This chapter is discussed about the investigation of structural, morphological, optical, photocatalytic and magnetic properties of synthesized bulk polycrystalline materials of  $\text{BiFeO}_3$  (BFO) and  $\text{Bi}_{0.9}\text{Y}_{0.1}\text{FeO}_3$  (BYFO) prepared by solid state reaction technique and their corresponding nanoparticles fabricated by ultrasonication technique and sol-gel method.

### 4.2 Crystal Structure Analysis

The structural properties  $\text{BiFeO}_3$  (BFO) and  $\text{Bi}_{0.9}\text{Y}_{0.1}\text{FeO}_3$  bulk and their corresponding nanoparticles were analyzed at room temperature (RT) by X-ray diffraction (XRD) using  $\text{CuK}\alpha$  ( $\lambda=1.5418 \text{ \AA}$ ) radiation. The XRD patterns of the  $\text{Bi}_{0.9}\text{Y}_{0.1}\text{FeO}_3$  bulk materials and their corresponding nanoparticles with rhombohedral crystal structure are shown in figures 4.1(a) and 4.1(b), respectively. The bulk undoped BFO materials and their nanoparticles appeared significant number of secondary phases as shown in figure 4.1 (a). Based on the reported data [1,2], both the impurity phases along with original R3c structure are indexed and shown in Figure 4.1 (a and b). During the solid state synthesis of bulk undoped BFO, and cations substituted BFO, the formation of these secondary phases were observed in a number of previous investigations [3–6].

In the XRD patterns, figure 4.1 (a), the (110) and (104) peaks are associated with twin peaks [7,8] of undoped BFO bulk and nano materials. For both BYFO bulk and BYFO nano prepared by ultrasonication the (110) ( $2\theta = 32.13$ ) and (104) ( $2\theta = 31.82$ ) peaks are twin peaks but the peak intensity of (110) is little bit greater than the pick intensity of (104). For BYFO nano prepared by sol-gel, the peak intensity of (110) ( $2\theta=32.35$ ) is significantly greater than the peak intensity of (104) ( $2\theta=31.77$ ). The decrease intensity of (104) peak and the shifting of (110) peak to the higher angle clearly show the structural phase transition from rhombohedra to orthorhombic. [9]



(a)

(b)

**Figure 4.1:** (a) X-ray diffraction patterns of the synthesized bulk materials and their corresponding nanoparticles (b): Magnified view of X-ray diffraction pattern.

The crystal structure of bismuth ferrite is a rhombohedrally distorted perovskite that belongs to the space group  $R3c$ . Compounds with the formula  $\text{Bi}_{0.9}\text{Y}_{0.1}\text{FeO}_3$  (prepared by sol-gel) is showed a perovskite orthorhombically distorted structure [9]. This phase transition may be due to the difference in the radius of  $\text{Y}^{3+}$  ions ( $1.04 \text{ \AA}$ ) compared to  $\text{Bi}^{3+}$  ions ( $1.17 \text{ \AA}$ ). The structural parameters obtained for the pure and doped samples are given in Table 4.1 by using the following equation.

$$\sin^2\theta = \frac{\lambda^2}{3a^2} (h^2 + hk + k^2) + \frac{\lambda^2 l^2}{4c^2} \quad (4.1)$$

The structural parameters of the undoped BFO bulk sample are reasonably close to the reported values in the literature [9,10]. For doped bulk samples and their corresponding nanoparticles, the lattice parameters decreased for the 10% Y doping. The decrement in the structural parameters can be explained on the basis of Goldschmidt tolerance factor ( $t$ ), which is associated with the cationic size variation (Shannon ionic radii) between A and B site ions [11–13].

## Chapter4: Results and Discussion

**Table 4.1:** The table shows the calculated lattice parameters of the synthesized nanoparticle.

Sample	Prepared By	Lattice parameters	
		a = b (Å)	c (Å)
Bi <sub>0.9</sub> Y <sub>0.1</sub> FeO <sub>3</sub> (Nano)	Sol-gel	5.535	14.077
Bi <sub>0.9</sub> Y <sub>0.1</sub> FeO <sub>3</sub> (Nano)	Ultrasonication	5.572	13.880
Bi <sub>0.9</sub> Y <sub>0.1</sub> FeO <sub>3</sub> (Bulk)	Solid-state	5.578	13.850
BFO(Nano)	Sol-gel	5.583	13.824
BFO(Bulk)	Solid-state	5.580	13.839

The average crystallite size (d) was calculated from XRD patterns by applying Scherrer's formula [2]:

$$d = \frac{k\lambda}{\beta \cos\theta} \quad (4.2)$$

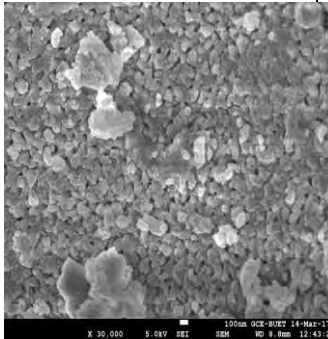
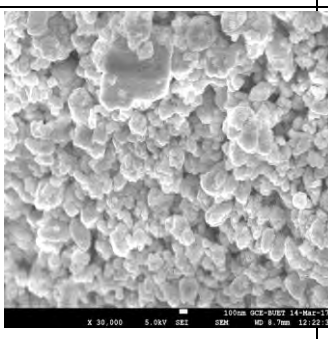
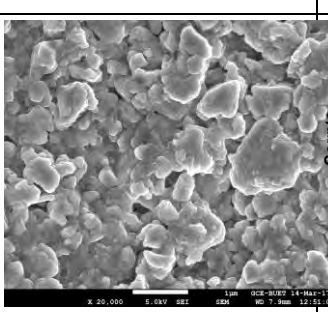
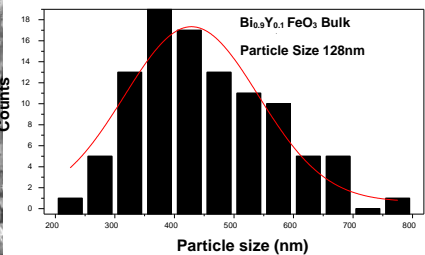
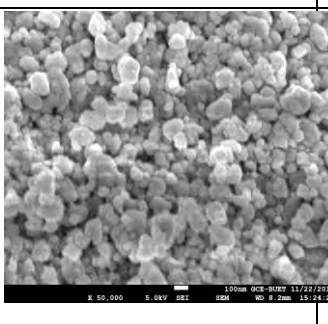
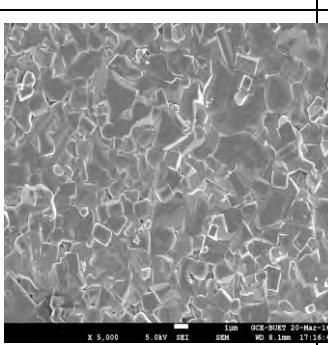
where k is the dimensionless shape factor with a typical value of about 0.94,  $\lambda$  is the wavelength of CuK $\alpha$  radiation with the value of 1.5418Å,  $\theta$  is the Bragg angle for the (102) diffraction peak and  $\beta$  is the full width at half maximum (FWHM) intensity of the corresponding diffraction peak. Using Scherrer formula the calculated values of crystallite size were shown in table 4.2

**Table 4.2:** The table shows the average crystallite size (calculated from XRD patterns) and average particle size (calculated from FESEM images)

Sample	Crystallite size (nm)	Particle size (nm)
BFO(Bulk)	74	750
BFO(Nano)	22	94
BYFO(Bulk)	73	428
BYFO (Nano) (by Ultrasonication)	23	88
BYFO (Nano) (by Sol-gel)	18	82

### 4.3 Morphological Analysis

To investigate the surface structure of the pellets, FESEM imaging was carried out for all of the samples. Figure 4.2 demonstrates the surface morphology of the pellets of the undoped and doped BFO bulk polycrystalline materials and their corresponding nanoparticles. It can also be seen that Y doping changes the morphology and size of the particles significantly. The smaller grain size is probably due to smaller size of  $Y^{3+}$  ions as compared to those of  $Bi^{3+}$  ions and results in lattice contraction. The particle size distribution is pretty homogeneous for each sample in the figure 4.2. Figure 4.2 (a,b,c,d, and e), show the histograms of the particle size distributions.

 <p>(a)</p>	<p><math>\text{Bi}_{0.9}\text{Y}_{0.1}\text{FeO}_3</math> Nanoparticles(Sol-gel)</p> <p>Average Particle size 82 nm</p>
 <p>(b)</p>	<p><math>\text{Bi}_{0.9}\text{Y}_{0.1}\text{FeO}_3</math> Nanoparticles(Ultra sonication)</p> <p>Average Particle size 88 nm</p>
 <p>(c)</p>	 <p><math>\text{Bi}_{0.9}\text{Y}_{0.1}\text{FeO}_3</math> Bulk (Solid-state)</p> <p>Average Particle size 428 nm</p>
 <p>(d)</p>	<p>BFO Nanoparticles(Sol-gel)</p> <p>Average Particle size 94 nm</p>
 <p>(e)</p>	<p>BFO Bulk (Solid-state)</p> <p>Average Particle size 750 nm</p>

**Figure 4.2:** FESEM images of the (a)  $\text{B}_{0.9}\text{Y}_{0.1}\text{FeO}_3$  Nanoparticles (Sol-gel) (b)  $\text{B}_{0.9}\text{Y}_{0.1}\text{FeO}_3$  Nanoparticles (Ultra sonication) (c)  $\text{B}_{0.9}\text{Y}_{0.1}\text{FeO}_3$  Bulk (Solid-state) (d) BFO Nanoparticles (Sol-gel) (e) BFO Bulk (solid state)

## 4.4 Optical Measurement

### 4.4.1 Absorbance and band gap estimation

The absorbance spectra of the selected samples were investigated with an aim to probing their optical properties as shown in figure 4.3 (a) BFO bulk polycrystalline powder materials and BFO nanoparticles are shown the absorption edges at 725 nm and 635 nm respectively, and (b) The absorption edges for  $B_{0.9}Y_{0.1}FeO_3$  bulk,  $B_{0.9}Y_{0.1}FeO_3$  nanoparticles (prepared by Ultrasonication) and  $B_{0.9}Y_{0.1}FeO_3$  nanoparticles (prepared by Sol-gel) at 630 nm, 614 nm, and 693 nm respectively, indicating that these materials can absorb light with wavelength from UV to visible region. However, the absorption edge of BYFO bulk materials evidently red-shifted may be due to their microstructure. For 10% Y doped BFO (prepared by Ultrasonication) nanosized materials was found to be blue-shifted due to the modification of band gap energy, but for 10% Y doped BFO (prepared by sol-gel) the absorption edge found to be red shifted, because of orthorhombically phase transition, it absorb visible light of more wavelength.

**Figure4.3:** (a) Absorption spectra for  $BFeO_3$  bulk materials and its corresponding nanoparticles (b) Absorption spectra for  $B_{0.9}Y_{0.1}FeO_3$  bulk materials and their corresponding nanoparticles

**Figure 4.4:** Kubelka Munk (KM) plot to estimate the band gap energy of the synthesized (a) BFO nano and (b) BFO bulk (c)  $\text{Bi}_{0.9}\text{Y}_{0.1}\text{FeO}_3$  bulk,  $\text{Bi}_{0.9}\text{Y}_{0.1}\text{FeO}_3$  Nano (prepared by Sol-gel) and  $\text{Bi}_{0.9}\text{Y}_{0.1}\text{FeO}_3$  Nano (prepared by Ultrasonication) samples.

The direct band gap energies of the samples were estimated from their Diffuse Reflectance Spectra (DRS) graphs by applying Kubelka Munk (KM) function as shown in figure 4.4. Using this method, the band gap energy of the 10% Y doped BFO bulk polycrystalline powder materials was estimated to be 2.12 eV consistent with literature report [30-34]. The band gap energy (2.24 eV) increased for the 10% Y doped BFO nano (prepared by ultrasonication) material. But the band gap energy (2.00 eV) for the 10% Y doped BFO nano (prepared by sol-gel) material which is very much consistent with the reported value of *Antonio Perejon et al* [35]. It is possible that the electronic structure of the  $\text{Bi}_{0.9}\text{Y}_{0.1}\text{FeO}_3$  bulk,  $\text{Bi}_{0.9}\text{Y}_{0.1}\text{FeO}_3$  nano (ultrasonication) and  $\text{Bi}_{0.9}\text{Y}_{0.1}\text{FeO}_3$  nano (sol-gel) would be affected due to the structural changes owing to the 1D structure as suggested from their XRD patterns.

### 4.4.2 Photocatalytic activity test

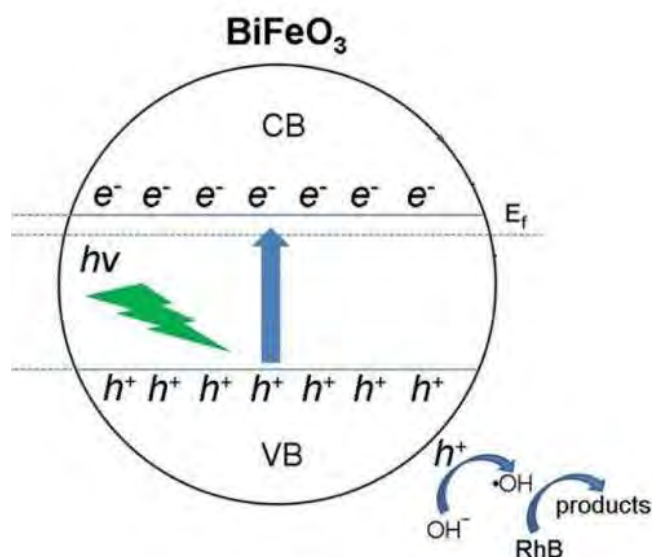
Recent studies suggested that BFO exhibit efficient visible-light photocatalytic activity for water splitting and degradation of organic pollutants due to its small band gap [36]. The photocatalytic activities were evaluated by the degradation of Rhodamine-B (RhB) in aqueous solution under visible-light irradiation using a 500 W Xenon lamp as a solar simulator. In a typical reaction run, 100 mL of RhB (5mg/L) solution, previously adjusted to a fixed pH value with diluted HCl and NaOH, was added to a glass flask containing 80 mg of the photocatalyst. After the elapse of a period of time, a small quantity of the solution was taken, and the concentration of RhB was determined by measuring the absorbance at 553 nm using a UV-vis spectrophotometer. Each time before the absorption measurement, the sample solution was filtered to separate the catalyst powder from the solution.

Figure 4.5(a-d) shows the time-dependent photodegradation of RhB under visible light irradiation with the photocatalysts of (a) undoped BFO bulk, (b) 10% Y doped BYFO nano synthesized by the ultrasonication and (c) 10% Y doped BYFO nano prepared by sol-gel method. In all cases (as shown in figure 4.5(a-d)), the absorbance peak intensity of RhB solution at 553 nm apparently decreased as the reaction time increased, indicating intense decomposition of RhB under visible-light irradiation with the presence of different materials as photocatalyst. Dark test, (RhB without any catalyst) with the absence of visible light exhibited an infinitesimal photolysis, which showed that the self-degradation of RhB in dark condition is almost zero as shown in figure 4.5 (e). Light test (RhB without any catalyst) under visible light exhibit little photolysis, which demonstrated that the self-degradation of RhB is slow; only 20% of RhB is photolyzed after 50 minutes illumination. In addition, after 50 minutes illumination of visible light with undoped BFO bulk polycrystalline bulk powder materials, the RhB degradation rate is about 60% while 10% Y doped BFO bulk materials displayed 70% degradation of RhB dye, indicating that the photodegradation rate increases with the Y doping at Bi side of BFO bulk materials. Interestingly, 10% Y doped BFO nanoparticles (prepared by sol-gel) under visible light exhibited

**Figure 4.5:** Photocatalytic degradation spectra by (a) BFO bulk materials, (b) BFO nanoparticles (c)  $\text{Bi}_{0.9}\text{Y}_{0.1}\text{FeO}_3$  nanoparticles (Sol-gel) and (d)  $\text{Bi}_{0.9}\text{Y}_{0.1}\text{FeO}_3$  nanoparticles (Ultrasonication) (e)  $\text{Bi}_{0.9}\text{Y}_{0.1}\text{FeO}_3$  bulk materials (f) Their  $C/C_0$  ratio graphs.

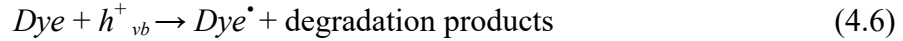
that the degradation rate of RhB is almost about 80% with 40 minutes illumination shown in figure 4.5 (e). However, the absorption peaks corresponding to RhB decreased after about 40 min suggesting the good photocatalytic activity of the 10% Y doped BFO nanoparticles (prepared by sol-gel). The photocatalytic activity is affected by many factors, which can cooperate with each other and enhance the photocatalytic activity. Among them, the particle size and surface area are important factors. Another important fact is the band gap. It has been reported that Y doped BFO nanoparticles (prepared by sol-gel) exhibited a decreased band gap, which might increase the photocatalytic activity [37-39].

### 4.4.3: Photocatalytic Mechanism



**Figure 4.6:** Schematic illustration of the photocatalytic mechanism of BFO photocatalyst toward the degradation of RhB.

Figure 4.6 schematically shows the photocatalytic mechanism of BFO photocatalyst toward the degradation of RhB. When BFO is irradiated with light of energy greater than its  $E_g$ , electrons are excited from the valence band to the conduction band, leaving behind holes in the conduction band. The photogenerated holes are expected to react with  $\text{OH}^-$  and/or  $\text{H}_2\text{O}$  adsorbed on the photocatalyst surface to generate  $\cdot\text{OH}$  radicals, which are thought to be the dominant active species responsible for the degradation reaction [49-51]. Therefore, the effective suppression of  $e^-$ - $h^+$  pair recombination and increased availability of  $h^+$  is the key point to improve the photocatalytic activity of the photocatalyst. The degradation path way of the dye molecules could be given as the following Eqs<sub>82</sub>



Therefore, the effective separation of charge carriers and rich availability of holes are the major cause of the observed enhanced photocatalytic activity of the Y doped BFO nanostructures.

## 4.5 Magnetic Characterization

For field dependent magnetic characterization, the M-H hysteresis loops of BFO bulk and nano,  $Bi_{0.9}Y_{0.1}FeO_3$  bulk materials and their corresponding nanoparticles were measured at room temperature with an applied magnetic field of up to  $\pm 20$  kOe. The room temperature M-H loops of BFO bulk samples and their corresponding nanoparticles are displayed in figure 4.7 (a). Figure 4.7 (b) shows the enlarged view of BFO bulk and nano polycrystalline powder materials prepared by solid state reaction technique. In figure 4.7 (a), the linear M-H curve of bulk BFO demonstrates its antiferromagnetic nature [45, 46].

**Table 4.3:** Remanent magnetization, coercivity and saturation magnetization of the synthesized bulk powder materials and their corresponding nanoparticles.

<i>Parameters</i>	<b>Bulk Materials (<math>Bi_{1-x}Y_xFeO_3</math>)</b>		<b>Nanoparticles (Ultrasonication) (<math>Bi_{1-x}Y_xFeO_3</math>)</b>		<b>Nanoparticles (Sol-gel) (<math>Bi_{1-x}Y_xFeO_3</math>)</b>
	x = 0.00	x = 0.10	x = 0.00	x = 0.10	x = 0.10
$M_r$ (emu/g)	-	0.032	0.005	0.022	0.510
$H_c$ (Oe)	-	22.21	159	174.98	100.46
$M_s$ (emu/g)	-	1.46	0.008	0.059	4.57

**Figure 4.7:** The room temperature M-H hysteresis loops of BFO and  $\text{Bi}_{0.9}\text{Y}_{0.1}\text{FeO}_3$  (a) BFO bulk and nano materials (b) The enlarged view of hysteresis loops of BFO bulk and nano particles (c) M-H hysteresis loops of  $\text{Bi}_{0.9}\text{Y}_{0.1}\text{FeO}_3$  bulk and their corresponding nanoparticles (prepared by both Ultrasonication and Sol-gel technique) (d) The enlarged view of the hysteresis loops of  $\text{Bi}_{0.9}\text{Y}_{0.1}\text{FeO}_3$  bulk and their corresponding nanoparticles (prepared by both Ultrasonication and Sol-gel technique)

It should be noted that the M-H hysteresis loop of undoped BFO nanoparticles exhibits a small loop at the center of the hysteresis with a coercivity of 159 Oe and remanent magnetization of 0.005 emu/g. This value of magnetization of undoped BFO nanoparticles

compared to that of bulk undoped BFO materials is also worth noting. Thus the magnetic properties of undoped BFO nanoparticles are improved than that of bulk counterpart.

The potential magnetization locked in the spin cycloid of the BFO can be released by destroying the cyclic spin structure upon Y doping. Also an asymmetric shift of the M-H hysteresis loop (Figure 4.7(d)) is observed for  $\text{Bi}_{0.9}\text{Y}_{0.1}\text{FeO}_3$  nanoparticles (prepared by sol-gel) indicates the coexistence of AFM and FM orderings [47,48]. Also the increasing of coercivity for  $\text{Bi}_{0.9}\text{Y}_{0.1}\text{FeO}_3$  nanoparticles (prepared by sol-gel) indicates that the shifting of soft magnetic material to hard magnetic material. And the saturation magnetization is high for  $\text{Bi}_{0.9}\text{Y}_{0.1}\text{FeO}_3$  nanoparticles (prepared by sol-gel)

### 4.6 Ferroelectric Behavior

The ferroelectric measurements were carried out with a fixed value of frequency 50 Hz to establish polarization (P) versus electric field (E) hysteresis loops (P-E) at applied field with a maximum value of  $\pm 4$  kV/cm for doped and undoped bulk polycrystalline powder materials and  $\pm 10$  kV/cm for nanoparticles. The P-E loops of undoped and doped BFO bulk materials and their corresponding nanoparticles are shown in figures 4.8 (a),(b),(c) and (d) respectively. The ferroelectricity of bulk powders as well as their corresponding nanoparticles was evidenced by the P-E loops. The bulk BFO exhibit a round shaped P-E loop as shown in figure 4.8 (c) due to their high leakage current which is in fact related to oxygen vacancies and space charge defects. In the case of nanoparticles, figure 4.8 (b), the P-E loops become more typical which is expected due to their reduced leakage current density [14-18] and the decrease of space charge defect which reduces with driven frequency is also given, as shown in the Figure 4.7 (c) for doped bulk polycrystalline materials which exhibit that the maximum polarization is very high at low frequency for both samples [25-30].

**Figure 4.8:** The P-E hysteresis loop for (a) BFO Nanoparticles (b)  $\text{Bi}_{0.9}\text{Y}_{0.1}\text{FeO}_3$  Nano (Sol-gel) (c) BFO Bulk (d)  $\text{Bi}_{0.9}\text{Y}_{0.1}\text{FeO}_3$ (Ultrasonication)

The polarization of the nanoparticles was found to decrease compared to that of bulk materials and this is consistent with previous investigation which reported the reduction of the polarization of BFO with reduced particle size [19-25].

# Bibliography

- [1] Basith, M. A., Kurni, O., Alam, M. S., Sinha, B. L., and Ahmmad, B., “Room temperature dielectric and magnetic properties of Gd and Ti co-doped BiFeO<sub>3</sub> ceramics”, *J. App. Phys.*, 115, 024102, 2014.
- [2] Pradhan, S. K., Das, J., Rout, P. P., Mohanta, V. R., Das, S. K., Samantray, S., Sahu, D. R., Huang, J. L., Verma, S. and Roul, B. K., “Effect of holmium substitution for the improvement of multiferroic properties of BiFeO<sub>3</sub>”, *J. Phys. chem. solid*, 71, 1557, 2010.
- [3] Bernardo, M. S., Jardiel, T., Peiteado, M. F., Mompean, J., Garcia-Hernandez, M., Garcia, M. A., Villegas, M. and Caballero, A. C., “Intrinsic Compositional Inhomogeneities in Bulk Ti-Doped BiFeO<sub>3</sub>: Microstructure Development and Multiferroic Properties”, *Chem. Mater.*, 25, 1533, 2013.
- [4] Fisher, J. G., Seo-Hee, J., Mi-So, P., Sun H., Su-Hyun, M., Jong-Sook, L., and Ali, H., “The Effect of Niobium Doping on the Electrical Properties of 0.4(Bi<sub>0.5</sub>K<sub>0.5</sub>)TiO<sub>3</sub>-0.6BiFeO<sub>3</sub> Lead-Free Piezoelectric Ceramics”, *Materials*, 8, 8183, 2015.
- [5] Dang, N. V., Thanh, T. D., Hong, L. V., Lam, V. D., and The-Long, P., “Structural, optical and magnetic properties of polycrystalline BaTi<sub>1-x</sub>FexO<sub>3</sub> ceramics”, *J. App. Phys.* 110, 043914, 2011.
- [6] Pradhan, S. K., and Roul, B. K., “Effect of Gd doping on structural, electrical and magnetic properties of BiFeO<sub>3</sub> electroceramic”, *J. Phys. Chem. Solids*, 72, 1180, 2011
- [7] Bernardo, M. S., Jardiel, T., Peiteado, M., Caballero, A. C. and Villegas, M., “Reaction pathways in the solid state synthesis of multiferroic BiFeO<sub>3</sub>”, *J. Eur. Ceram. Soc.*, 31, 3047, 2011.
- [8] Jian-Ping, Z., Ruo-Lin, Y., Rui-Juan, X., Xiao-Ming, C., and Chao-Yong, D., “Structure and phase transition of BiFeO<sub>3</sub> cubic micro-particles prepared by hydrothermal method”, *Mater. Res. Bull*, 47, 3630, 2012.
- [9] Shirolkar, M. M., Das, R., Maity, T., Poddar, P., and Kulkarni, S. K., “Observation of Enhanced Dielectric Coupling and Room Temperature Ferromagnetism in Chemically

- Synthesized BiFeO<sub>3</sub>.SiO<sub>2</sub> Core Shell Particles”, J. Phys. Chem. C, 116, 19503-19511, 2012.
- [10] F. Kubel and H. Schmid, “Structure of a Ferroelectric and Ferroelastic Mon- odomain Crystal of the Perovskite BiFeO<sub>3</sub>”, Acta Crystallogr., Sect. B: Struct. Sci., B46, 698-702, 1990.
- [11] Shannon, R. D., “Revised effective ionic radii and systematic studies of interatomic distances in halides and chalcogenides” Acta Crystallogr., Sect. A: Cryst. Phys., Diffr., Theor. Gen. Crystallogr., A32, 751-767, 1976.
- [12] P. M. Woodward., “Octahedral Tilting in Perovskites. II. Structure Stabilizing Forces”, Acta Crystallogr., Sect. B: Struct. Sci., 53, 4466, 1997.
- [13] Nikola I.Ilic., Jelena D.Bobi c., Bojan S. Stojadinovi c, Adis S. Dzunuzovi c, Mirjana M.Vijatovi c, Petrovi c, Zorana D.Doh Mitrovic., Biljana D.Stojanovi c., “Improving of the electrical and magnetic properties of BiFeO<sub>3</sub> by doping with yttrium”, Materials Research Bulletin 10,1016,2016.
- [14] Basith, M. A., Ngo, D -T., Quader, A., Rahman, M. A., Sinha, B. L., Bashir, A., and Hirose, F., “Simple top-down preparation of magnetic Bi<sub>0.9</sub>Gd<sub>0.1</sub>Fe<sub>1-x</sub>Ti<sub>x</sub>O<sub>3</sub> nanoparticles by ultrasonication of multiferroic bulk ma- terial”, Nanoscale, 6, 14336, 2014
- [15] Wang, Y. P., Zhou, L., Zhang, M. F., Chen, X. Y., Liu, J.-M., and Liu, Z. G., “Room-temperature saturated ferroelectric polarization in BiFeO<sub>3</sub> ceramics synthesized by rapid liquid phase sintering”, Appl. Phys. Lett., 84, 1731, 2004.
- [16] Makhdoom, A. R., Akhtar, M. J., Rafiq, M. A., and Hassan, M. M., “Investigation of transport behavior in Ba doped BiFeO<sub>3</sub>,” Ceram. Int., 38, 3829, 2012.
- [17] Cheng, Z., Wang, X., Dou, S., Kimura, H., and Ozawa, K., “Improved ferroelectric properties in multiferroic BiFeO<sub>3</sub> thin films through La and Nb codoping”, Phys. Rev. B, 77, 092101, 2008.
- [18] Deng, H., Zhang, M., Zhou, H., Qunfeng, X., Zhong, Q., Jizhou, W. and Hui, Y., “Enhanced dielectric and ferroelectric properties of Ba and Ti co-doped BiFeO<sub>3</sub> multiferroic ceramics”, J. Alloys Compd., 582, 273, 2014.
- [19] Mukherjee, A., Basu, S., Manna, P. K., Yusuf, S, M., and Pal, M., “Giant mag-

- netodielectric and enhanced multiferroic properties of Sm doped bismuth ferrite nanoparticles”, *J. Mater. Chem. C*, 2, 5885-5891, 2014.
- [20] Selbach, S. M., Tybell, T., Einarsrud, M. A., and Grande, T., “Size-Dependent Properties of Multiferroic BiFeO<sub>3</sub> Nanoparticles”, *Chem. Mater.*, 19, 6478, 2007.
- [21] Wongdamnern, N., Triamnak, N., Ngamjarrojana, A., Ananta, S., Laosiritaworn, Y., Yimnirun, R., “Stress-Dependent Scaling Behavior of Sub-Coercive Field Dynamic Hysteresis in Pb(Zr<sub>1/2</sub>Ti<sub>1/2</sub>)O<sub>3</sub>-Pb(Zn<sub>1/3</sub>Nb<sub>2/3</sub>)O<sub>3</sub> Ceramic Systems”, *Ferroelectrics*, 384, 1-9, 2009.
- [22] Ahmmad, B., Kanomata, K., Koike, K., Kubota, S., Kato, H., Hirose, F., Billah, Areef., Jalil, M. A., and Basith, M. A., “Large difference between the magnetic properties of Ba and Ti co-doped BiFeO<sub>3</sub> bulk materials and their corresponding nanoparticles prepared by ultrasonication”, *J. Phys. D: App. Phys.*, 2016.
- [23] Dutta, D. P., Mandal, B. P., Naik, R., Lawes, G., Tyagi, A. K., “Magnetic, Ferroelectric, and Magnetocapacitive Properties of Sonochemically Synthesized Sc-Doped BiFeO<sub>3</sub> Nanoparticles”, *J. Phys. Chem. C*, 117 (5), 2382, 2013.
- [24] Dutta, D. P., Mandal, B. P., Mukadam, M. D., Yusuf, S. M., Tyagi, A. K., “Improved magnetic and ferroelectric properties of Sc and Ti codoped multiferroic nano BiFeO<sub>3</sub> prepared via sonochemical synthesis”, *Dalton Trans.*, 43, 7838, 2014.
- [25] Chen, Z., Yongpeng, W., and Jianqiang, H., “Ethanol-Assisted Hydrothermal Synthesis and Characterization of BiFeO<sub>3</sub> Nanopowders”, *J. Am. Ceram. Soc.*, 96 (5), 1345-1348, 2013.
- [26] Pavana, S. V. M., Karthik, C., Ubig, R., Ramachandra Rao, M.S., and Sudakar, C., “Tunable bandgap in BiFeO<sub>3</sub> nanoparticles: The role of microstrain and oxygen defects”, *Appl. Phys. Lett.*, 103, 022910, 2013.
- [27] Clark, S. J. and Robertson, J., “Band gap and Schottky barrier heights of multiferroic BiFeO<sub>3</sub>”, *Appl. Phys. Lett.* 90, 132903, 2007.
- [28] J. B. Neaton, C. Ederer, U. V. Waghmare, N. A. Spaldin, and K. M. Rabe, “First-

- principles study of spontaneous polarization in multiferroic BiFeO<sub>3</sub>”, Phys. Rev. B, 71, 014113, 2005.
- [29] Xu, X. S., Brinzari, T. V., Lee, S., Chu, Y. H., Martin, L. W., Kumar, A., McGill, S., Rai, R. C., Ramesh, R., Gopalan, V., Cheong, S. W. and Musfeldt, J. L., “Optical properties and magnetochromism in multiferroic BiFeO<sub>3</sub>”, Phys. Rev. B, 79, 134425 (2009).
- [30] Ramachandran, B., Dixit, A., Naik, R., Lawes, G., and Rao, M. S. R., “Charge transfer and electronic transitions in polycrystalline BiFeO<sub>3</sub>”, Phys. Rev. B, 82, 012102, 2010.
- [31] Ramachandran, B., Dixit, A., Naik, R., Lawes, G., and Rao, M. S. R., “Dielectric relaxation and magneto-dielectric effect in polycrystalline Bi<sub>0.9</sub>Ca<sub>0.1</sub>FeO<sub>2.95</sub>”, Appl. Phys. Lett., 100, 252902, 2012.
- [32] Ramachandran, B. and Rao, M. S. R., “Chemical pressure effect on optical properties in multiferroic bulk BiFeO<sub>3</sub>”, J. Appl. Phys., 112, 073516, 2012.
- [33] Jung, J. H., Matsubara, M., Arima, T., He, J. P., Kaneko, Y., and Tokura, Y., “Optical Magnetoelectric Effect in the Polar GaFeO<sub>3</sub> Ferrimagnet”, Phys. Rev. Lett., 93, 037403, 2004.
- [34] Mukherjee, A., Hossain, Sk. M., Pal, M. and Basu, S., “Effect of Y-doping on optical properties of multiferroics BiFeO<sub>3</sub> nanoparticles”, Appl. Nanosci., 2, 305, 2012.
- [35] Perejon, A., Gil-Gonzalez, E., Sanchez-Jime, E.P., Criado M. J., and Perez-Maqueda A.L., “Structural, Optical, and Electrical Characterization of Yttrium Substituted BiFeO<sub>3</sub> Ceramics Prepared by Mechanical Activation”, ACS.inorgchem, 5b01654, 622, 8, 2015.
- [36] Guo, R., Fang, L., Dong, W., Zheng, F. and Shen, M., “Enhanced photocatalytic activity and ferromagnetism in Gd doped BiFeO<sub>3</sub> nanoparticles”, J. Phys. Chem. C, 114, 21390-21396, 2010.
- [37] Yu, J. Q., Kudo, A., “Effects of Structural Variation on the Photocatalytic Performance of Hydrothermally Synthesized BiVO<sub>4</sub>”, Adv. Funct. Mater., 16, 2163, 2006.
- [38] Fu, H. B., Pan, C. S., Yao, W. Q., Zhu, Y. F., “Visible-Light-Induced Degradation of

- Rhodamine B by Nanosized  $\text{Bi}_2\text{WO}_6$ ”, *J. Phys. Chem. B*, 109, 22432, 2005.
- [39] Zhang, A., Zhang, J., “Effects of europium doping on the photocatalytic behavior of  $\text{BiVO}_4$ ”, *J. Hazard. Mater.*, 173, 265, 2010.
- [40] Zhang, Z.; Wu, P.; Chen, L.; Wang, J. L., “Systematic variations in structural and electronic properties of  $\text{BiFeO}_3$  by A-site substitution”, *Appl. Phys. Lett.*, 96, 012905, 2010.
- [41] Bhardwaj, A., Burbure, N. V., Chen, L., Gamalski, A. and Rohrer, G. S., “Composition Dependence of the Photochemical reduction of Ag by  $\text{Ba}_{1-x}\text{Sr}_x\text{TiO}_3$ ”, *Chem. Mater.*, 22, 3257, 2010.
- [42] Linsebigler, A. L., Lu, G. Q., and Yates, J. T., “Photocatalysis on  $\text{TiO}_2$  Surfaces: Principles, Mechanisms, and Selected Results”, *Chem. Rev.* 95, 735, 1995.
- [43] Ramachandran, B., Dixit, A., Naik, R., Lawes, G., and Ramachandra Rao, M. S., “Weak ferromagnetic ordering in Ca doped polycrystalline  $\text{BiFeO}_3$ ”, *J. Appl. Phys.*, 111, 023910, 2012.
- [44] Rao, T. D., and Asthana, S., “Evidence of improved ferroelectric phase stabilization in Nd and Sc co-substituted  $\text{BiFeO}_3$ ”, *J. Appl. Phys.*, 116, 164102, 2014.
- [45] Khomchenko, V. A., and Kiselev, D. A., “Synthesis and multiferroic properties of  $\text{Bi}_{0.8}\text{A}_{0.2}\text{FeO}_3$  (A=Ca,Sr,Pb) ceramics”, *Appl. Phys. Lett.*, 90, 242901, 2007.
- [46] Huang, F., Wang, Z., Lu, X., Zhang, J., Min, K., Lin, W., Ti, R., Xu, T., He, J., Yue, C. and Zhu, J., “Peculiar magnetism of  $\text{BiFeO}_3$  nanoparticles with size approaching the period of the spiral spin structure”, *Sci. Rep.*, 2013, 3, 2907.
- [47] Soegijono, B., Suharno, Hidayati, R., and Suastiyanti, D., “Enhanced Microwave Absorption Properties of Y Doped  $\text{BiFeO}_3$ ”, *Asian Journal of Applied Sciences.*, 2321 , 0893,2009.
- [48] Park, T. J., Papaefthymiou, G. C., Viescas, A. J., Moodenbaugh, A. R., and Wong, S. S., “Size-Dependent Magnetic Properties of Single-Crystalline Multiferroic  $\text{BiFeO}_3$

Nanoparticles”, *Nano Lett.*, 7(3), 766, 2007.

- [49] Maleki, H., Zakeri, M., and Fathi, R., “Experimental study of the effect of yttrium on the structural, thermal, and magnetic properties of BiFeO<sub>3</sub>”, *Applied Physics A.*, 124, 728, 2018.
- [50] Bharathkumar, S., Sakar, M., Rohith Vinod, K., and Balakumar, S., “Versatility of electrospinning on the fabrication of fibrous mat and mesh nanostructures of bismuth ferrite (BiFeO<sub>3</sub>) and their magnetic, photocatalytic activities”, *Phys. Chem. Chem. Phys.*, 17, 17745, 2015.
- [51] He, J., Guo, R.Q., Fang, L.A., Dong, W., Zheng, F.G., and Shen, M.R., “Characterization and visible light photocatalytic mechanism of size-controlled BiFeO<sub>3</sub> nanoparticles”, *Mater. Res. Bull.* 48, 3017, 2011

# Chapter 5

## Summary and Conclusion

### 5.1 Summary

The nominal composition of  $\text{Bi}_{0.9}\text{Y}_{0.1}\text{FeO}_3$  bulk polycrystalline materials were synthesized by a conventional solid state reaction technique and their corresponding nanoparticles were produced directly from bulk powder materials by sol-gel and ultrasonication technique. The effect of Y-doping on structural, grain size distribution, electrical, optical, photocatalytic and magnetic properties were investigated.

The outcomes of this investigation are summarized as,

- After substitution of Y in place of Bi, structural phase transition was observed from the XRD pattern for Y doped  $\text{BiFeO}_3$  nanoparticles
- The grain size distributions were homogeneous and the average grain sizes decreased for Y doped in  $\text{BiFeO}_3$ .
- The absorption spectra confirmed that undoped and doped  $\text{BiFeO}_3$  can absorb light with wavelength from UV to visible region.
- In photocatalytic activity test, the higher photodegradation rate was found for 10% Y-doped  $\text{BiFeO}_3$  nanoparticles (prepared by sol-gel).
- The improved magnetization was observed with the substitution of Y in  $\text{BiFeO}_3$  bulk materials and Y doped nano particles (prepared by sol-gel) but the magnetization was decreased for Y-doped  $\text{BiFeO}_3$  nanoparticles (prepared by ultrasonication).
- The polarization (P) versus electric field (E) hysteresis loops were more typical for the 10% Y-doped  $\text{BiFeO}_3$  nanoparticles (prepared by sol-gel) compared to the 10% Y-doped  $\text{BiFeO}_3$  nanoparticles (prepared by ultrasonication).

## **5.2 Conclusion**

We may conclude that 10% Y-doped BiFeO<sub>3</sub> nanoparticles prepared by sol-gel technique is very good magnetic materials due to its high saturation magnetization and very good photocatalyst due to its high photosensitivity under visible light.

## **5.3 Suggestion for future work**

10% Y-doped BiFeO<sub>3</sub> nanoparticles prepared by Sol-gel technique will be used as a photocatalyst in producing H<sub>2</sub> gas via water splitting using solar energy from a solar simulator.